2009

Biophysical Characterization of Structure and Dynamics of Nuclear Pore Complex Components

Martin Kampmann

BIOPHYSICAL CHARACTERIZATION OF STRUCTURE AND DYNAMICS OF NUCLEAR PORE COMPLEX COMPONENTS

A Thesis Presented to the Faculty of

The Rockefeller University

in Partial Fulfillment of the Requirements for

the degree of Doctor of Philosophy

by

Martin Kampmann

June 2009

BIOPHYSICAL CHARACTERIZATION OF STRUCTURE AND DYNAMICS OF NUCLEAR PORE COMPLEX COMPONENTS

Martin Kampmann, Ph.D.

The Rockefeller University 2009

The Nuclear Pore Complex (NPC) mediates nucleo-cytoplasmic transport in all eukaryotes and is among the largest cellular assemblies of proteins, called nucleoporins (nups). The details of NPC architecture, dynamics, and mechanism are still unknown. NPCs can be dissected biochemically into distinct subcomplexes. One of the best-characterized subcomplexes, the Nup84 complex, consists of seven nups and was proposed to form a membrane-coating module of the NPC. I optimized the isolation of the heptameric complex from budding yeast and analyzed its structure by negative-stain electron microscopy (EM). My data confirm the previously reported flexible Y-shape. I solved the three-dimensional structures of two conformers of the heptamer and discerned additional details, including specific hinge regions. Tagged versions of two nups were localized within the heptamer and known crystal structures were docked into the EM map. The globular ends of the arms and the stem are formed by β-propeller

domains; thinner connecting segments are formed by α-solenoids. Strikingly, the same organizational principle is found in the clathrin triskelion, which was proposed to share a common evolutionary origin with the heptameric complex. A second focus of this thesis is the investigation of NPC dynamics in live cells, using polarized fluorescence microscopy. Two types of NPC dynamics have been suggested to play important functional roles: the dilation of the NPC to accommodate the transport of large cargoes, and the movement of disordered FG domains of nups to gate the NPC via entropic exclusion. An alternative model envisages a static FG domain meshwork that operates via hydrophobic exclusion. I analyzed theoretically how anisotropy measurements of GFP-tagged nups can be used to monitor nup orientation and dynamics. In a collaboration with the Simon lab (The Rockefeller University), we established techniques to analyze GFP anisotropy in live yeast cells. GFP attached to ordered nup domains displayed defined orientations with respect to the NPC, whereas GFP attached to the FG domains is randomly oriented. Homo-FRET between GFP-tags was observed in two cases. Future experiments should enable us to distinguish between different models for the role of FG domains in NPC gating, and to investigate NPC dilation during transport.

Meinen Eltern

in Liebe und Dankbarkeit

ACKNOWLEDGMENTS

I wish to express my gratitude to all those who have supported me throughout my time at The Rockefeller University, as mentors, teachers, collaborators, colleagues and companions. In particular, I thank

First and foremost, my advisor and mentor Dr. Günter Blobel. I am grateful for his guidance and our stimulating discussions that helped me to keep sight of the "big picture", as well as for the freedom he gave me to pursue my own ideas. I also thank him for teaching me much about writing a good paper. Parts of this thesis were adapted from a manuscript that we wrote together.

Dr. Sandy Simon, who has been a mentor to me in more than one way: as a teacher, as the chair of my thesis committee, and as a collaborator on one of the two projects presented in this thesis. His creativity and enthusiasm were always inspiring.

Dr. Alexa Mattheyses and Claire Atkinson, with whom I collaborated in the Simon lab. Working with them has taught me one of the most important lessons of graduate school: How enjoyable and productive a

collaboration can be, if you work with the right people. I also thank Alexa and Claire for critical comments on parts of this thesis.

Dr. Shai Shaham and Dr. Fred Cross, for the excellent courses they taught and for their guidance while serving on my faculty advisory committee.

Dr. Joachim Frank, the external member of my thesis committee. I am honored to have as an examiner the scientist who developed many of the methods I used for the single-particle EM project.

Dr. Ruben Diaz-Avalos and Dr. William Rice from the New York Structural Biology Center (NYSBC), who have taught me much about electron microscopy and computational image analysis, and whose advice was crucial for my EM project. I also thank all other NYSBC staff for their support.

Members of the Blobel lab for sharing advice and reagents, and for critical comments on parts of this thesis, especially Dr. Erik Debler, Dr. Elias Coutavas, Vivien Nagy, Johanna Napetschnig, Kuo Chiang-Hsia, Dr. Andre Hoelz, and Dr. Samuel Dales, who introduced me to thin-section EM.

Chad Lue and Zhonghui Huang, for technical assistance with plasmid and strain construction.

Dr. Thomas Huber and Dr. Sourabh Banerjee, with whom I started a collaboration that we will hopefully be able to pursue over the next few months.

Dr. Natacha Opalka for supporting early EM work I did at the Rockefeller University, and for sharing liposome protocols.

Dr. Frank Neumann for sharing a yeast microscopy protocol; Dr. Susan Wente, Dr. Caroline Ajo-Franklin, Dr. Kenneth Belanger, Dr. Megan King, Dr. Patrick Lusk and Dr. Xiaolan Zhao for sharing plasmids and yeast strains.

Many other colleagues and friends at The Rockefeller University, for their advice and sharing of materials over the years.

Dr. David King and the HHMI mass spectrometry facility for protein identification.

The David Rockefeller Graduate program and the Dean's Office for their unbureaucratic support.

The Howard Hughes Medical Institute for a predoctoral fellowship.

My family and friends, whose support and encouragement have been invaluable.

TABLE OF CONTENTS

LIST OF FIGURES

LIST OF TABLES

LIST OF ABBREVIATIONS

2D, two-dimensional

3D, three-dimensional

5-FOA, 5-fluoro-orotic acid

CCC, cross-correlation coefficient

CCD, charge-coupled device

CHAPS, 3-[(3-Cholamidopropyl)dimethylammonio]-1-propanesulfonate

Da, Dalton

DTT, dithiothreitol

EM, electron microscopy / electron microscopic

FG domain / motif / repeat, phenylalanine-glycine domain / motif / repeat

FRET, fluorescence resonance energy transfer

FSC, Fourier shell correlation

GAP, GTPase-activating protein

GEF, guanine nucleotide exchange factor

GFP, green fluorescent protein; the enhanced version (EGFP) was used.

HEPES, 4-(2-hydroxyethyl)-1-piperazineethanesulfonic acid

IgG, immunoglobulin G

Kap, karyopherin

NLS, nuclear localization sequence

NPC, Nuclear Pore Complex

Nup, nucleoporin

OD600, optical density at 600 nm

PAGE, polyacrylamide gel electrophoresis

PCR, polymerase chain reaction

PDB, protein data bank

PMSF, phenylmethylsulphonyl fluoride

SDS, sodium dodecyl sulfate

TAP-tag, tandem affinity purification tag

TEV protease, tobacco etch virus protease

CHAPTER 1: Introduction

This chapter introduces the subject of the thesis, the structure and function of the nuclear pore complex, as well as the experimental approaches used to obtain the results that are presented in the following chapters.

The Nuclear Pore Complex

The hallmark of eukaryotic cells is their compartmentalization into specialized membrane-bounded organelles. The most prominent organelle is the nucleus, which contains the genomic DNA. The boundary between the nucleus and the cytoplasm is formed by the nuclear envelope, which consists of two membranes: the inner nuclear membrane on the nucleoplasmic side, and the outer nuclear membrane, which is continuous with the endoplasmic reticulum, on the cytoplasmic site. The nuclear envelope is perforated by circular pores, at which the inner and outer nuclear membranes are connected by a sharply bent membrane domain called the pore membrane. These pores contain a large proteinaceous assembly, the nuclear pore complex (NPC) (**Figure 1**).

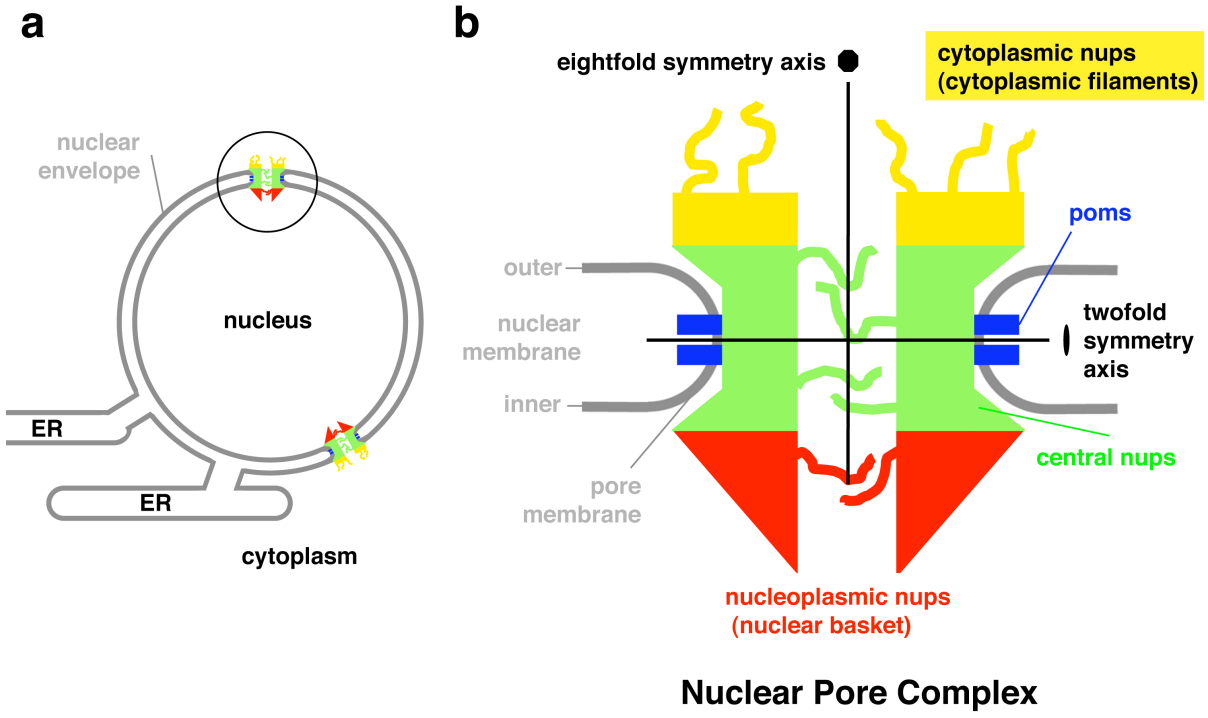

Figure 1 Schematic overview of Nuclear Pore Complex architecture and membrane topology. (**a**) The nuclear envelope is a double membrane surrounding the nucleus. It is perforated by pores containing nuclear pore complexes (NPCs). The outer nuclear membrane is continuous with the ER. (**b**) Detailed view of a NPC. A pore in the nuclear membrane is a circumscribed fusion between the inner and outer nuclear membranes. The membrane domain lining the pore is the pore membrane; it contains integral membrane proteins called poms, which anchor the NPC. The proteins constituting the NPC are called nucleoporins (nups). The NPC has an eightfold axis of symmetry perpendicular to the nuclear membrane. The central core of the NPC also has a twofold symmetry axis in the nuclear envelope mid-plane. Nucleoplasmic and cytoplasmic nups are bound asymmetrically to the central core.

The NPC mediates transport between the nucleus and the cytoplasm. Nucleo-cytoplasmic transport is required for many basic cellular functions: mRNAs, which are transcribed and processed in the nucleus, are exported to the cytoplasm, where they are translated; the 40S and 60S ribosomal subunits are assembled in the nucleus and exported into the cytoplasm; proteins functioning in the nucleus need to be imported from the cytoplasm, where they are synthesized.

While actively transporting a variety of substrates, some of them very large, the NPC also functions as a passive diffusion barrier for molecules larger than ~40 kDa that are not selectively transported. Thus, the NPC functions as the "gatekeeper" of the nucleus. The control of access to the genomic DNA can be a regulatory mechanism, for example in the case of transcription factors.

Besides its transport function, the NPC has been implied in chromatin organization, gene regulation, and maintenance of genome integrity. The mechanistic basis for these diverse functions of the NPC is currently not understood in detail.

Modular architecture of the NPC

The NPC is an assembly of multiple copies of ~30 different proteins called nucleoporins (nups), with an estimated total mass of ~50 MDa in budding yeast and an even greater mass in metazoan cells (Cronshaw et al., 2002; Rout et al., 2000). The pore membrane domain contains three specific integral membrane proteins called poms, which presumably function in anchoring the soluble nups. The relative stoichiometry of nups within the yeast NPC has been estimated from quantitative Western blots (Rout et al., 2000).

Electron microscopic (EM) structures of whole NPCs from a variety of organisms have revealed the dimensions and symmetry of the NPC, as well as its overall architecture (Akey and Radermacher, 1993; Beck et al., 2004; Beck et al., 2007; Hinshaw et al., 1992; Kiseleva et al., 2004; Yang et al., 1998). The NPC displays eightfold symmetry around its nucleo-cytoplasmic axis. A small fraction of NPCs with nine- or tenfold symmetry has been observed as well (Hinshaw and Milligan, 2003). In addition, the central core of the NPC displays two-fold symmetry around an axis within the nuclear envelope mid-plane. Peripheral nups are asymmetrically bound to the cytoplasmic and nucleoplasmic sides of the core, where they form

cytoplasmic filaments and the so-called nuclear basket structure, respectively (**Figure 1**).

In budding yeast, the core NPC is up to 100 nm wide, and its extension along the nucleo-cytoplasmic axis is ~30 nm (Yang et al., 1998). It contains a central channel with a diameter of about 40 nm, through which selective transport between nucleus and cytoplasm occurs. The approximate locations of nups within the yeast NPC have been mapped by immuno-EM (Rout et al., 2000).

Several high-resolution crystal structures have been solved of individual nup domains (Berke et al., 2004; Hodel et al., 2002; Hsia et al., 2007; Jeudy and Schwartz, 2007; Napetschnig et al., 2007; Robinson et al., 2005; Weirich et al., 2004), as well as binary complexes between nup domains (Berke et al., 2004; Boehmer et al., 2008; Brohawn et al., 2008; Debler et al., 2008; Hsia et al., 2007; Melcák et al., 2007).

Based on these crystal structures, different models for the arrangement of nups within the NPC have been proposed (Brohawn et al., 2008; Hsia et al., 2007). Based mostly on biochemical interaction data, a computer-generated model for NPC architecture was proposed (Alber et al., 2007). However, a consensus model has not yet emerged.

Both EM (Akey, 1995; Beck et al., 2004; Beck et al., 2007) and crystallographic data (Boehmer et al., 2008; Debler et al., 2008; Melcák et al., 2007), as well as atomic force microscopy studies (Jaggi et al., 2003; Mooren et al., 2004; Stoffler et al., 1999; Wang and Clapham, 1999) suggest that the NPC is conformationally flexible. This flexibility may be a functional requirement - specifically, dilation of the NPC has been suggested to facilitate the transport of large cargo (Melcák et al., 2007).

Several nups contain so-called FG domains featuring repeats of characteristic phenylalanine-glycine (FG) motifs. These domains do not adopt defined folds and are unstructured *in vitro* (Lim et al., 2006). The FG domains are thought to fill the central channel of the NPC and form filaments extending into the nucleus and cytoplasm. They have been proposed to provide the basis for selective transport through the NPC, as described below. FG domains cannot easily be studied by classical methods of structural biology, due to their disordered nature. Most of our knowledge of NPC structure is limited to the ordered domains of nups.

The Nup84 complex: a conserved NPC subcomplex

Nups are organized into distinct structural modules, called NPC subcomplexes. In higher eukaryotes, the NPC undergoes disassembly into

these subcomplexes during mitosis. Interphase NPCs can be dissected biochemically into similar subcomplexes.

One of the best-characterized NPC subcomplexes is the heptameric Nup84 complex from yeast. This heptameric complex consists of Nup133, Nup84, Nup145C, Sec13, Nup85, Seh1 and Nup120 and has a predicted molecular mass of 576 kDa. The heptamer can be isolated from budding yeast, using non-ionic detergent and salt (Siniossoglou et al., 2000), and it was also successfully reconstituted from proteins that were recombinantly expressed in *E. coli* (Lutzmann et al., 2002).

Both reconstituted and native complex were shown by negative–stain electron microscopy to form a Y-shaped structure (Lutzmann et al., 2002; Siniossoglou et al., 2000). Based on reconstitution and negative-stain electron microscopy of various nup modules of the heptamer, the positions of these modules within the two-dimensional Y-shaped structure were suggested (Lutzmann et al., 2002). While several crystal structures of heptameric complex nups are known (Brohawn et al., 2008; Debler et al., 2008; Hsia et al., 2007), the three-dimensional structure of the entire heptamer has not been previously determined.

The yeast Nup84 complex has an equivalent in vertebrate cells, the nonameric Nup107-160 complex (Belgareh et al., 2001; Glavy et al.,

2007; Loïodice et al., 2004). The nonameric complex stays intact throughout mitosis, when it is targeted to kinetochores and functions in spindle assembly (Belgareh et al., 2001; Orjalo et al., 2006; Zuccolo et al., 2007). It was also shown to be required for NPC formation (D'Angelo et al., 2006; Harel et al., 2003; Walther et al., 2003). These findings suggest that the subcomplex represents a functional module.

Interestingly, both the heptameric and the nonameric complexes share a protein subunit, Sec13, with the COPII complex, which coats vesicles for transport from the ER to the Golgi apparatus. Furthermore, the two principal folds of the heptamer nups, β-propellers and α-solenoids, are also found in coat complexes for vesicular transport. These facts have led to the hypothesis that the heptameric complex, as well as vesicle coats, have evolved from a "protocoatamer", which played a crucial role in the evolution of eukaryotic cells (Devos et al., 2004). The formation of the nuclear envelope and the endoplasmic reticulum in the evolution of prokaryotic to eukaryotic cells was envisaged to occur by invagination of specific domains of the prokaryotic plasma membrane (Blobel, 1980). A protocoatamer was suggested to stabilize the sharp membrane bends generated by this process. During the evolution of eukaryotic cells, this protocoatamer would have

given rise to present-day membrane coat structures, including the heptameric subcomplex of the NPC (Devos et al., 2004).

Consistent with a membrane-coating function, the heptamer is localized close to the pore membrane *in vivo* (Rout et al., 2000). Moreover, several of the heptameric complex nups contain a predicted membrane-curvature sensing motif, and in the case of Nup133, this motif was shown to mediate selective binding to highly curved liposomes *in vitro* (Drin et al., 2007).

FG Domains and Mechanism of Transport through the NPC

Proteins destined for nuclear import or export contain short sequences that function as nuclear localization sequence (NLS) or nuclear export sequence (NES). These sequences are recognized by transport factors called karyopherins (kaps), which in turn interact with FG motifs to facilitate transport through the NPC.

The directionality of transport is controlled by Ran, a small GTPase. A guanine nucleotide exchange factor for Ran (ran-GEF) is localized to the nucleus, whereas a GTPase activating protein for Ran (ran-GAP) is present in the cytoplasm. This distribution results in a high ratio of Ran-GTP to Ran-GDP in the nucleus, and a high Ran-GDP to Ran-GTP

ratio in the cytoplasm. Ran-GTP dissociates imported proteins from their kaps in the nucleus, thus sequestering the imported protein in the nucleus. Ran-GTP also stabilizes complexes of export cargoes with their kaps, thus facilitating export. In the cytoplasm, Ran-GEF stimulates GTP hydrolysis by Ran, which leads to the dissociation of the export complex.

While the role of these soluble transport factors has been well characterized, the mechanism by which the interaction between kaps and FG repeats leads to transport through the NPC is still controversial, and several models have been proposed (**Figure 2**).

According to the *virtual gating* model (Rout et al., 2003; Rout et al., 2000), the free ends of FG domains are highly mobile and form a dynamic "polymer brush" occluding the central channel of the NPC. This behavior has been observed for isolated FG domains *in vitro* (Lim et al., 2006). Thereby, they prevent large molecules from entering the NPC. Kaps mediate binding to the FG repeats, and the binding energy is proposed to overcome the entropically unfavorable pathway through the occluded channel of the NPC.

The *selective phase* model (Frey and Gorlich, 2007; Ribbeck and Gorlich, 2002) suggests that the FG repeats interact with each other and form a hydrophobic meshwork in the central channel of the NPC that

prevents the passage of hydrophilic cargo. A hydrogel could be formed from isolated FG domains *in vitro* using a pH-shift protocol (Frey and Gorlich, 2007). Kap binding to FG repeats competes with FG–FG interactions, thus allowing kap-bound cargo to partition into the hydrophobic phase and "melt through" the meshwork.

The *dual-gate* model (Patel et al., 2007) is a combination of the previous two models: mobile nups at the NPC periphery may present an entropic barrier, while a central meshwork of nups may form a hydrophobic barrier.

In an addition to the virtual gating model, kaps were suggested to bind several FG repeats cooperatively, thus inducing a local collapse of mobile FG domains around the cargo complex, which would counteract the steric repulsion and promote capture and transport (Lim et al., 2007).

These models were mostly supported by studies of isolated FG domains *in vitro*. The dynamics of FG repeats have not previously been studied in the context of live cells.

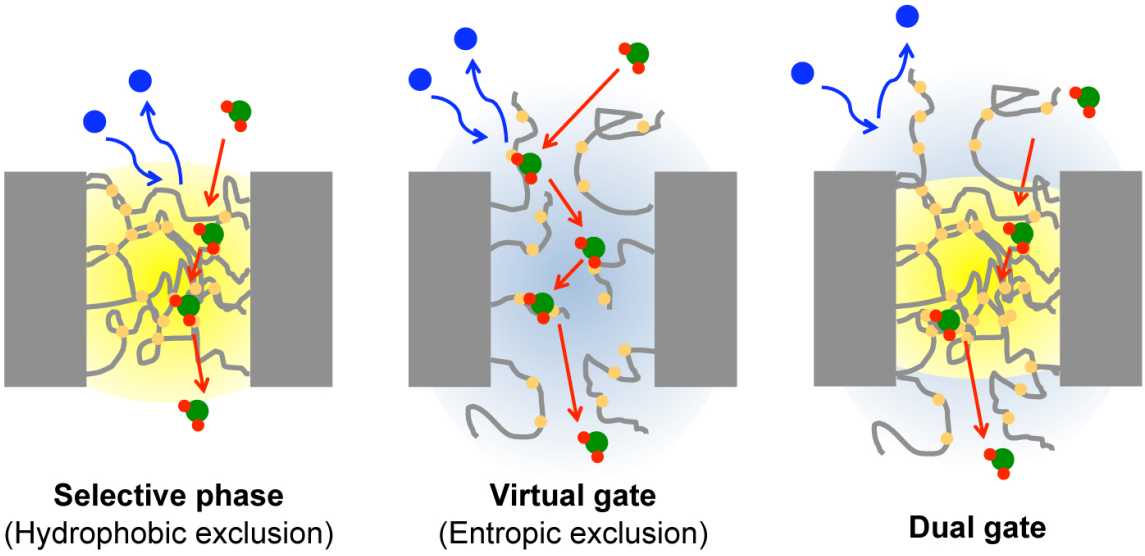

Figure 2 Models for selective transport through the NPC. FG domains are schematically depicted as grey lines, with yellow dots representing FG motifs. Blue disc: protein excluded from the NPC channel. Green disk: kap-cargo complex. Red dots represent FG-binding sites on the kap. In the selective phase model, FG domains form a hydrophobic meshwork cross-linked by interactions between FG motifs. Kaps interact with FG motifs and thus partition into the "FG phase". In the virtual gating model, FG domains are highly mobile and prevent proteins from entering the NPC channel entropically. Kaps bind FG motifs and the binding energy overcomes the entropic cost of traversing the channel. The dual gate model combines the two models.

Electron Microscopy of Macromolecular Complexes

A major part of the results presented in this thesis is based on electron microscopic (EM) studies of a NPC subcomplex. This section introduces concepts underlying EM of macromolecular assemblies that are directly relevant to the work presented in Chapter 2. For a detailed description of the methodology, the reader is referred to the monograph by Frank (Frank, 2006).

Image formation in the EM relies on the scattering of electrons by a thin specimen. To prevent electron scattering by air molecules, a vacuum is maintained inside the EM. Biological specimens scatter a small fraction of the electrons elastically, and interference of unscattered and elastically scattered electrons generates so-called *phase contrast* in the image plane. Inelastic scattering events and scattering of electrons outside the aperture of the EM result in a reduction of the number of electrons reaching the image plane and thereby generates so-called *amplitude contrast*. The transformation of the projected Coulomb potential of the specimen into image contrast by the EM is described quantitatively by the *contrast transfer function*. The image can be recorded on photographic film or by a CCD camera linked to a scintillator screen that generates light signals in response to impacting electrons.

Unstained biological specimens generally give rise to low-contrast EM images. To improve the contrast, staining protocols have been developed. A commonly used approach is *negative staining* of macromolecules or viruses with heavy metal salt solutions (Brenner and Horne, 1959), as illustrated in **Figure 3**. Particles in aqueous solution are adsorbed to a thin carbon support film and a solution of a heavy metal salt is added. The sample is dried, leaving a layer of heavy metal stain on the support film. Stain is excluded from the biological particles, thus negatively staining the specimen. Potential artifacts of the negative staining technique include (i) distortion of the particle structure during the air-drying process, (ii) loss of information about internal particle structures that are not penetrated by the stain, and (iii), in the case of large particles, incomplete coverage of the particle with stain, leading to "one-sided" staining.

To avoid staining artefacts, samples can be subjected to cryo-EM: An aqueous solution containing biological molecules is applied to a perforated carbon film and frozen rapidly to obtain a thin layer of vitreous ice, which can then be imaged under vacuum. The advantage of this method is that particles are in a more "native-like" state. However, cryo-EM images are typically very low in contrast.

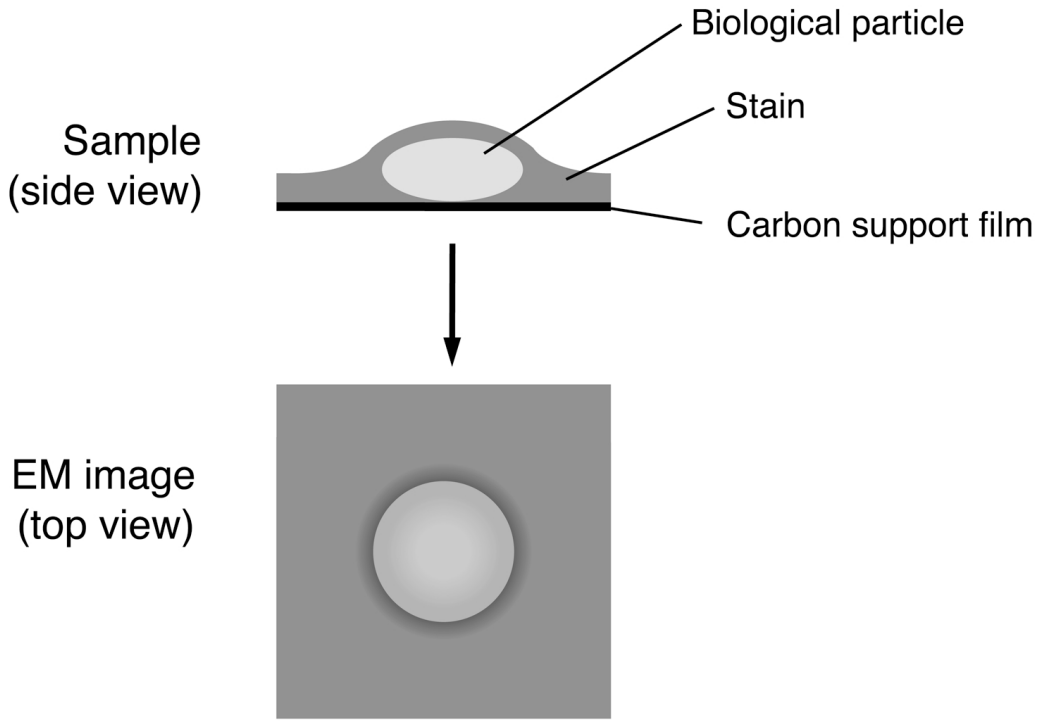

Figure 3 Negative staining of biological particles (schematic diagram). Particles of interest and a heavy metal stain are applied to a carbon support film and dried. Stain is excluded from the particles, which therefore appear as bright objects on a dark background. Accumulation of stain around the particle occurs frequently and gives rise to a dark rim surrounding the particle.

When exposed to the electron beam inside the EM, biological samples suffer radiation damage. To minimize this damage, the total dose of electrons used for particle imaging is typically limited to ~10 electrons per

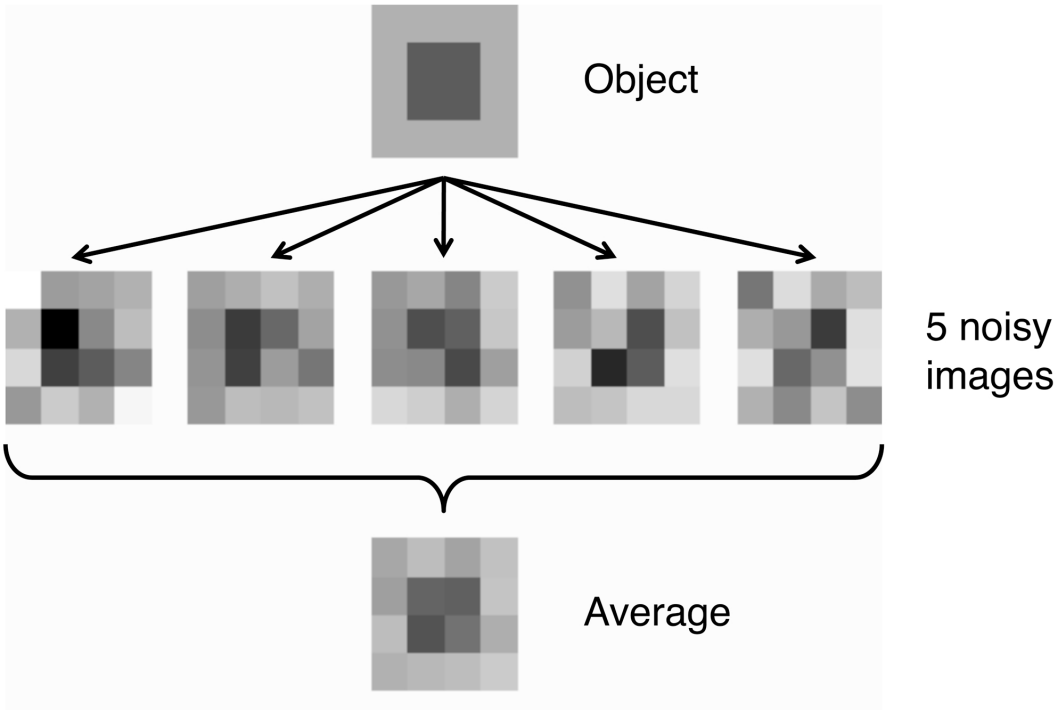

Figure 4 Averaging of noisy images increases the signal-to-noise ratio (schematic diagram). The object of interest is a dark square on a lighter background. Five noisy images are taken and digitized to yield 4-by-4 pixel images. Each pixel is associated with a numeric value corresponding to its brightness on a grayscale. Pixel values at corresponding positions of the images can be averaged. The average image resembles the object more closely than any of the individual noisy images.

Å^2. The disadvantage of this *low-dose* regime is that the resulting images contain a high level of stochastic shot noise. The signal-to-noise ratio can be increased by averaging a large number of images (Frank et al., 1981), as illustrated in **Figure 4**.

Only images representing a highly similar view and conformation of the particle should be averaged, particle images therefore need to be classified into groups representing distinct particle views or conformations. Alignment of particle images is required prior to classification and averaging. Computational methods for automatic reference-free alignment (Penczek et al., 1992) and classification (van Heel and Frank, 1981) of particle images are available.

A quantitative measure for the quality of alignment between two images is the cross-correlation coefficient (CCC). For digitized images *a* and *b* with average pixel intensity values <*a*> and <*b*>, which are each composed of *N* pixels with the intensities a_i and b_i in the *i*-th position within the image, the CCC is defined as

$$[1.1] \qquad CCC = \frac{\sum_{i=1}^{N}(a_i - \langle a \rangle) \cdot (b_i - \langle b \rangle)}{\sqrt{\sum_{i=1}^{N}(a_i - \langle a \rangle)^2 \cdot \sum_{i=1}^{N}(b_i - \langle b \rangle)^2}}$$

As illustrated in **Figure 5**, the correct alignment between two images can be found by calculating the CCC between two images in all possible positions relative to each other and choosing the position with the highest CCC.

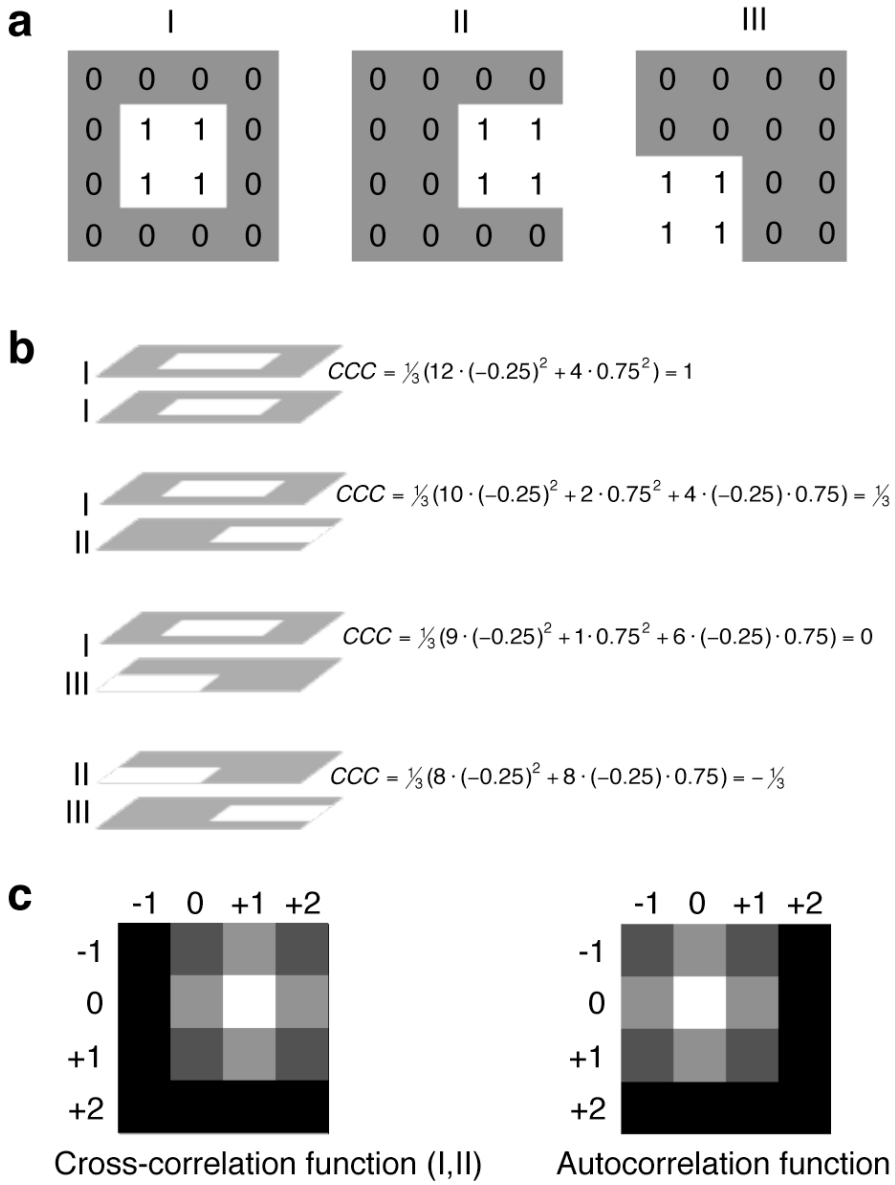

Figure 5 Image alignment based on the cross-correlation coefficient (CCC). (**a**) Examples of unaligned images of a white square on a dark background There are only two pixel values, 0 and 1. (**b**) The CCC is calculated for different combinations of images. (**c**) A translational cross-correlation function is obtained by shifting two images across each other and calculating a CCC for every possible shift. The maximum of the cross-correlation function indicates the shift needed for optimal alignment. An autocorrelation function is the cross-correlation function of an image with itself.

In order to classify aligned images, a metric of image similarity is required. Digital grayscale images with $n \cdot m$ pixels can be described as points in an $n \cdot m$-dimensional space, and their Euclidean distance can provide a measure of similarity, provided that pixel values were normalized in each image (**Figure 6**). To analyze clustering of images in this high-dimensional space, methods of multivariate data analysis, such as *principal component analysis* are used to reduce the dimensionality of the problem. Other metrics for the similarity between images are also in use, such as the χ^2 distance in *correspondence analysis* (van Heel and Frank, 1981). Either method determines those directions (factors) in $n \cdot m$ space along which most of the variance occurs. These factors are called *eigenimages*, since they correspond to eigenvectors in principal component analysis. Most of the signal is usually contained in the first few factors; thus every original image can be reconstituted as a linear combination of a limited number of eigenimages. Hierarchical ascendant classification or k-means clustering can then be used to classify images in this lower-dimensional space.

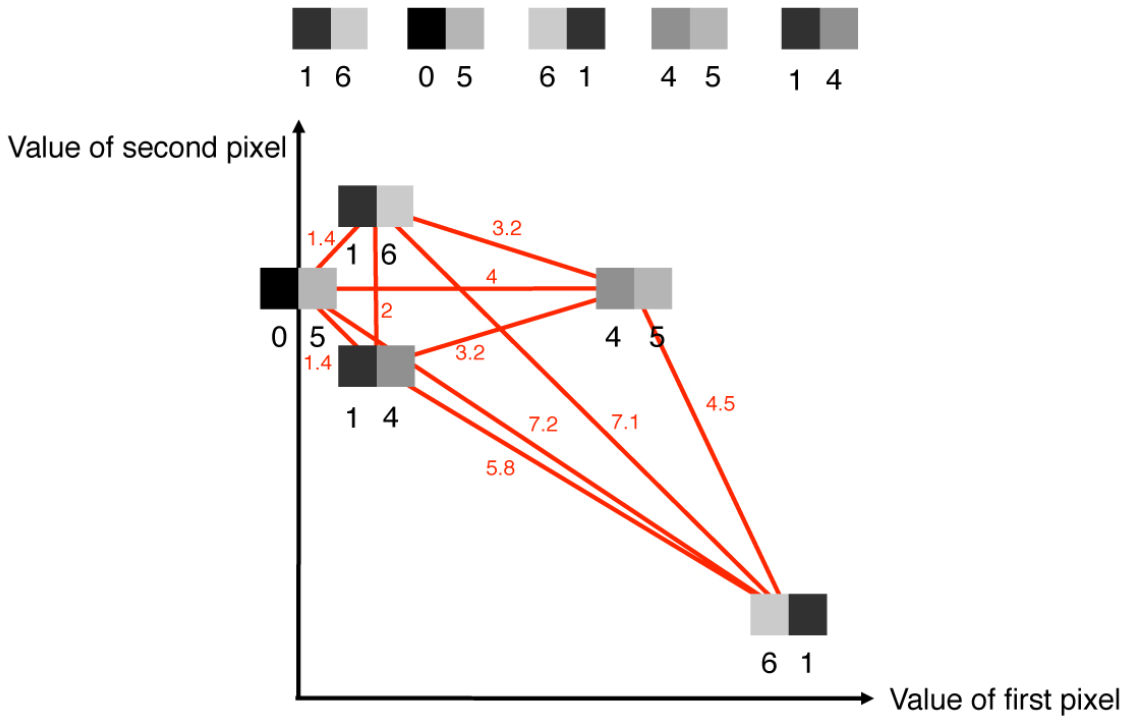

Figure 6 Clustering of images based on Euclidean distances. Two-pixel grayscale images can be assigned to points in a two-dimensional space, where their coordinates are defined by the pixel values at two positions. Euclidean distances can then be calculated (shown in red) and serve as a basis for the detection of clusters.

The central problem in single-particle EM is how the three-dimensional (3D) structure of a particle can be reconstructed from a number of two-dimensional (2D) images. A straightforward solution would be to rotate the specimen within the EM and take pictures from many different angles. However, due to the low-dose requirement for single-particle EM,

only one or two images with an acceptable signal-to-noise ratio can be taken from a given area of the specimen.

A commonly used technique for the *de novo* determination of 3D structures is random-conical tilt reconstruction (Radermacher et al., 1986). As illustrated in **Figure 7**, a field of particles, usually adsorbed to a carbon support film, is tilted by a known angle, and a first image is taken. Then, the sample is returned to an untilted position and a second image is taken. Since the in-plane orientation of particles in untilted images is random, the tilted images show a range of different particle views. Pairs of tilted and untilted images of the same particle are selected. Untilted particle images are used to classify particles and determine their in-plane orientation, and tilted particle images are used to reconstruct the 3D structure of the particle.

When a previously determined 3D structure of a given particle is available, *projection matching* can be applied to obtain a reconstruction using more or better 2D images. The previous 3D structure is used to calculate 2D projection images in different directions. The new images of particles in unknown orientations can then be aligned to whichever

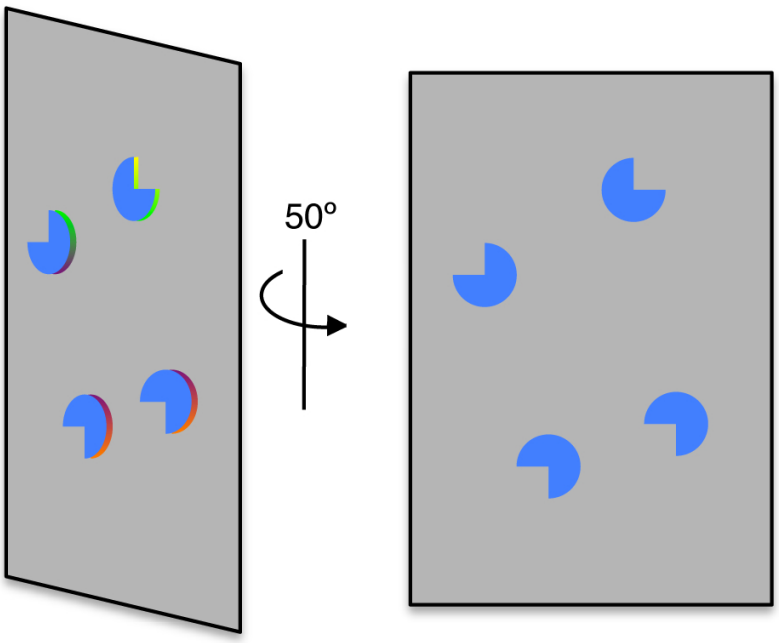

Figure 7 Principle of Random Conical Tilt reconstruction. A field of particles is imaged once at a 50º tilt angle, and then without tilt. The untilted image is used to determine in-plane orientations of particles. The tilted images show different views of the particle and are used for 3D reconstruction.

projection they most resemble, based on cross-correlation. Thus, the orientation of the new image is determined and a new 3D structure can be reconstructed from the new images.

There are several operational definitions for the resolution of a 3D EM structure. Most commonly, the set of images is randomly split in half and independent 3D structures are reconstructed from each of the half-

sets. These structures are Fourier-transformed, resulting in volumes in reciprocal space, where the center of the volume corresponds to the lowest spatial frequency, and concentric "Fourier shells" around it correspond to increasing spatial frequencies. The cross-correlation between corresponding shells from the two volumes is calculated. The cross-correlation typically decreases as the spatial frequency increases, and the spatial frequency at which the Fourier shell correlation drops to 0.5 is regarded as the reproducible resolution of the initial 3D structure.

Fluorescence anisotropy

Chapter 3 presents the development of assays for NPC architecture and dynamics based on polarization fluorescence microscopy. This section introduces the most important principles underlying that technique. More details can be found in textbooks of biophysical chemistry (Cantor and Schimmel, 1980).

Molecules can exist in different energy states, corresponding to different electronic, vibrational, and rotational states. At room temperature, molecules are in the lowest electronic state, S_0. However, absorption of a photon with the required energy will excite a molecule to the next electronic state, S_1 (**Figure 8**). By vibrational relaxation, the molecule reaches the lowest

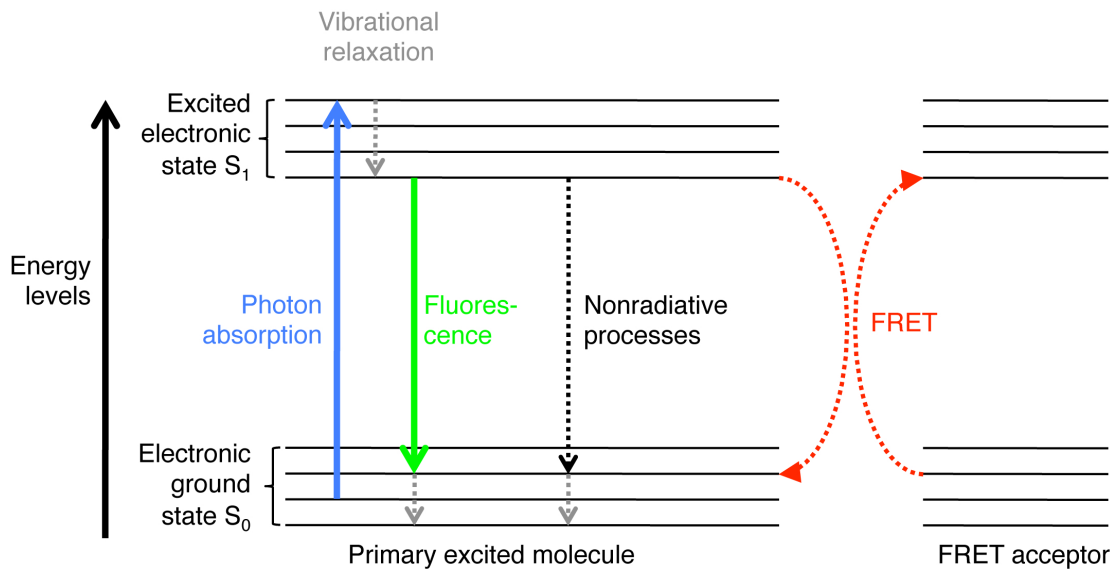

Figure 8 Fluorescence and competing processes. Horizontal lines represent different vibrational energy levels of molecules. Absorption of a photon can excite a molecule such that it transitions from the ground electronic state, S_0, to an excited electronic state S_1. Part of the energy is rapidly dissipated by vibrational relaxation. The ground state can be reached by emission of a photon (fluorescence), by nonradiative processes, or by transfer of energy by FRET to a nearby molecule, which will in turn transition to the excited electronic state.

vibrational energy level within S_1. From here, the molecule can return to the electronic ground state S_0 either by non-radiative processes (such as quenching or internal conversion), or by emitting a photon in a process called *fluorescence*. Since a fraction of the energy of the absorbed photon is usually dissipated by vibrational relaxation, the energy of the photon emitted

by fluorescence is typically lower than the energy of the absorbed photon and the emitted light has a longer wavelength than absorbed light.

Non-radiative decay and fluorescence are competing pathways occurring with rates k_{nr} and k_F, respectively. Not every absorbed photon will lead to emission of a photon. The ratio of emitted photons to absorbed photons is called *quantum yield* ϕ_F, and can be calculated as:

[1.2] $$\phi_F = k_F / (k_F + k_{nr})$$

Molecules undergoing fluorescence are called *fluorophores*. Excited states of fluorophores decay exponentially over time, thus the fluorescence intensity of a population of fluorophores excited at time t = 0 follows:

[1.3] $$I(t) = I_0 \cdot e^{-t/\tau_F}$$

I_0 is the initial fluorescence intensity, and the decay constant τ_F is called *fluorescence lifetime*, and can be calculated as follows:

[1.4] $$\tau_F = \phi_F / k_F = 1 / (k_F + k_{nr})$$

Fluorescence lifetimes are typically on the nanosecond timescale.

Transitions between electronic states of a molecule are associated with *transition dipole moments* that correspond to a spatial vector $\boldsymbol{\mu}$ in the coordinate system of the molecule. Light can be described as a rapidly oscillating electromagnetic field, and excitation of a molecule by light occurs most efficiently when the electric field vector of the light is parallel to the absorption transition dipole moment of the molecule. When plane-polarized light is used to excite a population of molecules, those molecules oriented with $\boldsymbol{\mu}$ parallel to the direction of the electric field vector $\boldsymbol{E}$ have the highest probability of being excited. This phenomenon is called *photoselection*.

The polarization of light emitted from a fluorophore will be parallel to the emission transition dipole of the molecule. The transition dipoles for photon absorption and emission are parallel if both transitions are between the same electronic states of a molecule. Assuming that the molecules do not rotate between absorption and emission, and that the population of molecules is randomly oriented (isotropic), one can calculate which fraction of the emitted light maintains the polarization direction of the

exciting light. A measure for this conservation of the initial polarization is called *anisotropy* and measured as follows:

[1.5] Measured anisotropy $A = \frac{I_{\parallel} - I_{\perp}}{I_{\parallel} + 2I_{\perp}}$

$I_{\parallel}$ and $I_{\perp}$ are the intensities of emitted light measured after passing through a polarizer oriented parallel or perpendicular, respectively, to the polarization direction of the exciting light. For a rigid, isotropic sample as described above, the value for A is:

[1.6] Limiting anisotropy $A_0 = \frac{3\cos^2 \xi - 1}{5}$

where ξ is the angle between transition dipoles. This angle can directly be determined in rigid isotropic samples, where the measured anisotropy A is identical to the limiting anisotropy A_0. If the absorption and emission dipoles are the same, A_0 becomes 0.4.

Samples that are not rigid or isotropic will have other anisotropy values, hence anisotropy measurements can reveal properties of a sample, as described in the following three subsections.

(i) Rotational diffusion of the fluorophores

If molecules rotate between photon absorption and emission, the transition dipoles of absorption and emission will differ in the coordinate system of the observer. If the rotation is slow compared to the fluorescence lifetime of the molecule, the dipoles will be correlated, but if the rotation is very fast compared to the fluorescence lifetime, the dipoles become virtually uncorrelated, and thus almost all information about the polarization plane of the exciting light is lost. The ratio between the rotational correlation time τ_c of the fluorophore and its fluorescence lifetime τ_F thus determines the measured anisotropy as described by the *Perrin equation*:

$$[1.7] \qquad A = A_0 \cdot \frac{1}{1 + \tau_F / \tau_c}$$

Hence, the limit for A is 0 as τ_c tends to 0: for very short correlation times, the light becomes depolarized. For τ_c much larger than τ_F, the fluorophore behaves essentially as rigid and A becomes A_0.

The rotational correlation time τ_c is inversely proportional to the rotational diffusion constant D_{rot} of the fluorophore, and thus depends on

the hydrated volume V_H of the fluorophore, as well as on temperature T and viscosity η:

[1.8] $$\tau_c = \frac{1}{6 \cdot D_{rot}} = \frac{V_H \cdot \eta}{k \cdot T}$$

where k is Boltzmann's constant. For globular proteins, the hydrated specific volume is ~1 cm^3/g. From this value, we can predict τ_c for a globular protein of molecular mass M in water at 20ºC to be:

[1.9] $$\tau_c = M/2.4 \times 10^{-9} \text{ seconds / kDa.}$$

Therefore, fluorescence anisotropy measurements can be used to monitor rotational diffusion, and to calculate the volume and approximate mass of a fluorophore in a solution of known viscosity.

(ii) Orientation of the fluorophores

While molecules in solution are usually randomly oriented, molecules in biological systems can be ordered according to various geometric principles. In the simplest case, all fluorophore transition dipoles **μ** could be parallel to each other, and excitation and emission dipoles could be identical. When

exposed to polarized light, the excitation of fluorophores in the sample will then depend on the angle between $\boldsymbol{\mu}$ and the electric field vector $\boldsymbol{E}$ of the light. If they are perpendicular, no fluorophores are excited. If they are parallel, all fluorophores are maximally excited. In general, the probability p of excitation will depend on the angle between $\boldsymbol{\mu}$ and $\boldsymbol{E}$ as follows:

[1.10] $$p \propto \cos^2 \angle(\boldsymbol{E},\boldsymbol{\mu}) = \left(\frac{\boldsymbol{E} \cdot \boldsymbol{\mu}}{|\boldsymbol{E}||\boldsymbol{\mu}|} \right)^2$$

The components of the emitted light parallel and perpendicular to E will also depend on the dipole orientation $\boldsymbol{\mu}$:

[1.11] $$I_{\parallel} \propto p \cdot \cos^2 \angle(\boldsymbol{E},\boldsymbol{\mu})$$

[1.12] $$I_{\perp} \propto p \cdot \sin^2 \angle(\boldsymbol{E},\boldsymbol{\mu})$$

The resulting anisotropy value is a function of $\boldsymbol{\mu}$. Note that the anisotropy in this example can reach values of up to 1, whereas for samples with randomly oriented fluorophores, the maximum value is 0.4

(iii) Fluorophore clustering

An excited molecule can pass on its energy to a nearby fluorophore, thereby exciting it. Note that this process is not mediated by photon emission and absorption. It is referred to as *fluorescence resonance energy transfer* (FRET) and can occur as long as the emission spectrum of the donor molecule overlaps with the absorption spectrum of the acceptor molecule. FRET efficiency E is highly dependent on the distance $|\boldsymbol{R}|$ between fluorophores:

$$E = \frac{R_0^6}{R_0^6 + |\boldsymbol{R}|^6} \quad [1.13]$$

where R_0, the distance of half-maximal FRET efficiency, is called the Förster distance. R_0 depends on a number of factors, including the spectral overlap between donor emission and acceptor absorption, the quantum yield of the donor, the refractive index of the medium, and, as detailed below, on the orientation between donor and acceptor dipoles:

$$R_0 \propto \sqrt[6]{\kappa^2} \quad [1.14]$$

where κ^2 is the orientation factor defined as:

[1.15] $$\kappa^2 = (\cos\theta - 3 \cdot \cos\varphi \cdot \cos\psi)^2$$

for angles θ (between the donor emission and acceptor absorption dipoles), φ (between donor emission dipole and the vector ***R*** connecting donor and acceptor) and ψ (between acceptor absorption dipole and ***R***), as shown in **Figure 9**. For a mixture of randomly oriented molecules, the average κ^2 is 2/3.

When FRET occurs between two identical fluorophores, it is referred to as *homo-FRET*. While homo-FRET cannot be detected on the basis of the wavelength of emitted light, it will typically cause a decrease in fluorescence anisotropy. This is due to the fact that while the anisotropy of light emitted from donor molecules that were photoselectively excited with polarized light reflects the orientation of the donor, homo-FRET can lead to emission from fluorophores that would normally not have been excited by the polarized light. Hence the perpendicular component of the emitted light intensity will generally increase and the anisotropy will decrease. In ordered systems, the geometry of dipole orientations will determine the extent and effects of homo-FRET.

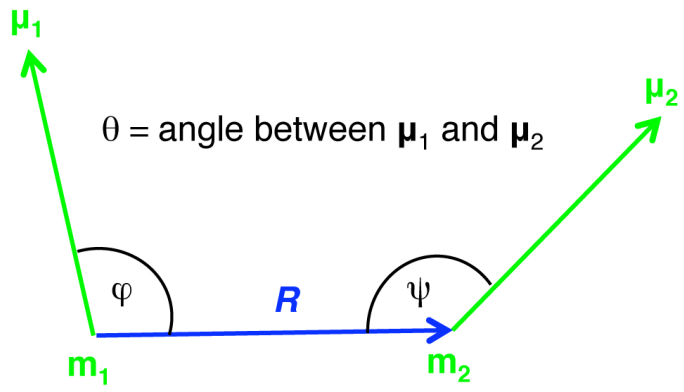

Figure 9 Angles defining the orientation factor κ^2 for FRET. See text for details.

CHAPTER 2: Three-dimensional structure and electron microscopic analysis of the membrane-coating module of the nuclear pore complex

I set out to determine the three-dimensional structure of native Nup84 complex from budding yeast by single-particle EM. My objective was the elucidation of the architectural principles of the heptameric complex, which would provide further insights into the proposed evolutionary relationship between the NPC subcomplex and vesicle coats, and a detailed characterization of the observed flexibility of the heptamer. Moreover, docking of nup crystal structures into an EM structure of the entire subcomplex should be an important step towards bridging the gap between high-resolution structures of individual nups and low-resolution structures of the entire NPC.

Purification and EM of the Nup84 complex from budding yeast

Purification protocols for affinity-tagged Nup84 complex from budding yeast have been reported (Cristea et al., 2005; Lutzmann et al., 2005; Siniossoglou et al., 2000; Siniossoglou et al., 1996). The published protocols produced particle populations either missing individual proteins, namely

Nup133 (Siniossoglou et al., 2000; Siniossoglou et al., 1996), or containing additional nups or other proteins (Cristea et al., 2005; Lutzmann et al., 2005). Furthermore, most of the published protocols (Cristea et al., 2005; Siniossoglou et al., 2000; Siniossoglou et al., 1996) used lysis buffer containing 1% Triton X-100, well above the critical micelle concentration. Potential incorporation of the protein complex into micelles would likely compromise structure determination by EM. Also, I hoped to recover higher-order structures of the Nup84 complex that may exist within the NPC, and that may be disrupted under harsh detergent conditions.

I therefore developed a protocol for affinity-purification of the heptameric Nup84 complex followed by size-exclusion chromatography, with the following objectives: (i) recovery of intact complexes, (ii) purity, and (iii) minimization of detergent use. An overview of the purification protocol is shown in **Figure 10**.

During size-exclusion chromatography, the heptameric complex eluted as one slightly asymmetric peak (**Figure 11**a). On-line multi-angle light scattering indicated a molecular mass of 574.9 kDa for the peak, consistent with a single heptamer. The chromatography fraction indicated by dashed lines in (**Figure 11**a) was analyzed by SDS-PAGE and

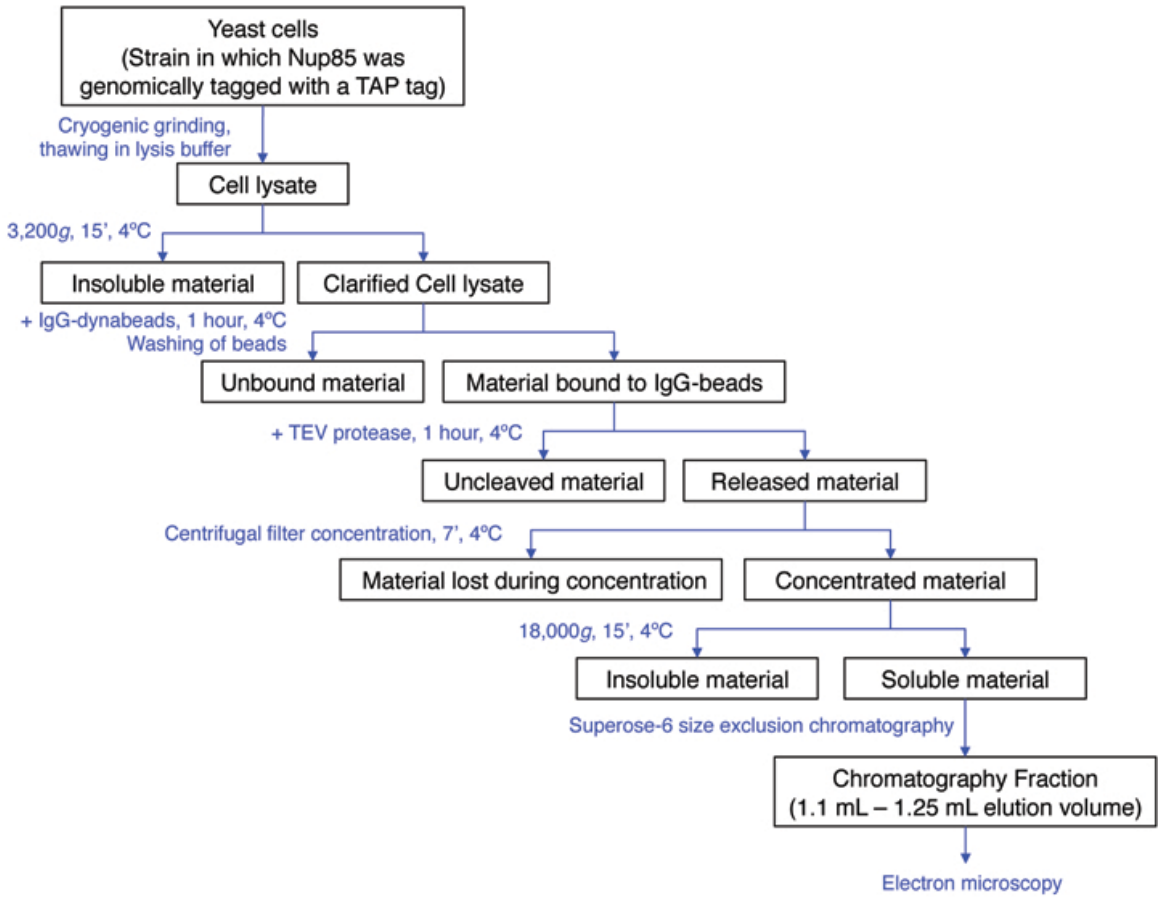

Figure 10 Purification Strategy for the Nup84 complex from budding yeast. For details of the protocol, see Chapter 5.

Figure 11 Purification and electron microscopy of the heptameric Nup84 complex. (**a**) Size exclusion chromatography profile of affinity-purified Nup84 complex released from IgG-beads by TEV protease cleavage. The fraction indicated by dashed lines contains Nup84 complex and was used for EM. (**b**) Coomassie-stained SDS-PAGE of the fraction from size exclusion chromatography indicated in (a). All bands were identified by mass spectrometry. Nup85-CBP is Nup85 C-terminally tagged with the calmodulin-binding peptide moiety of the TAP-tag, which was cleaved from the protein A moiety by TEV protease. (**c**) Negative-stain EM of heptameric complex particles. A field of particles adsorbed to glow-discharged carbon film and stained with 2% uranyl formate is shown.

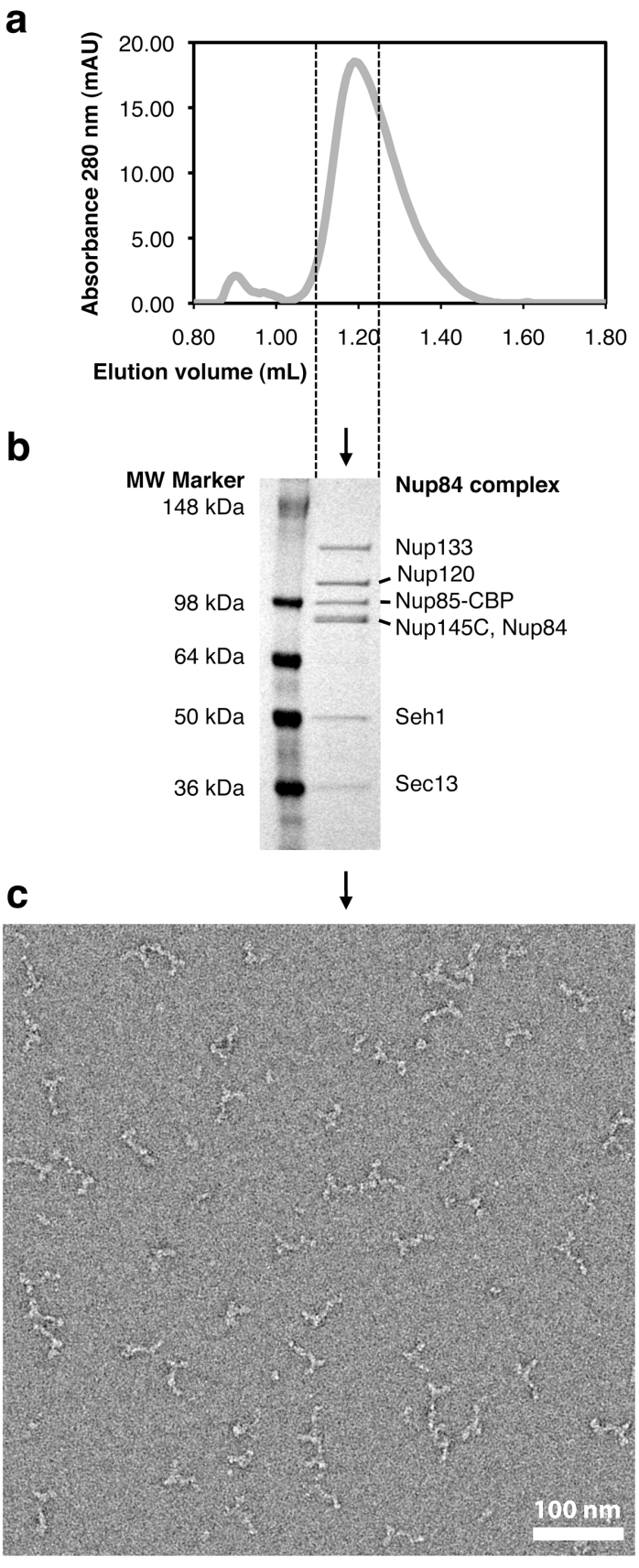
a
Absorbance 280 nm (mAU)
20.00
15.00
10.00
5.00
0.00
0.80
1.00
1.20
1.40
1.60
1.80
Elution volume (mL)
b
MW Marker
148 kDa
98 kDa
64 kDa
50 kDa
36 kDa
Nup84 complex
Nup133
Nup120
Nup85-CBP
Nup145C, Nup84
Seh1
Sec13
c
100 nm

Figure 11

the identity of each band was confirmed by mass spectrometry (**Figure 11**b). An aliquot of this material was applied to glow-discharged carbon-coated grids, negatively stained with uranyl formate, and subjected to EM (**Figure 11**c). As previously described (Lutzmann et al., 2002; Siniossoglou et al., 2000), the heptamer appeared as a Y-shaped particle.

2D analysis of particle structure and flexibility

EM images of 9,028 individual particles were subjected to automated reference-free alignment. Aligned particles were then computationally clustered into 90 classes, and particles within each class were averaged. The resulting class averages are shown in **Figure 12**. Inspection of the class averages revealed characteristic features of the heptameric complex (**Figure 13**).

The heptamer forms a ~45 nm long, branched structure with a short arm, a long arm and a stem meeting at a vertex. In most class averages, the stem appears kinked at two regions, referred to as stem hinge 1 (the vertex-proximal hinge) and stem hinge 2 (the vertex-distal hinge). Four globular regions with a diameter of ~5 nm are present at the end of the long and short arms, at the foot of the stem and as a knob next to the vertex.

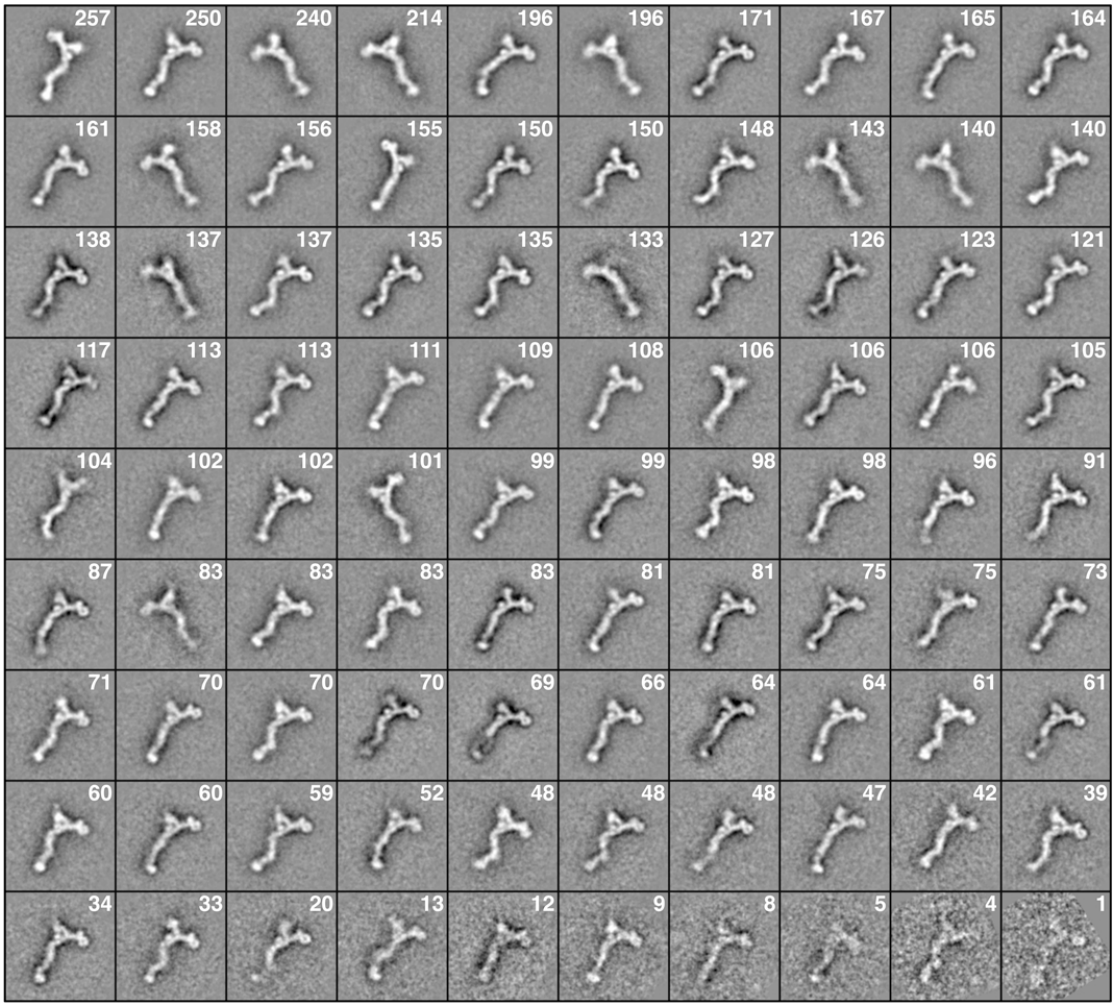

Figure 12 Alignment, classification and averaging of particle images. Reference-free alignment and k-means classification of 9,028 untilted particle images into 90 classes resulted in the depicted class averages. The number of particles constituting each class is indicated.

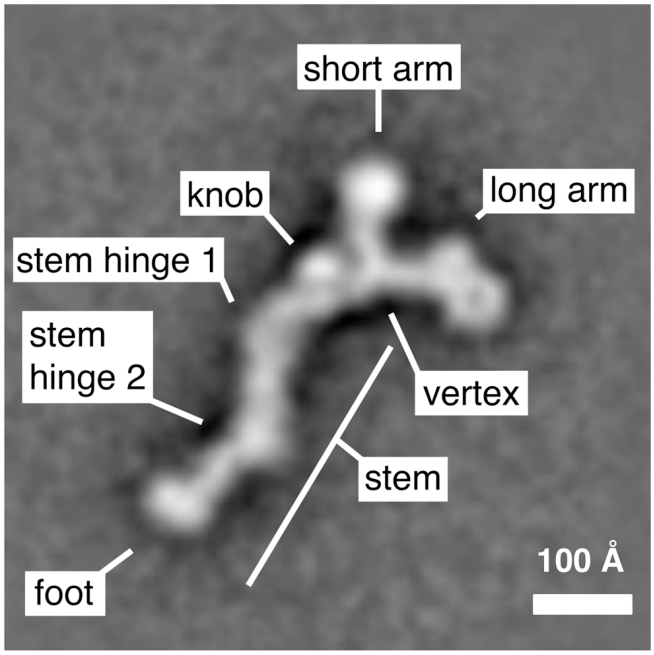

Figure 13 Structural details of the Nup84 complex. A well-defined class average is shown and prominent features are named.

Strikingly, the globular region at the tip of the long arm shows a central hole or depression and thus resembles a β-propeller in top view. The present 2D structure is consistent with the structure described by Lutzmann and colleagues (Lutzmann et al., 2002) but reveals more details since averaging of aligned particle images increased the signal-to-noise ratio.

The 2D class averages show a spectrum of different appearances (**Figure 12**), differing mainly in the angles between different segments of the particle. To analyze this variability, I determined angles

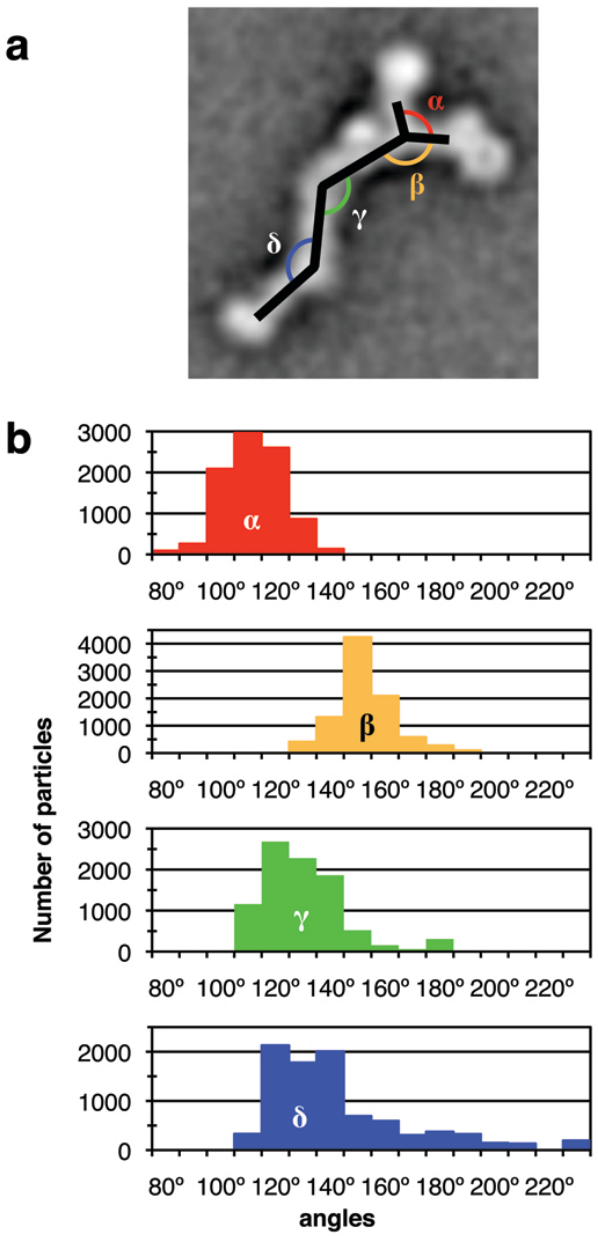

Figure 14 Heterogeneity of particle appearance. (**a**) Definition of angles between particle segments for the 2D view of untilted particles. α, angle between long and short arms; β, angle between long arm and vertex-proximal stem segment; γ, angle at stem hinge 1; δ, angle at stem hinge 2. (**b**) Distribution of angles for the 90 classes shown in **Figure 12**. Angles were measured for 2D class averages and assigned to the number of particles constituting each class.

between particle segments for the 90 class averages (**Figure 12**). Four angles were measured (**Figure 14**a): α (the angle between the two arms), β (the angle between the long arm and the vertex-proximal stem segment), γ (the angle at stem hinge 1), and δ (the angle at stem hinge 2). The angle between the short arm and the vertex-proximal stem segment equals 360º–(α+β), and is therefore not separately analyzed.

Analysis of the 90 classes revealed a continuum of angles between particle segments (**Figure 14**b). The highest variability between 2D class averages was observed at the two stem hinges, especially stem hinge 2. Angles γ and δ at the stem hinges varied from ~110º to ~180º, and from ~110º to ~230º, respectively (**Figure 14**b), causing the stem appearance to vary from straight to kinked. The angles around the vertex, α and β, also vary considerably: from ~80º to ~140º, and from ~130º to ~190º, respectively (**Figure 14**b).

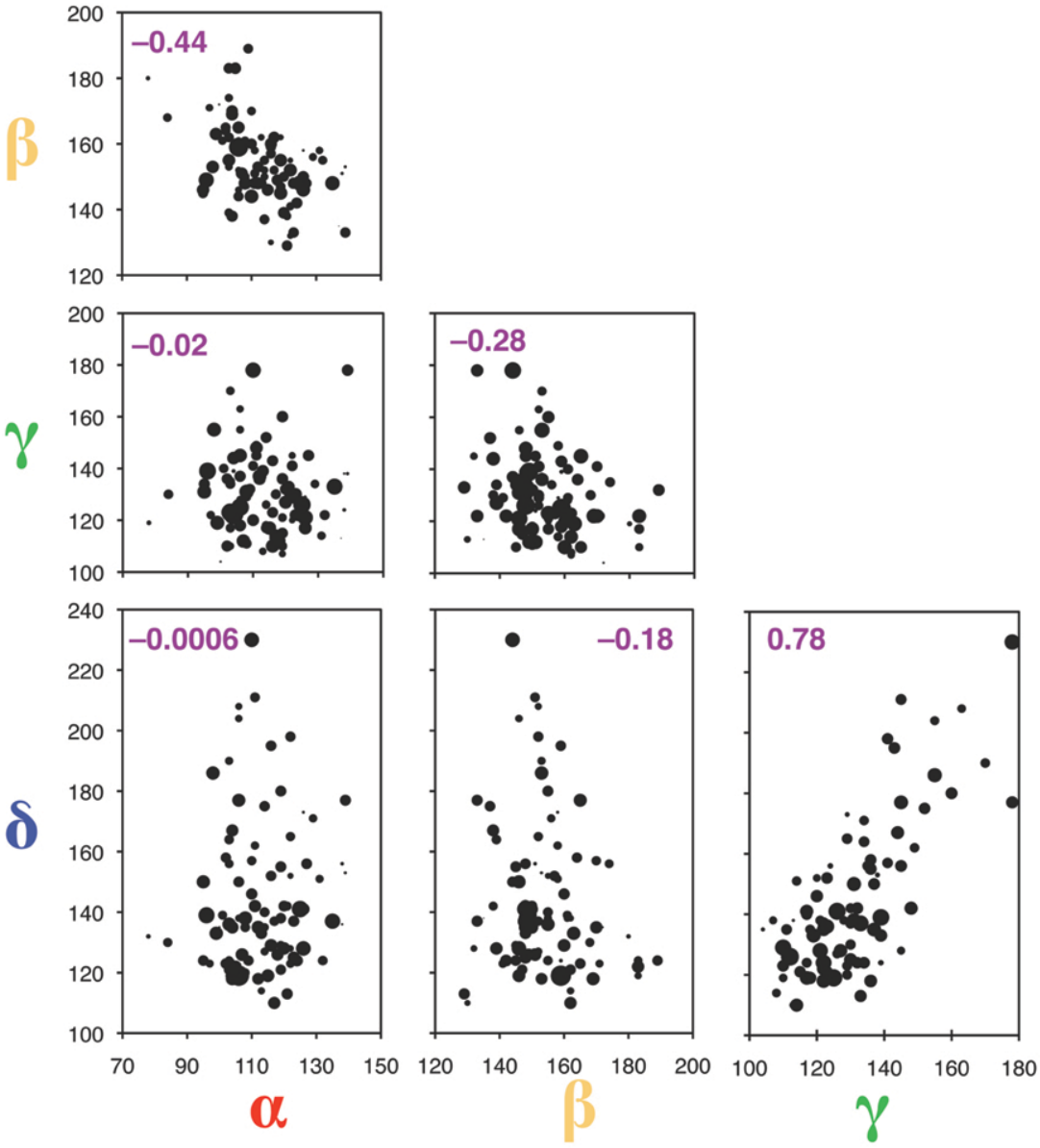

Figure 15 Correlations between particle angles. Angles between particle segments, as defined for untilted particles in **Figure 14**a. All binary combinations of angles α, β, γ and δ are plotted; each marker represents two angles for a particle class. Marker area is proportional to class size. Particle-based correlation coefficients are indicated in purple.

The angles at the stem hinges, γ and δ, are positively correlated with a correlation coefficient of 0.78 (**Figure 15**): most particles appear to have either a straight stem or a stem kinked at both hinges; stems kinked atone hinge and straight at the other hinge were not commonly observed. This suggests either that a large stem region undergoes a rigid-body movement, or that conformational changes at the two stem hinges are coupled. Other pairs of angles between particle segments do not correlate strongly (**Figure 15**), and principal component analysis indicates that correlated changes of the stem hinge angles γ and δ explain 73% of the measured angular variance (**Figure 16**). Weak anti-correlation between α and β (–0.44) can be rationalized by the fact that the sum of α, β, and the angle between short arm and vertex-proximal stem is fixed at 360°.

The foot region also shows conformational flexibility, as evidenced by the varying position of the foot with respect to the adjacent stem segment, and the fuzzy appearance in several class averages, which is indicative of in-class variation (**Figure 12**). Since the foot appears as a globular shape without discernible internal features, I could not reliably determine its orientation with respect to the stem and therefore abstained from quantitative analysis of variability in the foot region.

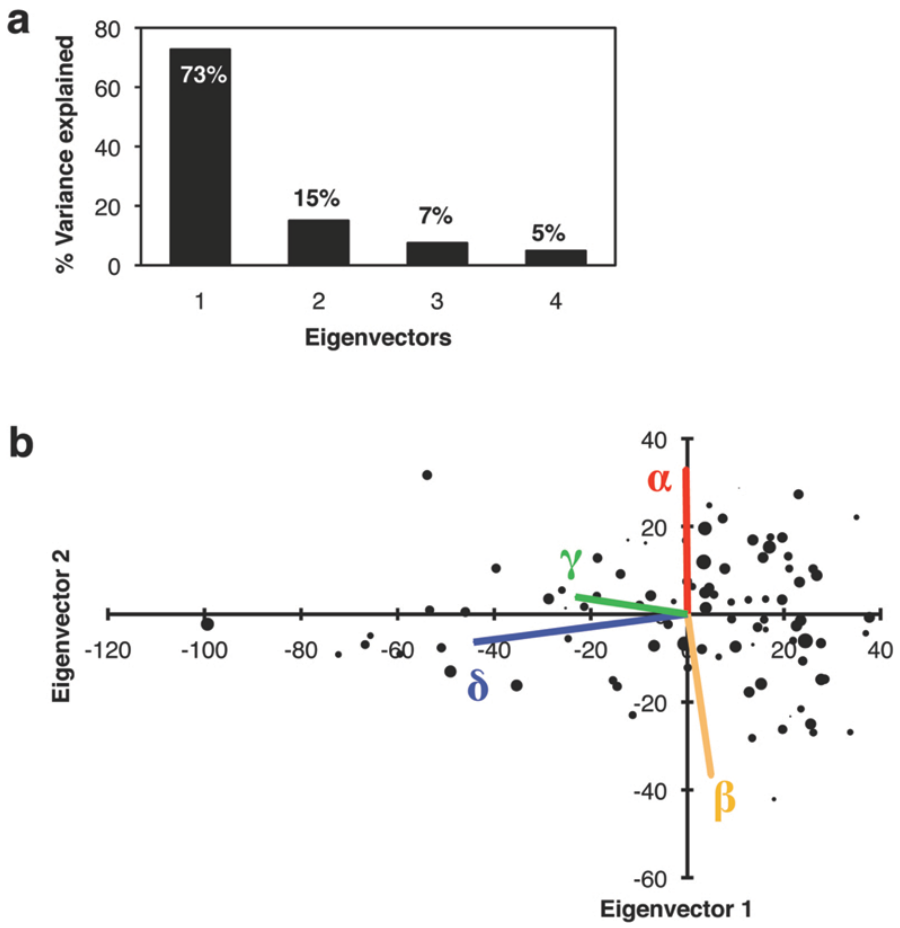

Figure 16 Principle component analysis (PCA) of the variation of angles α, β, γ and δ between particle segments (see also **Figure 14** and **Figure 15**). (**a**) Eigenvector 1 explains 73% of the variance; the remaining three eigenvectors explain the residual 27% of the variance. (**b**) Biplot: The black dots correspond to the original data projected onto the plane defined by the first two eigenvectors. The projections of the four original dimensions (angles) onto this plane are indicated by colored lines. Eigenvector 1 represents mainly the correlated variation in γ and δ. Eigenvector 2 represents mainly the anti-correlated variation in α and β.

3D structures of the heptameric complex

The method of choice for the *de novo* determination of 3D structures by EM is random-conical tilt reconstruction (Radermacher et al., 1986): A field of particles is imaged once after tilting the sample by a known angle, in my case 50°, and a second time after returning the sample to an untilted position, and pairs of tilted and untilted views of the same particle are picked, as illustrated in **Figure 17**. Since the in-plane orientation of particles in untilted images is random, the tilted images show a range of different particle views. Untilted particle images are used to classify particles and determine their in-plane orientation, and tilted particle images are used to reconstruct the 3D structure of the particle.

The 9,028 untilted particle images analyzed above were all taken in conjunction with tilted images of the same particles. The continuum of different conformations present in the heptamer population poses a challenge to 3D reconstruction. Ideally, a conformationally homogeneous class of particles should be used for reconstruction. At the same time, a class comprising a large number of particles is desirable to improve signal-to-noise ratio and angular coverage for random-conical tilt reconstruction. The number of particles chosen for a 3D reconstruction is thus a trade-off between homogeneity and signal-to-noise ratio. I approached the problem as follows: Untilted particle were grouped into larger classes by hierarchical

clustering, and two relatively homogeneous classes encompassing 497 and 608 particles, respectively, were chosen for random conical tilt reconstruction (**Figure 18**a).

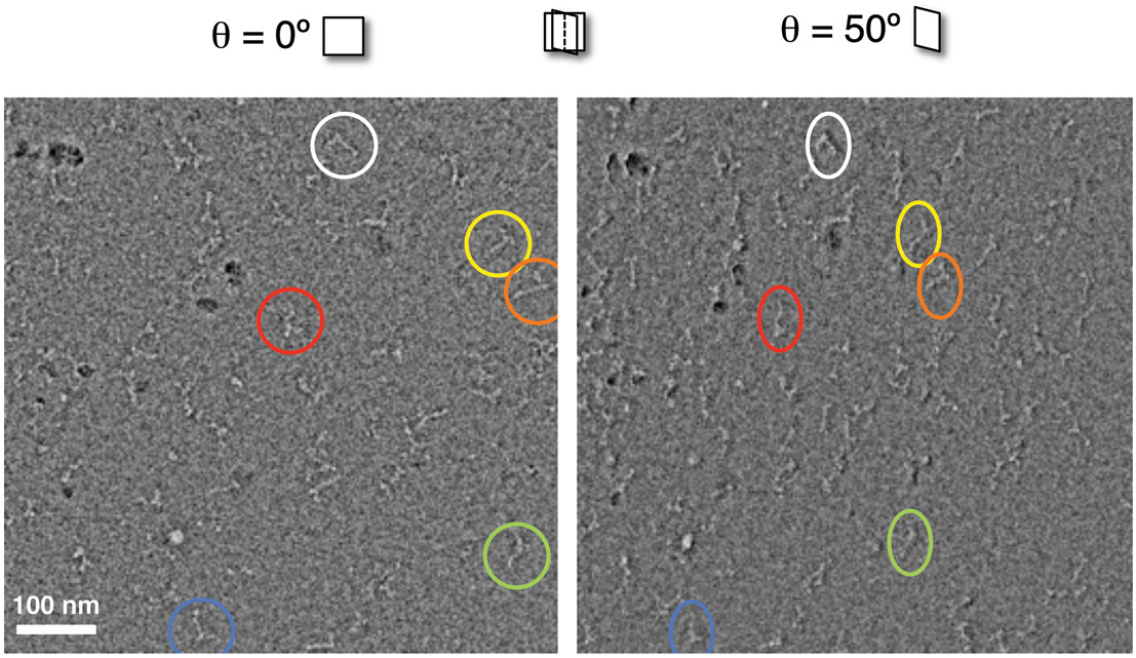

Figure 17 Micrograph tilt pair. A field of negatively stained particles was imaged at 50° and 0° tilt. Pairs of tilted and untilted views of the same particle were picked as illustrated by white ovals.

Figure 18 3D structures of the heptameric complex. (a) 9,028 untilted particle images were grouped by hierarchical ascendant classification and the two depicted classes, comprising 497 and 608 particles, respectively, were chosen for random conical tilt reconstruction. (b) Initial maps obtained by random conical tilt reconstruction from the classes shown in (a) are depicted as isodensity contour surfaces that were low-pass filtered beyond the reproducible resolution (FSC = 0.5 at 1/58 Å-1, see **Figure 22**). (c) The initial maps were used as references for projection matching of all 9,028 tilted particle images (see text for details and **Figure 19**). 4,430 particles aligned to initial map 1, and 4,598 particles aligned to initial map 2. 3D maps 1 and 2 were obtained by the simultaneous iterative reconstruction technique, and are shown in two views as isodensity contour surfaces low-pass filtered beyond the reproducible resolution (FSC = 0.5 at 1/35 Å-1, see **Figure 22**).

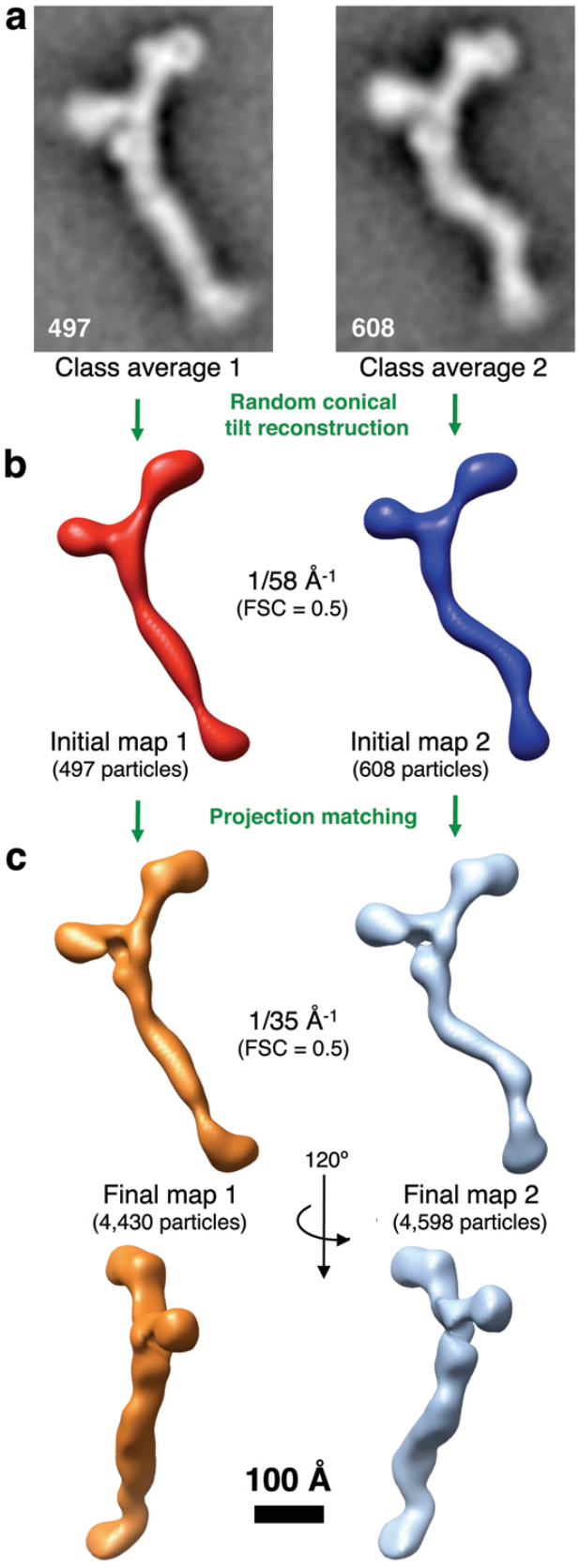
a
497
608
Class average 1
Class average 2
Random conical tilt reconstruction
b
1/58 Å-1
(FSC = 0.5)
Initial map 1
(497 particles)
Initial map 2
(608 particles)
Projection matching
c
1/35 Å-1
(FSC = 0.5)
120°
Final map 1
(4,430 particles)
Final map 2
(4,598 particles)
100 Å

Figure 18

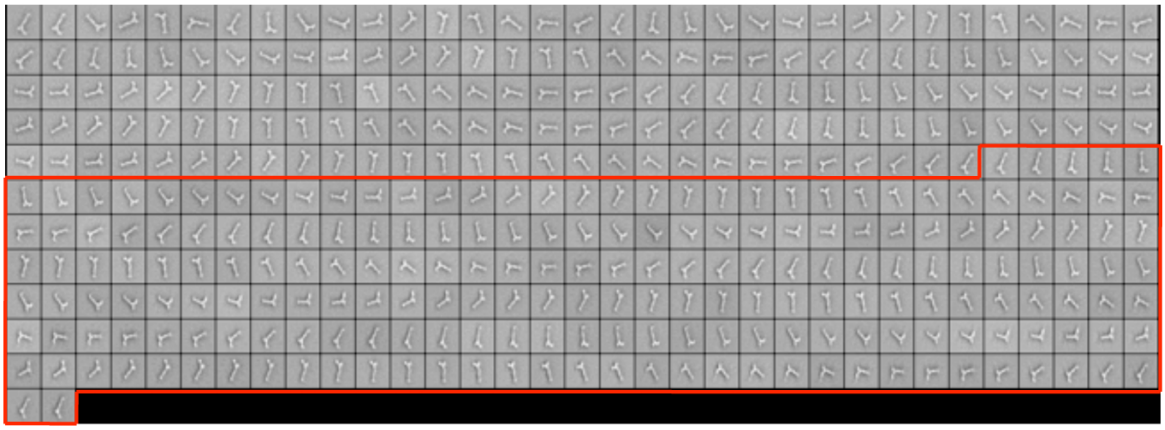

Projections of Initial Map 1

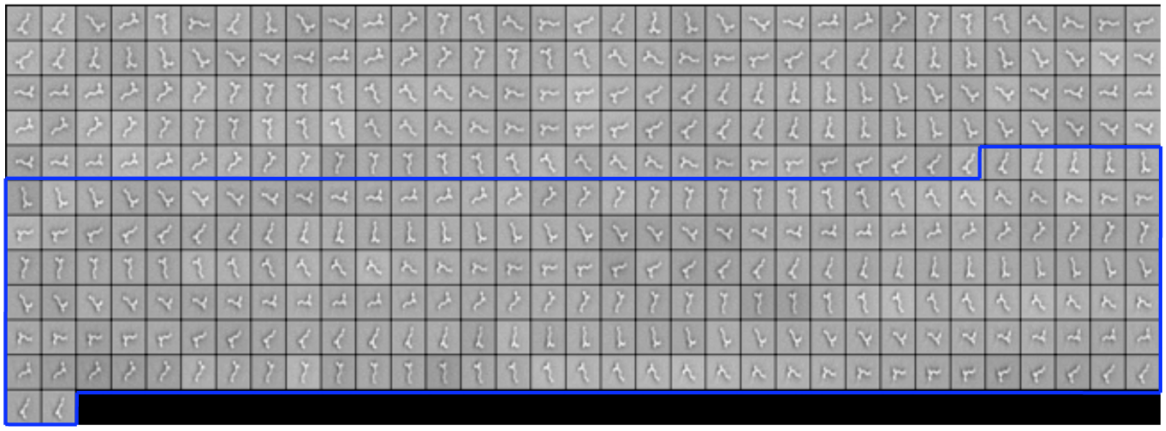

Projections of Initial Map 2

Figure 19 Projections calculated from initial maps 1 and 2. Projections were calculated in 5° increments up to a tilt angle of 55°. Projections between tilt angles of 40° and 55° (as indicated by red and blue boxes) were used for projection matching.

Figure 20 Cross-correlation-based projection matching. (**a**) Each grey dot represents one image of a particle from the tilted specimen. The non-normalized cross-correlation coefficient between the particle and the best-matching reference projection from initial map 2 is plotted versus the non-normalized cross-correlation coefficient between the particle and the best-matching reference projection from initial map 1. Red and blue dots represent particles from the classes that were used to construct initial maps 1 and 2, respectively. The diagonal (x=y) divides the particles into two sets of particles: those that have a higher score for alignment to a projection from initial volume 1 and were used for the reconstruction of final map 1 (dots below the diagonal), and those that have a higher score for alignment to a projection from initial volume 2 and were used for the reconstruction of final map 2 (dots above the diagonal). For control purposes, volumes were also reconstructed from subsets of particles that represented the 50% or 25% of the particles in each set with the highest cross-correlation coefficients for alignment to the best reference projection. (**b**) Maps obtained by projection matching and simultaneous iterative reconstruction using for each map the 25% of particles which aligned to the initial maps with the highest cross-correlation coefficients (see text for details). 4a (**c**) Final maps obtained by projection matching and simultaneous iterative reconstruction using all particles. All structures are depicted to scale as isodensity contour surfaces that were low-pass filtered beyond the reproducible resolution.

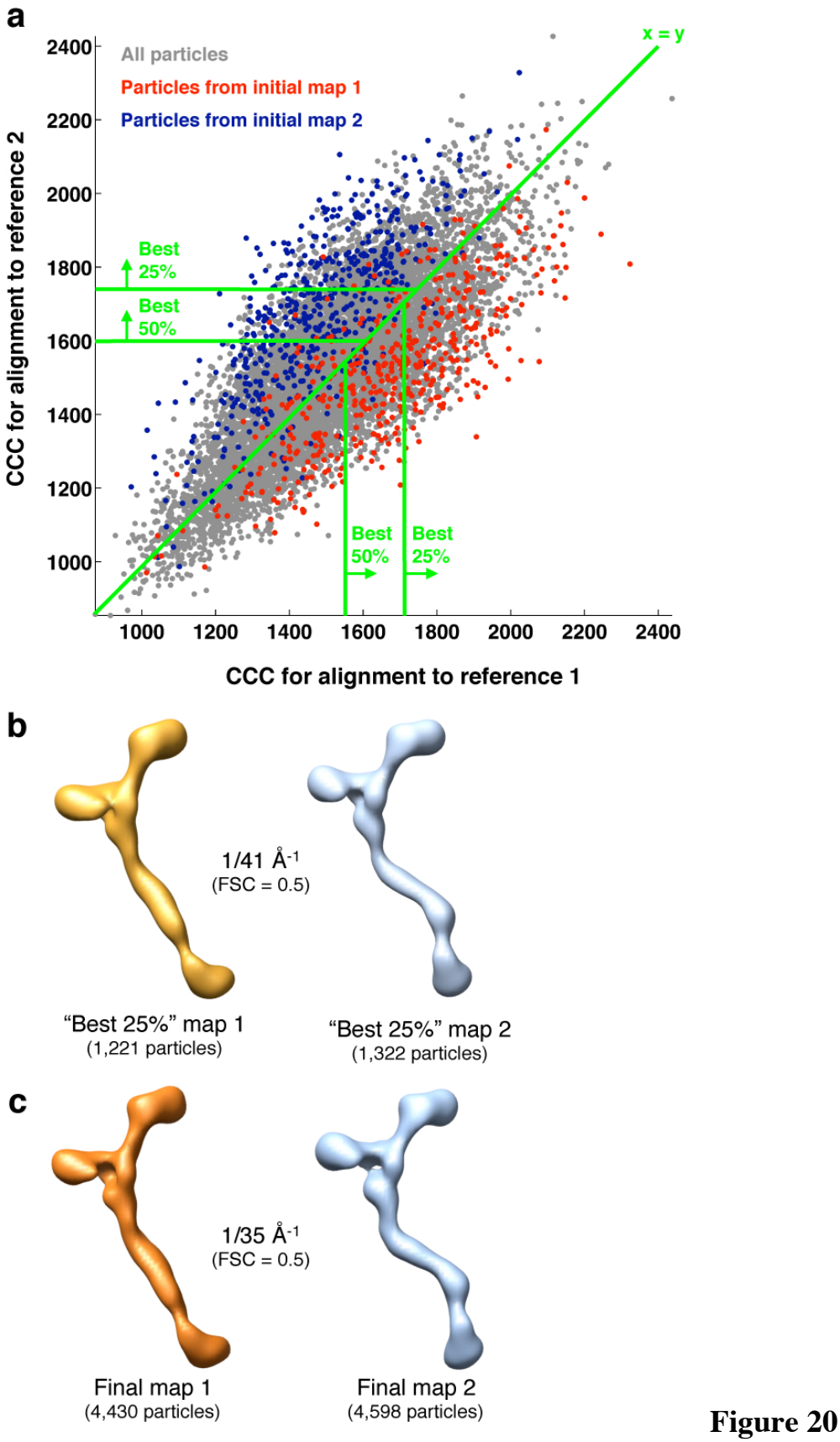
a
All particles
Particles from initial map 1
Particles from initial map 2
x = y
Best 25%
Best 50%
Best 50%
Best 25%
CCC for alignment to reference 2
CCC for alignment to reference 1
2400
2200
2000
1800
1600
1400
1200
1000
1000 1200 1400 1600 1800 2000 2200 2400
b
1/41 Å-1
(FSC = 0.5)
"Best 25%" map 1
(1,221 particles)
"Best 25%" map 2
(1,322 particles)
c
1/35 Å-1
(FSC = 0.5)
Final map 1
(4,430 particles)
Final map 2
(4,598 particles)

Figure 20

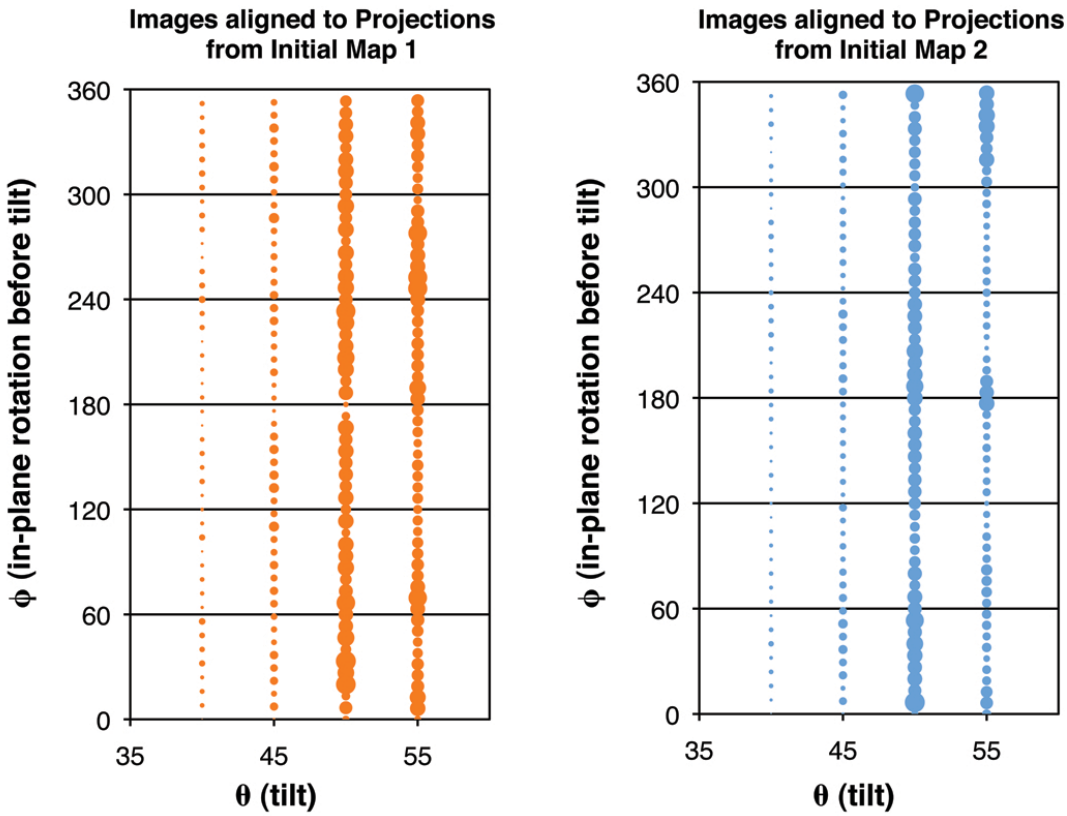

Figure 21 Angular coverage for final maps 1 and 2. Bubble plots showing the distribution of tilted particle images between projections from initial maps 1 and 2. Each projection is characterized by the angles ϕ (in-plane rotation before tilt) and θ (tilt). Bubble size is proportional to the number of particles aligned to each projection. In total, 4,430 particles aligned to initial map 1, and 4,598 particles aligned to initial map 2.

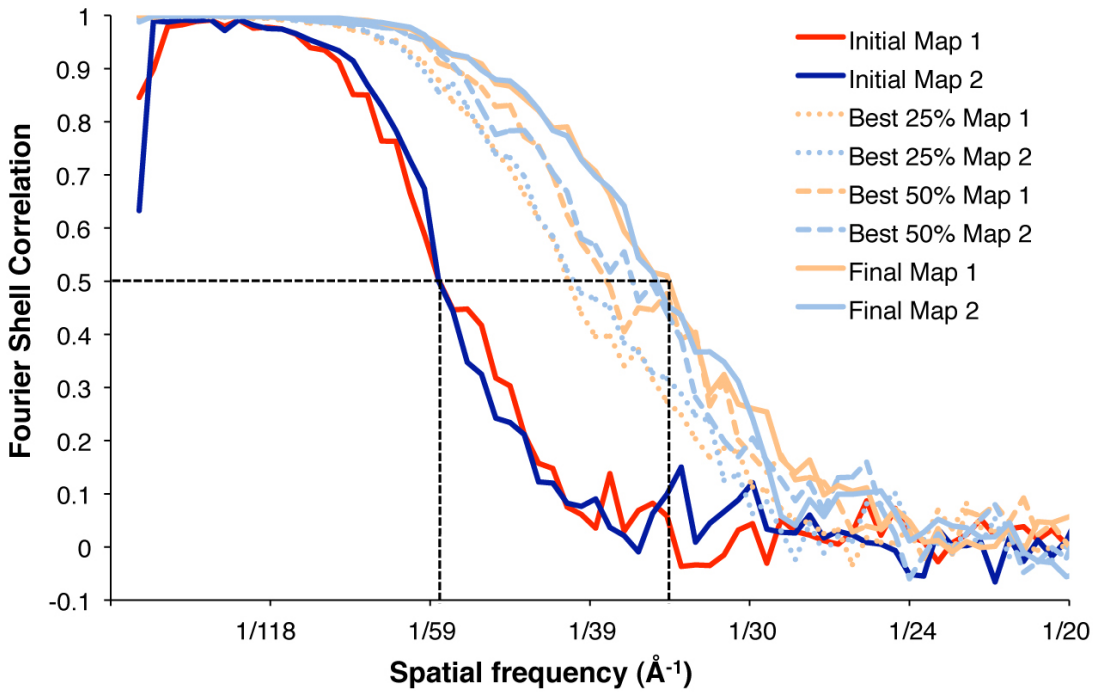

Figure 22 Fourier Shell Correlation (FSC) for initial and final maps 1 and 2, as well as control maps that were reconstructed by projection matching, only using the best-matching 25% or 50% of particles, as shown in Supplementary Figures 4,5. The reproducible resolution, as defined by FSC=0.5, is ~58 Å for the initial maps and ~35 Å for the final maps.

3D maps were generated by random conical tilt reconstruction (**Figure 18**b). The reproducible resolution of these initial 3D maps is ~58 Å as determined by the 0.5 Fourier-Shell correlation (FSC) criterion (**Figure 22**). My next goal was to increase the signal-to-noise ratio of the initial maps by incorporating more tilted particle images. I hypothesized that some of the variation in particle appearance is likely to be caused by slight differences in

the particle orientation with respect to the carbon support. Therefore, additional particles are likely to have a similar conformation to the particles constituting the two initial maps, and the signal-to-noise ratio of the initial maps may be improved by incorporating additional particle images.

I proceeded as follows: Projection images were created from the two initial maps (**Figure 19**), and all tilted particle images were matched to one of these projections based on the highest correlation coefficient. 4,430 particles aligned best to initial map 1 and 4,598 particles aligned best to initial map 2. **Figure 20**a shows the cross-correlation coefficients (CCC) for alignment of each particle to the best-matching reference projection from both initial maps (grey dots). Each particle was assigned to either map 1 or map 2 to maximize the CCC. **Figure 21** shows the numbers of particles corresponding to each projection.

Red and blue dots in **Figure 20**a correspond to the particles that were used to construct initial maps 1 and 2, respectively. Of the particles used for initial map 1, 86% have a higher CCC for alignment to initial map 1 projections than to initial map 2 projections; they lie below the x=y diagonal in **Figure 20**a. Of the particles used for initial map 2, 91% lie above the diagonal. Therefore, the CCC is a suitable criterion to distinguish the two different particle conformations.

Interestingly, the CCC distributions of particles used to reconstruct initial maps 1 and overlap with the CCC distribution of all other particles, supporting the idea that some of the other particles are likely to represent different views of a particle in the same (or a highly similar) conformation as initial maps 1 and 2.

However, the CCC distributions are unimodal; therefore, it is not possible to find by inspection a correct threshold to distinguish between particles with a conformation corresponding to the reference map and particles with a different conformation. This finding is compatible with my conclusion that there is a continuous spectrum of particle conformations.

I therefore independently reconstructed maps from three subsets for each map 1 and map 2 using the simultaneous iterative reconstruction technique (Gilbert, 1972). The subsets contained the 25% particles with the highest CCCs, the 50% particles with the highest CCCs, or all particles. The maps obtained from these subsets are highly similar (**Figure 20**b,c).

The Fourier shell correlation (FSC) curves for all maps are compared in **Figure 22**. The reproducible resolution of the maps, as defined by FSC=0.5, increases monotonically with the number of particles used for the reconstruction. I therefore decided to use the final maps 1 and 2

(reconstructed from all particle images), with a reproducible resolution of ~35 Å, for further analysis.

The 3D structures confirm that the isolated heptameric complex is a flexible particle that can exist in different conformations (**Figure 18**bc): map 1 corresponds to a "straight-stem" conformation and map 2 to a "kinked-stem" conformation. In both conformations, the particle lies relatively flat on the carbon support film. It is possible that binding of the particle to the planar support restricts its conformational flexibility, and that the complex displays an even greater conformational variability in solution.

I attempted to characterize the 3D structure of the heptameric complex in solution by collecting cryo-EM images of vitrified samples. Unfortunately, I was not able to detect the particle by either cryo-EM or negative-stain cryo-EM, probably due to the low contrast provided by the thin, extended shape of the particle.

Nup positions within the heptameric complex

The localization of several nups or nup complexes to different segments of the Nup84 complex was reported by Hurt and colleagues (Lutzmann et al., 2002), and further supported by crystallographic studies (Boehmer et al., 2008; Brohawn et al., 2008; Debler et al., 2008; Hsia et al., 2007).

Specifically, the following aspects of Nup84 complex architecture were previously established:

(i) Nup145C·Sec13 and Nup85·Seh1 are stable heterodimers (Lutzmann et al., 2002) in which the seventh blade of the Sec13 and Seh1 β-propellers is contributed by Nup145C and Nup85, respectively (Brohawn et al., 2008; Debler et al., 2008; Hsia et al., 2007).

(ii) Nup120 can form trimers with Nup145C·Sec13 and with Nup85·Seh1, and together, these five proteins can form a pentamer which appears in EM as a triskelion with three short arms, and can thus be concluded to correspond to the two arms and the vertex-proximal stem segment of the heptameric complex (Lutzmann et al., 2002).

(iii) Nup84 forms a dimer with Nup133 (Lutzmann et al., 2002); more specifically, these two nups interact via their C termini (Boehmer et al., 2008).

(iv) Nup133·Nup84 forms a tetramer with Nup145C·Sec13. Nup84 alone, as well as the Nup133·Nup84 dimer bind the Nup120·Nup145C·Sec13·Nup85·Seh1 pentamer, thereby extending one of the three arms into the elongated stem (Lutzmann et al., 2002). Taken together, these observations show that the two arms of the heptameric complex are formed by Nup120 and Nup85·Seh1, which are connected to

Nup145C·Sec13 at the vertex region. Nup145C·Sec13 forms the upper part of the stem, Nup84 the mid-stem and Nup133 the distal stem and the foot.

I described here the asymmetric appearance of the two arms of the heptameric complex. Since previous data did not allow us to deduce which arm corresponds to Nup120 and which to Nup85·Seh1, I addressed this question experimentally. I genomically tagged the C terminus of Seh1 with green fluorescent protein (GFP) and purified the heptameric complex from this modified yeast strain.

Furthermore, I chose to tag N- or C-termini of other proteins that are part of available crystal structures: the C-terminus of Sec13 (Hsia et al., 2007), and the N- and C-termini of Nup133 (Berke et al., 2004; Boehmer et al., 2008). GFP tagging did not interfere with nuclear envelope localization *in vivo* (**Figure 23**) or with complex purification, with one exception: GFP-tagging of Sec13 greatly reduced recovery of heptameric complex, which prevented me from collecting data from this version of the complex.

EM images were collected for the other three GFP-tagged complexes, and aligned class averages of GFP-tagged and untagged particles were compared. Areas of statistically significant differences corresponding to the GFP density could be localized (**Figure 24**).

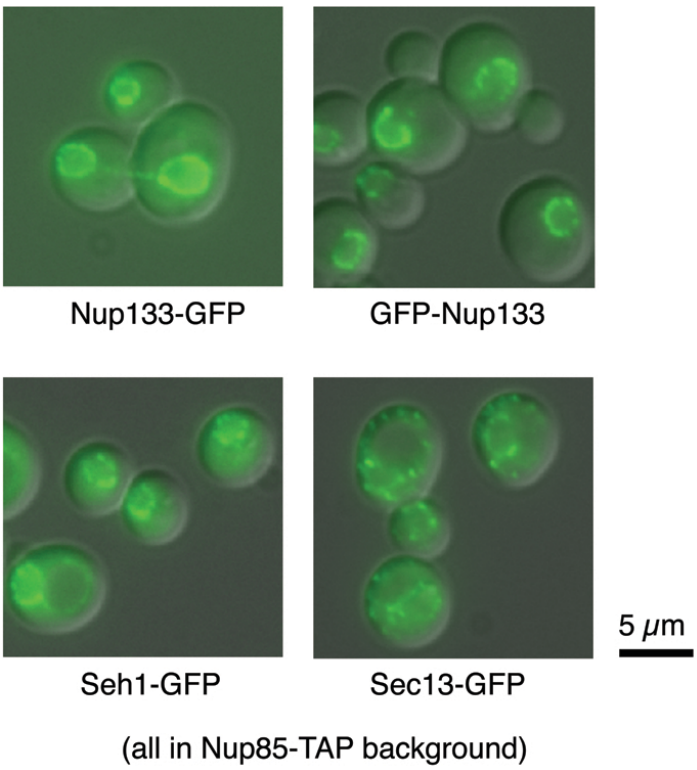

Figure 23 Localization of GFP-tagged nups in vivo. Micrographs of yeast strains that were used for the purification of GFP-tagged heptameric complex. Overlay of GFP fluorescence (green) and phase contrast (grayscale). Nup133-GFP and GFP-Nup133 show the nuclear rim staining pattern typically observed for NPC-localized proteins. Sec13-GFP shows cytoplasmic localization in addition to the nuclear rim staining, as expected based on its localization to both the NPC and COPII coats. Seh1-GFP is localized mainly to the nuclear rim; a small fraction may also be localized to other endomembranes.

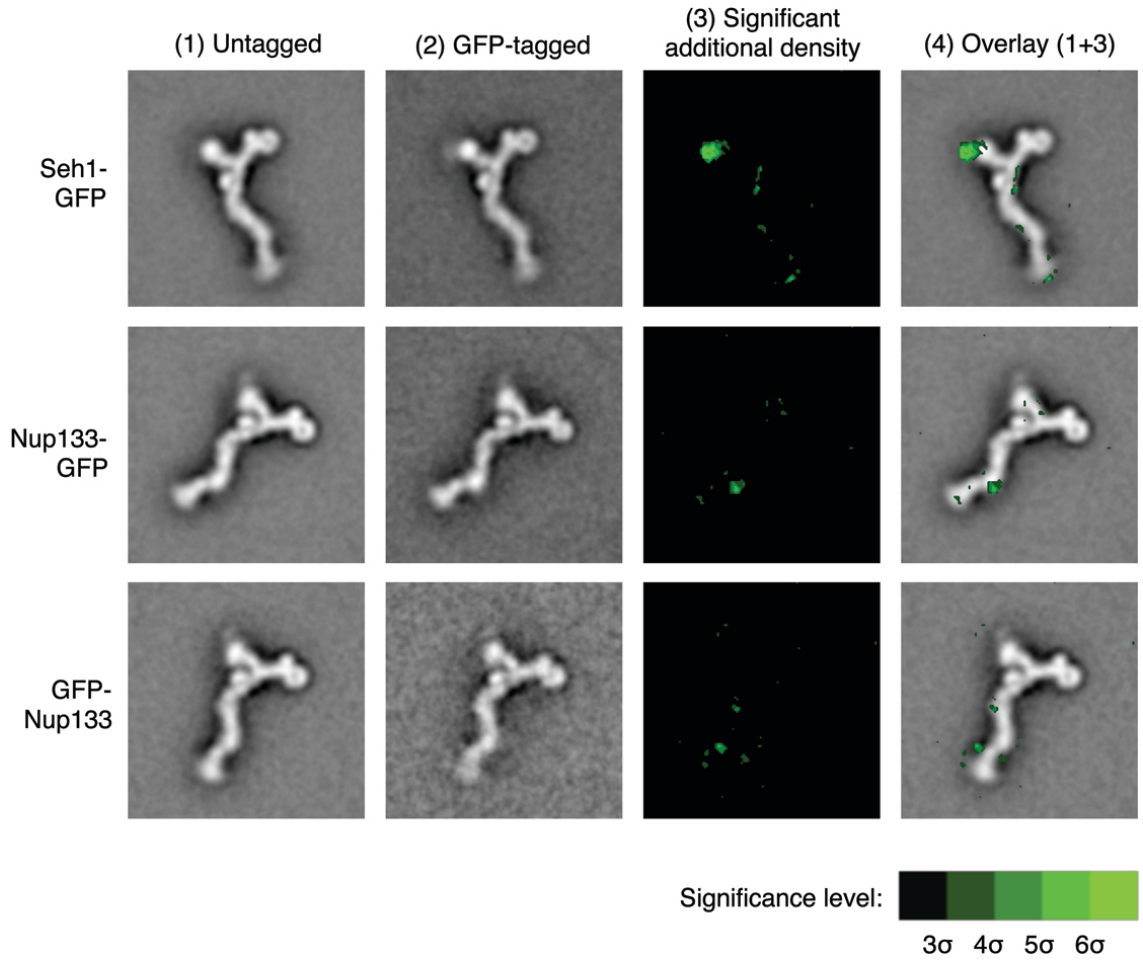

Figure 24 Mapping of nup localization. Heptameric complexes were purified from yeast strains in which one protein of the subcomplex was genomically tagged with GFP: the C-terminus of Seh1 (first row), the C-terminus of Nup133 (second row) or the N-terminus of Nup133 (third row). Aligned class averages of untagged and GFP-tagged particles are shown in columns (1) and (2). The significance map column (3) shows extra density for the GFP-tagged particles above multiples of the pixel-based standard deviation of the class averages. Column (4) shows an overlay of columns (1) and (3).

In the case of Seh1-GFP, the GFP appears to be rigidly attached to the rest of the particle, resulting in a defined additional density approximately the size of the GFP protein, at the tip of the short arm. For the other GFP-tagged particles, the GFP density appears more fuzzy and delocalized, likely because of a greater flexibility of the attached GFP in these cases. The C-terminus of Nup133 coincides with stem hinge 2. The GFP attached to the N-terminus of Nup133 gives the most diffuse signal, but the largest coherent area of additional density is localized on the distal stem segment, between stem hinge 2 and the globular foot domain.

These localization maps, in conjunction with established interactions between members of the heptameric complex (Boehmer et al., 2008; Brohawn et al., 2008; Debler et al., 2008; Hsia et al., 2007; Lutzmann et al., 2002), enabled me to assign the identity of structural features of the heptameric complex as follows: Short arm, Nup85·Seh1; long arm, Nup120; vertex-proximal stem, Nup145C·Sec13, medial stem, Nup84; distal stem, Nup133. Thus, I confirmed the general nup arrangement proposed by Lutzmann and colleagues (Lutzmann et al., 2002) and elucidated the structure further by assigning the positions of nups within the two asymmetric arms.

EM map 2 was segmented according to this assignment (**Figure 25**) to indicate the approximate localization of nups. Some details, such as the exact interaction of Nup120, Nup145C and Nup85 regions at the vertex, are currently unknown and displayed tentatively.

Nup crystal structures docked into the EM map

I proceeded to dock known crystal structures of heptameric complex components into the 3D EM structure. Each crystal structure was computationally fitted into the EM map based on global 3D cross-correlation, without initial constraints. From the list of likely positions and orientations within the EM map generated by the algorithm, the highest-scoring fit that localized the crystal structure to the correct segment of the heptamer (as defined in **Figure 25**) was accepted, as illustrated in **Figure 26**. Docking was carried out independently for heptamer maps 1 and 2, and the resulting structures are shown in **Figure 27**, Details of the docked structures in map 2 are shown in **Figure 28**.

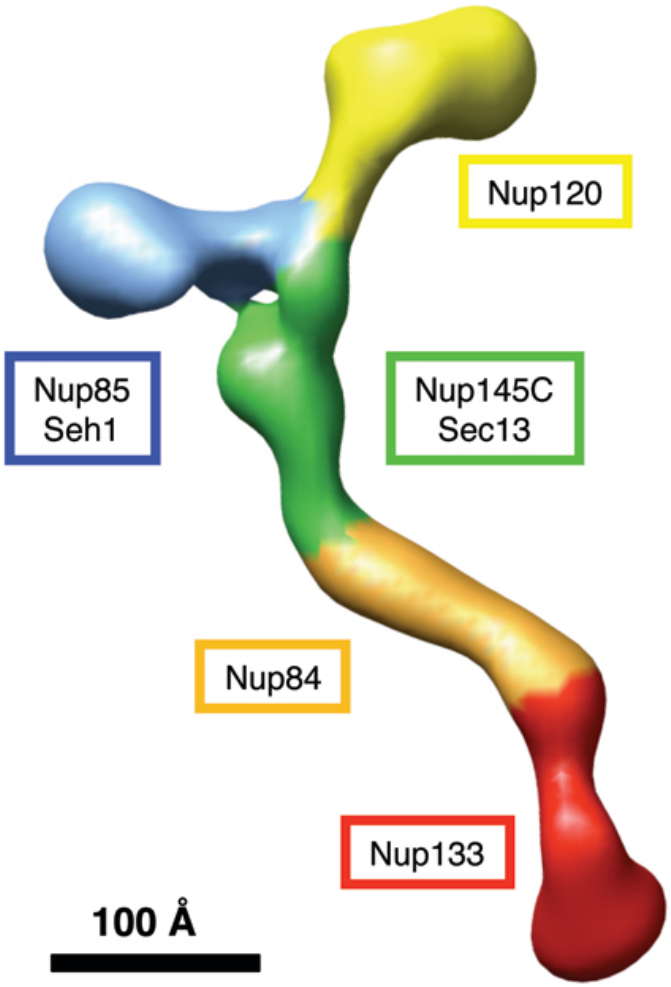

Figure 25 Segmentation of the particle (map 2) based on mapped nup localizations and previously established biochemical interactions. The particle surface is color-coded to represent the regions of the particle corresponding to different modules. Boundaries between regions are approximate.

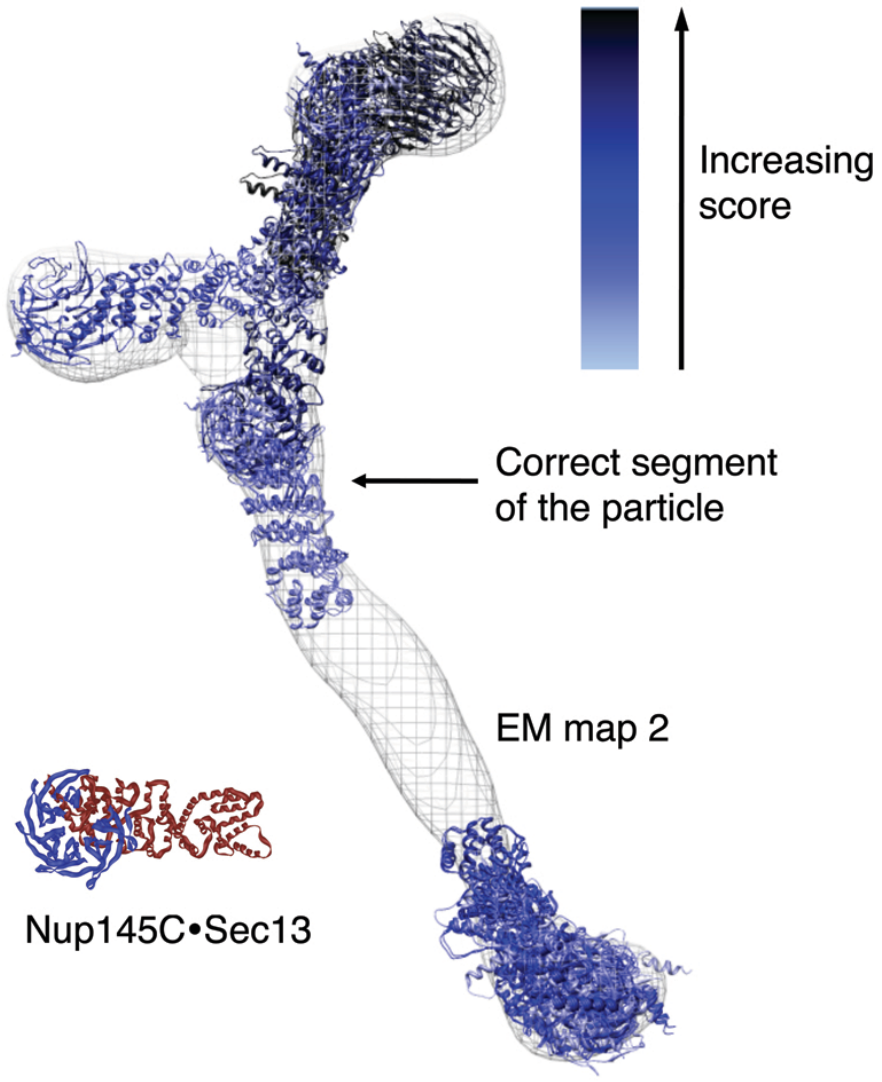

Figure 26 Crystal structure docking strategy, illustrated for Nup145C·Sec13. For objective docking, the crystal structure was fit globally into the EM map by the program Situs. The program returns a list of likely positions of the crystal structure within the EM map, ordered by a cross-correlation score indicating the quality of fit. Darker shades of blue indicated higher-scoring positions.

Figure 27 Docking of available crystal structures (ribbon representation) into the EM maps (isodensity contour mesh representation). Two views related by a 90º rotation around a vertical axis are shown. The crystal structures are of: yeast Nup85 (amino acids 1-570 of 744, dark blue) in complex with yeast Seh1 (full length, light blue) (Debler et al., 2008), yeast Nup145C (amino acids 125-555 of 711, dark green) in complex with human Sec13 (amino acids 1-316 of 322, light green) (Hsia et al., 2007), human Nup107 (the homologue of yeast Nup84, amino acids 658-925 of 925, orange) in complex with human Nup133 (amino acids 934-1156 of 1156, red) (Boehmer et al., 2008), and Nup133 (amino acids 76-478 of 1156, red) (Berke et al., 2004). The conformation of the Nup107·Nup133 fragment is likely to differ from the actual Nup84·Nup133 conformation in map 2, as evidenced by the poor fit, and the structure is included for illustrative purposes only. Empty regions in the particle map correspond to proteins and protein domains for which no crystal structure is available yet.

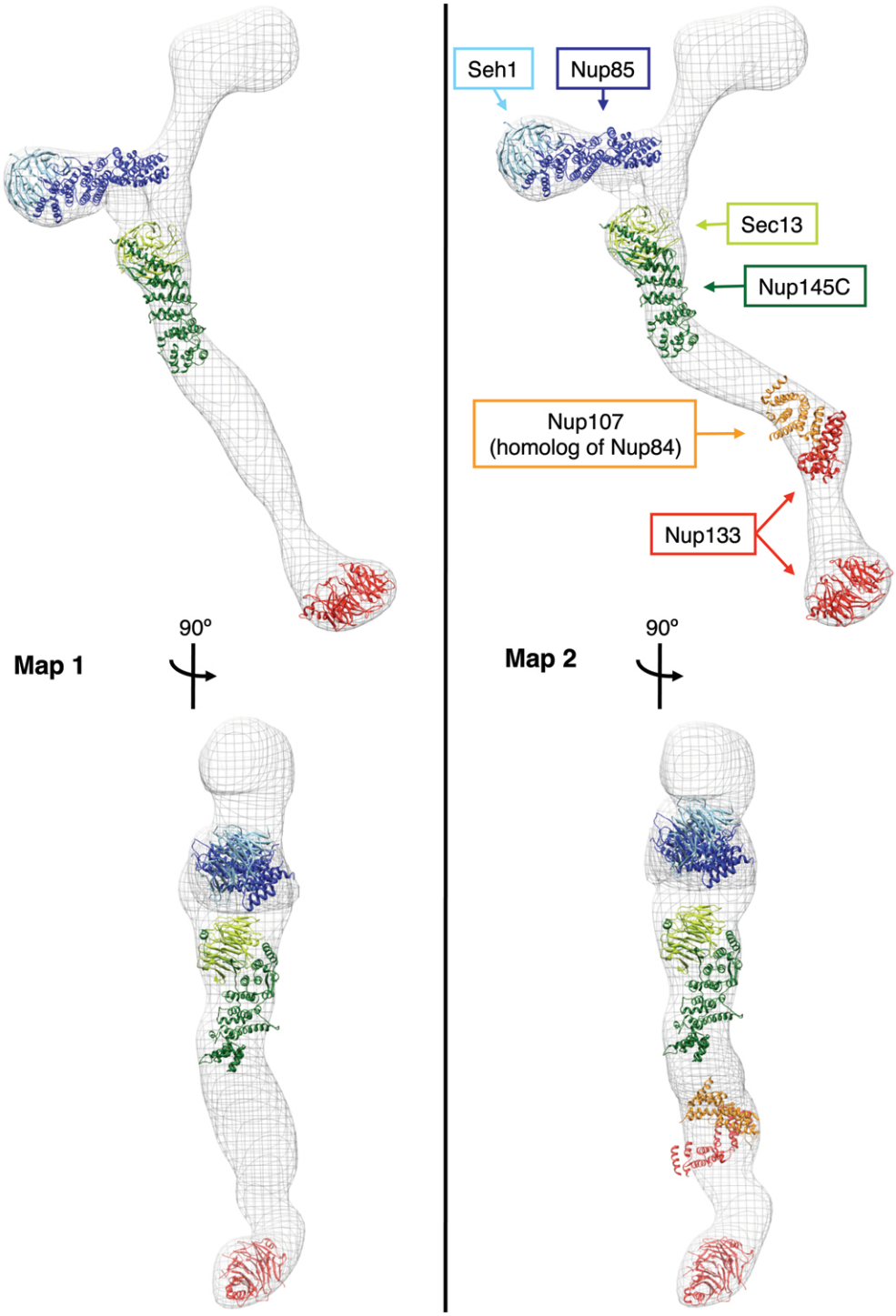
Seh1
Nup85
Sec13
Nup145C
Nup107
(homolog of Nup84)
Nup133
90°
Map 1
90°
Map 2

Figure 27

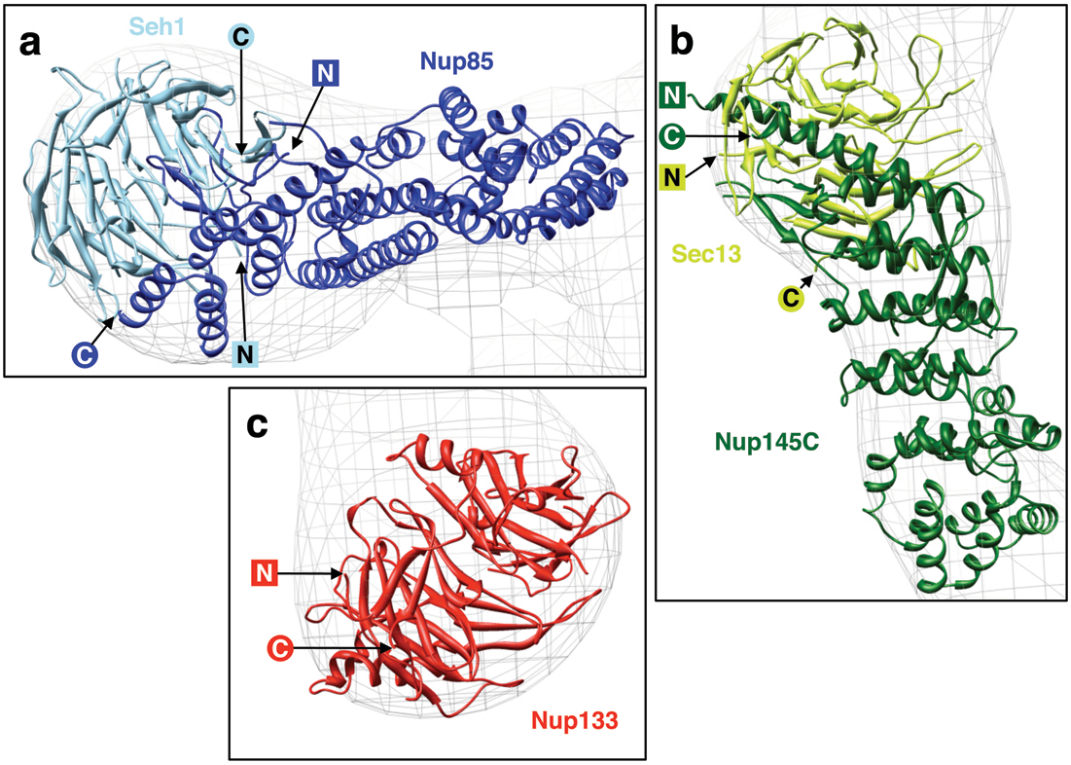

Figure 28 Detailed views of crystal structures docked into map 2; N- and C-termini of the crystallized nup domains are indicated. (**a**) Nup85·Seh1 (**b**) Nup145C·Sec13 (**c**) Nup133 β-propeller.

The Nup85·Seh1 dimer fit into the short arm of the heptamer (**Figure 28**a), and assumed highly similar positions in EM maps 1 and 2 (**Figure 27**). The Seh1 β-propeller corresponds to the thicker globular region at the end of the short arm; the α-solenoid regions of Nup85 localize to the thinner arm region. The crystal structure of Nup85 lacks 174 C-terminal amino acids. The C-terminus of the crystallized Nup85 fragment points

towards the end of the short arm (**Figure 28**a). Since the end of the short arm is occupied with the Seh1 β-propeller, additional C-terminal residues of Nup85 likely fold back towards the vertex region. The crystallized domain of Nup85 does not completely fill the short arm of the EM map, thus leaving space for the Nup85 C-terminus. However, the current resolution of the EM map is not sufficient to discern the exact location of the additional residues.

The Nup145C·Sec13 dimer localizes to the vertex-proximal stem region (**Figure 28**b), with highly similar orientations in maps 1 and 2 (**Figure 27**). The Sec13 β-propeller corresponds to the knob region. The crystal structure of Nup145C lacks 125 N-terminal amino acids and 156 C-terminal amino acids. Both the N- and C-terminus of the crystallized Nup145C fragment point towards the vertex of the heptamer (**Figure 28**b), suggesting that the region between the knob and the vertex is filled with the remaining portions of Nup145C. The middle part of Nup145 extends to the stem hinge 1 region of the heptamer, where it interacts with Nup84. This suggests that stem hinge 1 is formed at the interface between Nup145C and Nup84.

The N-terminal Nup133 β-propeller forms the globular foot region of the heptamer, in a similar orientation for maps 1 and 2 (**Figure 27** and **Figure 28**c). The N-terminal 66 amino acids of Nup133 are absent from

the crystal structure and presumably unstructured. The N-terminus of the crystallized Nup133 β-propeller domain points away from the foot, towards the stem region (**Figure 28**c), consistent with the observed localization pattern of the GFP-tagged N-terminus of Nup133 (**Figure 24**). The C-terminus of the crystallized Nup133 β-propeller domain points away from the stem; the following residues will have to fold back to connect to the remaining part of Nup133. Again, the resolution of the EM map is not high enough to predict the exact path taken by protein fragments absent from the crystal structure.

Since structures of yeast Nup133 and Nup84 have not been determined, I used the partial crystal structures of their human homologues Nup133 and Nup107 for docking. The crystal structure contains C-terminal fragments of Nup107 and Nup133. Since the C-terminus of Nup133 maps to stem hinge 2 (**Figure 24**), the crystal structure can be expected to be situated in this segment of the heptamer. The global fitting method failed for the Nup107·Nup133 structure: none of the computed positions coincided with stem hinge 2. Therefore, I positioned the crystal structure manually in this region and optimized the local fit computationally. The crystal structure does not fit neatly into the EM map (**Figure 27**). The likely explanation is that since stem hinge 2 is a conformationally flexible region, the conformation of

human Nup133·Nup107 in the crystal structure is somewhat different from the conformation of the homologous yeast Nup133·Nup84 in the particle conformation of map 2. Thus, the docking of the Nup133·Nup107 fragment is tentative, and mainly shown for illustrative purposes.

CHAPTER 3: Investigation of Nuclear Pore Complex Architecture and Dynamics in Live Cells by Polarized Fluorescence Microscopy

As outlined in Chapter 1, polarized fluorescence microscopy can yield information about the orientation and rotational diffusion of fluorophores, as well as the distances between fluorophores. Fluorescent labeling of NPC components may therefore provide insights into NPC dynamics and architecture in live cells, and into the mechanism by which FG domains function in NPC gating. In the first three sections of this chapter, I will discuss theoretically how fluorescence anisotropy measurements of GFP-tagged nups in live cells can reveal aspects of NPC architecture and dynamics. In collaboration with Alexa Mattheyses, Claire Atkinson and Sanford Simon (The Rockefeller University), we established techniques for the acquisition and computational analysis of polarized fluorescence microscopy measurements of GFP-tagged nups in live yeast cells. These techniques, as well as first results, will be presented in the remaining sections of this chapter.

Effects of orientation of GFP-tagged nups within the NPC on fluorescence anisotropy: Theory

Fluorescence anisotropy in macroscopically ordered systems has been investigated previously for different geometries (Axelrod, 1979; Rocheleau et al., 2003; Vrabioiu and Mitchison, 2006, 2007). In this section, I will apply previous theoretical results to quantitatively derive how the microscopically measured fluorescence anisotropy of GFP rigidly attached to nups depends on the orientation of GFP within the NPC.

The nuclear envelope is assumed to be a sphere, and a central cross-section of the sphere is imaged. The coordinate system ***xyz*** is defined with respect to the microscope (**Figure 29**). ***z*** is the optical axis, and ***y*** is the direction of the electric field dipole of the polarized exciting light. The coordinate system ***NPQ*** is defined with respect to the nuclear pore complex (**Figure 30**). ***N*** is the nucleo-cytoplasmic axis, which always lies in the ***xy*** plane since a central section of the nuclear envelope is imaged. ***P*** is chosen to be parallel to ***z***, which places ***Q*** in the ***xy*** plane. ***PQ*** is the plane of the nuclear envelope. The position of a NPC along the nuclear envelope cross-section can be described by γ, the angle between ***N*** and ***y***.

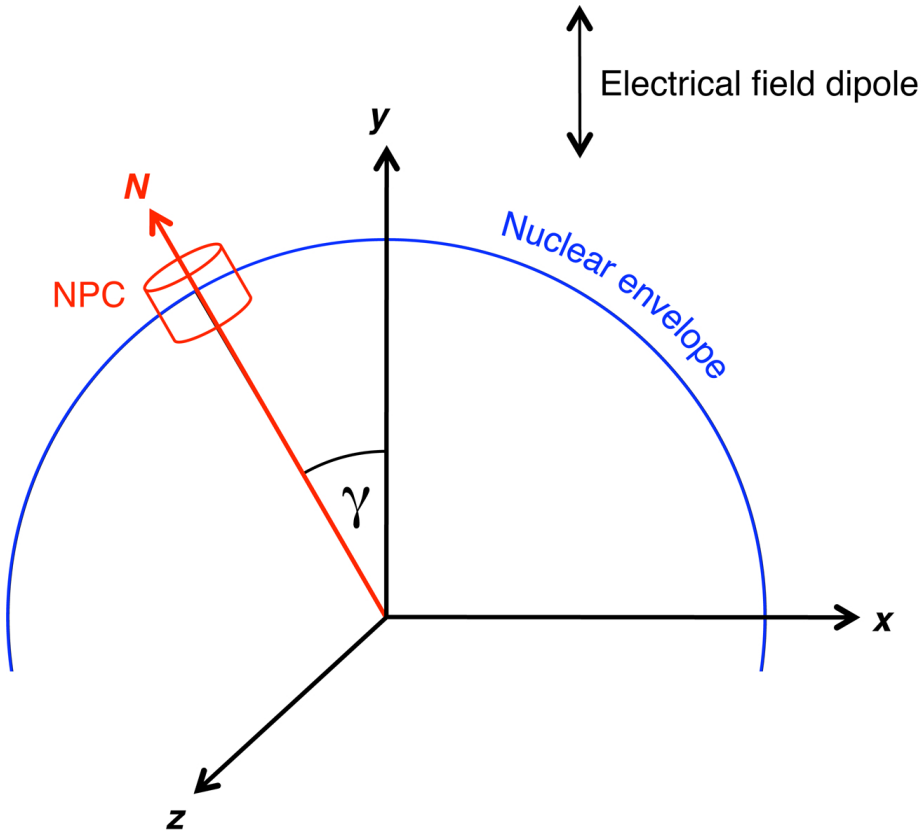

Figure 29 Microscope-fixed coordinate system. The orthogonal coordinate system ***xyz*** is fixed with respect to the microscope. ***z*** is parallel to the optical axis and ***y*** is parallel to the electric field vector of the exciting light. The focal plane is chosen such that the nuclear envelope is imaged as a central cross section. The position of a NPC along the nuclear cross-section is defined by the angle γ between the ***y*** axis and ***N***, the eight-fold symmetry axis of the NPC. ***N*** always lies in the ***xy*** plane and is normal to the nuclear envelope plane.

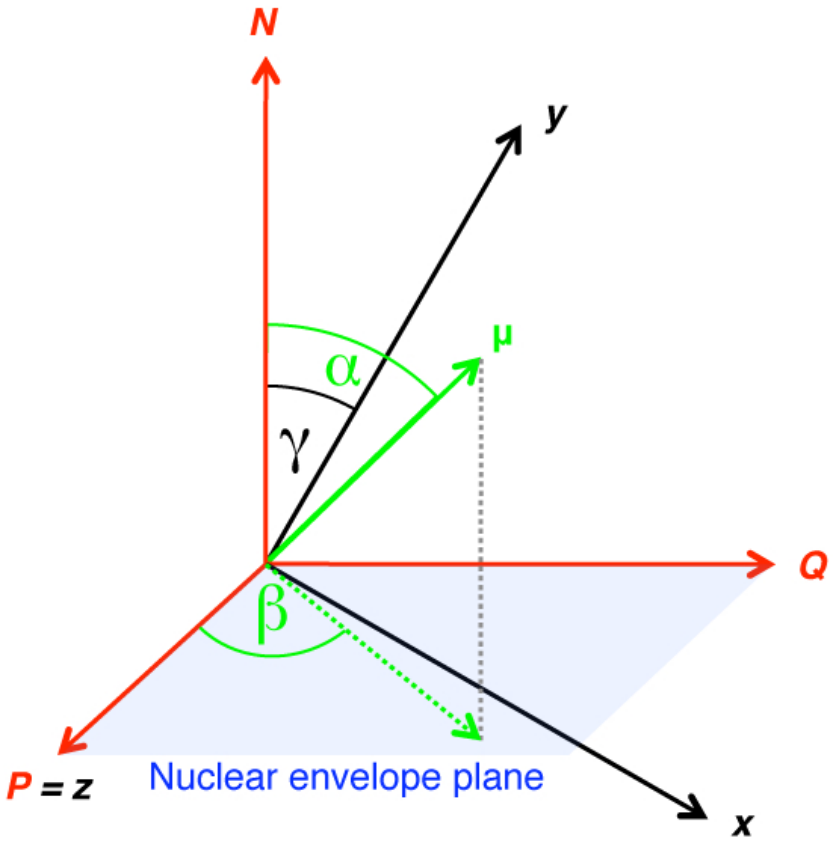

Figure 30 NPC-fixed coordinate system. The orthogonal coordinate system ***NPQ*** is fixed with respect to an individual NPC. ***P*** is chosen to be parallel with the optical axis ***z***. ***P*** and ***Q*** span the nuclear envelope plane. ***NPQ*** can be transformed into ***xyz*** by a rotation of γ around ***P***. The orientation of a fluorophore with excitation transition dipole **μ** within the NPC is characterized by two angles, α and β. α is the angle between ***N*** and **μ**; β is the angle between ***P*** and the projection of **μ** onto the ***PQ*** plane.

The excitation transition dipole **μ** of a fluorophore rigidly attached to the NPC can be defined by two angles: α, the angle between **μ** and the nucleo-cytoplasmic axis ***N***, and β, the angle between ***P*** and the projection of **μ** onto the nuclear envelope plane ***PQ***. I chose to express fluorophore dipole

orientation using these two angles, since the representation of the eight-fold symmetry of the NPC around ***N*** is particularly elegant in this notation: eight fluorophores labeling all copies of the same nup will have $\boldsymbol{\mu}_j$ dipoles with

[3.1] $$\alpha_j = \alpha_1 \text{ and } \beta_j = \beta_1 + (j-1)\tfrac{\pi}{4} \text{ for j} = 1, \ldots, 8 .$$

Vectors $\boldsymbol{\mu}$, $\boldsymbol{x}$, $\boldsymbol{y}$ and $\boldsymbol{z}$ can be expressed as unit length vectors in the ***NPQ*** coordinate system:

[3.2] $$\mu = \begin{pmatrix} \cos\alpha \\ \sin\alpha \cdot \cos\beta \\ \sin\alpha \cdot \sin\beta \end{pmatrix}$$

[3.3] $$\boldsymbol{x} = \begin{pmatrix} -\sin\gamma \\ 0 \\ \cos\gamma \end{pmatrix}$$

[3.4] $$\boldsymbol{y} = \begin{pmatrix} \cos\gamma \\ 0 \\ \sin\gamma \end{pmatrix}$$

[3.5] $$\boldsymbol{z} = \begin{pmatrix} 0 \\ 1 \\ 0 \end{pmatrix}$$

The fluorophore transition dipole $\boldsymbol{\mu}$ has the following $\boldsymbol{x}$, $\boldsymbol{y}$ and $\boldsymbol{z}$ components:

[3.6] $$\mu_x = \frac{\boldsymbol{\mu} \cdot \boldsymbol{x}}{|\boldsymbol{\mu}||\boldsymbol{x}|} = \sin\alpha \cdot \sin\beta \cdot \cos\gamma - \cos\alpha \cdot \sin\gamma$$

[3.7] $$\mu_y = \frac{\boldsymbol{\mu} \cdot \boldsymbol{y}}{|\boldsymbol{\mu}||\boldsymbol{y}|} = \cos\alpha \cdot \cos\gamma + \sin\alpha \cdot \sin\beta \cdot \sin\gamma$$

[3.8] $$\mu_z = \frac{\boldsymbol{\mu} \cdot \boldsymbol{z}}{|\boldsymbol{\mu}||\boldsymbol{z}|} = \sin\alpha \cdot \cos\beta$$

For each individual fluorophore, the probability $p_{\boldsymbol{\mu}}$ of being excited by polarized light is proportional to $\boldsymbol{\mu}_y^2$, since the energy of an electric field is proportional to the square of the electric field vector. Thus:

[3.9] $$p_{\boldsymbol{\mu}} \propto \boldsymbol{\mu}_y^2 = (\cos\alpha \cdot \cos\gamma + \sin\alpha \cdot \sin\beta \cdot \sin\gamma)^2$$

Whereas α is a parameter specific to the geometry of fluorophore attachment to the nup, and γ depends on the region of the nuclear envelope that we investigate, the probability distribution of β can be assumed to be uniform

over [0 , 2π]. Therefore, we can calculate *f*, the fraction of the fluorophores that will be excited on average, as follows:

[3.10] $$f(\alpha,\gamma) = \frac{1}{2\pi}\int_0^{2\pi} p_{\mu}(\alpha,\beta,\gamma)d\beta$$

After substituting with equation [3.9] and solving the integral, we obtain:

[3.11] $$f(\alpha,\gamma) = \cos^2\alpha\cdot\cos^2\gamma + \frac{1}{2}\cdot\sin^2\alpha\cdot\sin^2\gamma$$

Note that *f* does not depend on β, and thus the eightfold symmetry of the NPC around ***N*** does not affect the result:

[3.12] $$f_{NPC} = \frac{1}{8}\sum_{j=0}^{7} f(\beta = \beta_0 + \frac{\pi}{4}j) = f(\gamma)$$

Likewise, in the case of sixteen nups, where eight nups are related to the eight other nups by a rotation of 180° around an axis within the nuclear envelope plane, the results are not affected: α for the additional eight nups is obtained by adding π to the α value for the first eight nups, and $f(\alpha+\pi) = f(\alpha)$. This property of *f* is expected, since dipoles are invariant with respect to rotation by π.

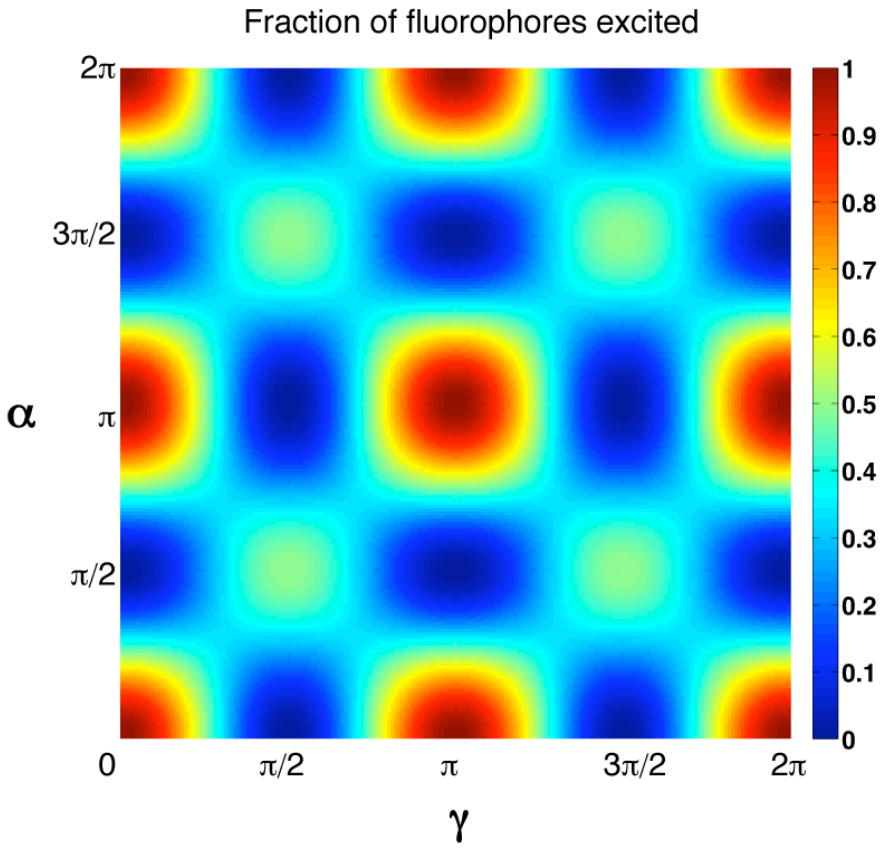

Figure 31 Graph of *f*, the fraction of fluorophores excited by polarized light, as a function of α (the angle between the fluorophore excitation transition dipole and the nucleo-cytoplasmic axis of the NPC) and γ (the angle between the nucleo-cytoplasmic axis of the NPC and the electric field dipole of the exciting light).

The family of functions $f_\alpha(\gamma)$ is displayed in **Figure 31**. To localize minima and maxima along the nuclear envelope cross-section, we calculate the first two derivatives of *f* with respect to γ:

[3.13] $$\frac{\partial f}{\partial \gamma} = (1 - 3 \cdot \cos^2 \alpha) \cdot \cos \gamma \cdot \sin \gamma$$

[3.14] $$\frac{\partial^2 f}{\partial \gamma^2} = (3 \cdot \cos^2 \alpha - 1) \cdot (1 - 2 \cdot \cos^2 \gamma)$$

For any choice of parameter α (with one exception), we find the following two points to be critical points:

[3.15] $$\gamma_1 \equiv 0 + n \cdot \pi$$

[3.16] $$\gamma_2 \equiv \tfrac{\pi}{2} + n \cdot \pi$$

The exception occurs for

[3.17] $$\alpha^* \equiv \pm \arccos \frac{1}{\sqrt{3}} + n \cdot \pi$$

since

[3.18] $$f_{\alpha^*}(\gamma) = \frac{1}{3} = const$$

that is, for the exact orientation α^* of the fluorophores, their excitation becomes independent on the position of the NPC along the nuclear envelope cross-section.

For $|\alpha| < \arccos\frac{1}{\sqrt{3}}$, γ_1 is a maximum point and γ_2 is a minimum point; for $|\alpha| > \arccos\frac{1}{\sqrt{3}}$, the situation is reversed. Hence, for any fixed α, the largest difference between values is found between $f_\alpha(\gamma_1)$ and $f_\alpha(\gamma_2)$, and this difference will be referred to as $\Delta f(\alpha)$:

[3.19] $$\Delta f(\alpha) \equiv f_\alpha(\gamma_1) - f_\alpha(\gamma_2)$$

In combination with equation [3.11], we obtain:

[3.20] $$\Delta f(\alpha) = \cos^2\alpha - \tfrac{1}{2}\sin^2\alpha$$

This function has the maximum points

[3.21] $$\alpha_1 = 0 + n \cdot \pi$$

and the minimum points

[3.22] $\alpha_2 = \frac{\pi}{2} + n \cdot \pi$

These points represent special cases of $f_\alpha(\gamma)$, which I will now discuss.

(i) α_1: All fluorophore dipoles are parallel to the nucleo-cytoplasmic axis

When the fluorophore excitation transition dipoles are parallel to the nucleo-cytoplasmic axis ($\alpha = \alpha_1 = 0 + n \cdot \pi$) equation [3.11] becomes:

[3.21] $f_{\alpha_1}(\gamma) = \cos^2 \gamma$

For NPCs with their nucleo-cytoplasmic axis parallel to the direction of the polarized light, all fluorophores are excited, $f_{\alpha_1}(\gamma_1) = 1$. For NPCs with their nucleo-cytoplasmic axis perpendicular to the direction of the polarized light, none of the fluorophores are excited: $f_{\alpha_1}(\gamma_2) = 0$. Therefore, $\Delta f(\alpha_1) = 1$, which is the maximal value of Δf.

(ii) α_2: fluorophore dipoles are parallel to the nuclear envelope

When the fluorophore transition dipoles are parallel to the nuclear envelope $(\alpha = \alpha_2 = \frac{\pi}{2} + n \cdot \pi)$, equation [3.11] becomes:

[3.22] $$f_{\alpha_2}(\gamma) = \tfrac{1}{2} \cdot \sin^2 \gamma$$

Now fluorophores in NPCs with their nucleo-cytoplasmic axis parallel to the direction of the polarized light are not excited, $f_{\alpha_2}(\gamma_1) = 0$. Half of the fluorophores in NPCs with their nucleo-cytoplasmic axis perpendicular to the direction of the polarized light are excited: $f_{\alpha_2}(\gamma_2) = \frac{1}{2}$, $\Delta f(\alpha_2) = -\frac{1}{2}$.

Thus far, we have characterized the fraction of fluorophores that are excited by polarized light. In a typical experimental setup for polarization microscopy, the emitted light is passed through an analyzer or polarizing beam splitter, such that $I_{\parallel}$, the light intensity parallel to ***y***, the electric field component of the exciting light, can be quantified separately from $I_{\perp}$, the light intensity perpendicular to ***y*** and parallel to ***x***. $I_{\parallel}$ and $I_{\perp}$ depend on the orientation of the emission transition dipole of the fluorophore, which I will assume to be identical to the excitation transition dipole $\boldsymbol{\mu}$. This assumption is valid if the excitation transition occurs between

the same two electrical states as the emission transition. In the case of GFP, this has been shown experimentally to be a fair assumption (Rocheleau et al., 2003; Volkmer et al., 2000).

Equations [3.6-3.8] then apply directly to the ***x, y*** and ***z*** components of the transition emission dipole $\boldsymbol{\mu}$ of an excited fluorophore. The ***x, y*** and ***z*** components of the light intensity emitted by this fluorophore are proportional to the squares of the dipole components, $\boldsymbol{\mu}_x^2$, $\boldsymbol{\mu}_y^2$, $\boldsymbol{\mu}_z^2$. To obtain the relative average light intensity components for all fluorophores at given α and γ, we need to multiply the light intensity components from a fluorophore oriented at angle β with the probability that this fluorophore was excited by the polarized light (equation [3.9]), and then integrate over all β:

[3.23] $$I_x = \frac{1}{2\pi}\int_0^{2\pi} \boldsymbol{\mu}_x^2 p_{\boldsymbol{\mu}} d\beta = \frac{1}{2}a^2c^2 + a^2d^2 + \frac{3}{8}b^2c^2 + \frac{1}{2}b^2d^2 - 2abcd$$

[3.24] $$I_y = \frac{1}{2\pi}\int_0^{2\pi} \boldsymbol{\mu}_y^2 p_{\boldsymbol{\mu}} d\beta = a^4 + 3a^2b^2 + \frac{3}{8}b^4$$

[3.25] $$I_z = \frac{1}{2\pi}\int_0^{2\pi} \mu_z^2 p_{\mu} d\beta = \frac{1}{2}a^2 \sin^2\alpha + \frac{1}{8}b^2 \sin^2\alpha$$

where $a = \cos\alpha \cdot \cos\gamma$, $b = \sin\alpha \cdot \sin\gamma$, $c = \sin\alpha \cdot \cos\gamma$, $d = \cos\alpha \cdot \sin\gamma$.

Graphs of these functions are presented in **Figure 32**.

Figure 32 ***x***,***y*** and ***z*** components of light emitted by GFP attached to the NPC. The light intensity components depend on α (the angle between the GFP excitation transition dipole and the nucleo-cytoplasmic axis of the NPC) and γ (the angle between the nucleo-cytoplasmic axis of the NPC and the electric field dipole of the exciting light).

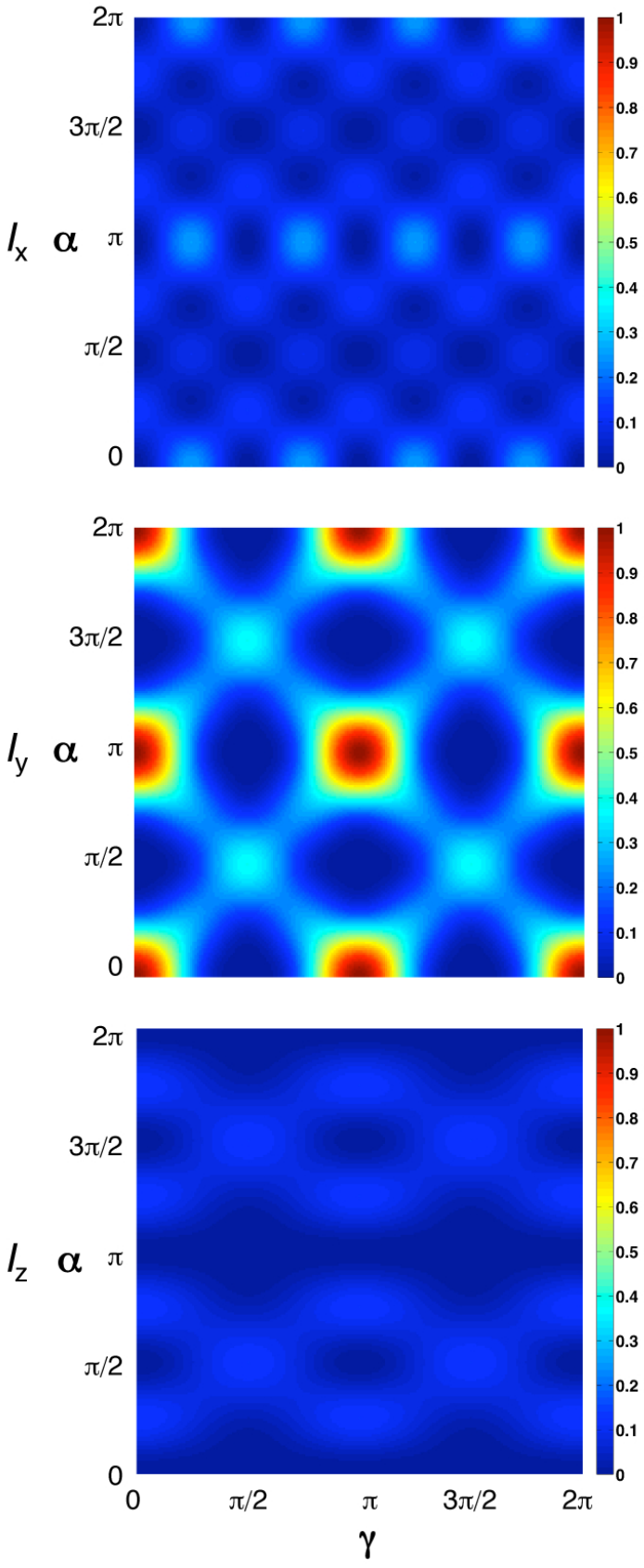

Figure 32

When measuring $I_{\parallel}$ and $I_{\perp}$ using a microscope, the intuitive assumption would be $I_{\parallel} = I_y$, $I_{\perp} = I_x$. However, light intensity components get "mixed" as they pass through the microscope. A correction for this component mixing has been derived by Axelrod (Axelrod, 1979):

[3.26] $$I_{\parallel} = K_1 I_x + K_2 I_y + K_3 I_z$$

[3.27] $$I_{\perp} = K_2 I_x + K_1 I_y + K_3 I_z$$

where

[3.28] $$K_1 = \tfrac{1}{12}(1 - 3\cos\sigma_0 + 3\cos^2\sigma_0)$$

[3.29] $$K_2 = \tfrac{1}{4}(5 - 3\cos\sigma_0 - \cos^2\sigma_0 - \cos^3\sigma_0)$$

[3.30] $$K_3 = \tfrac{1}{3}(2 - 3\cos\sigma_0 + \cos^3\sigma_0)$$

where σ_0 is the half-angle of the maximum cone of light entering the lens. σ_0 can be calculated from *NA*, the numerical aperture of the objective and *n*, the index of refraction of the medium through which the light passes, using the following relation:

[3.31] $$NA = n \sin \sigma_0$$

In the present study, we used an objective with *NA* = 1.45 and immersion oil with *n* = 1.516, yielding $\sigma_0 \approx 1.27$ (73º). Using this value for σ_0, we obtain $K_1 \approx 0.03$, $K_2 \approx 1.00$, $K_3 \approx 0.38$. Graphs of $I_{\parallel}$ and $I_{\perp}$ for these values are shown in **Figure 33**.

The corrected anisotropy distribution around the nuclear envelope cross-section for GFP with orientation α with respect to the NPC as measured by polarized microscopy is:

[3.32] $$A_\alpha(\gamma) = \frac{I_{\parallel} - I_{\perp}}{I_{\parallel} + 2 \cdot I_{\perp}} = (K_2 - K_1) \frac{I_y - I_x}{(K_1 + 2K_2) I_x + (K_2 + 2K_1) I_y + 3K_3 I_z}$$

Inserting $K_1 \approx 0.03$, $K_2 \approx 1.00$, $K_3 \approx 0.38$ into [3.32] yields:

[3.33] $$A_\alpha(\gamma) \approx \frac{I_y - I_x}{2.1 \cdot I_x + 1.1 \cdot I_y + 1.2 \cdot I_z}$$

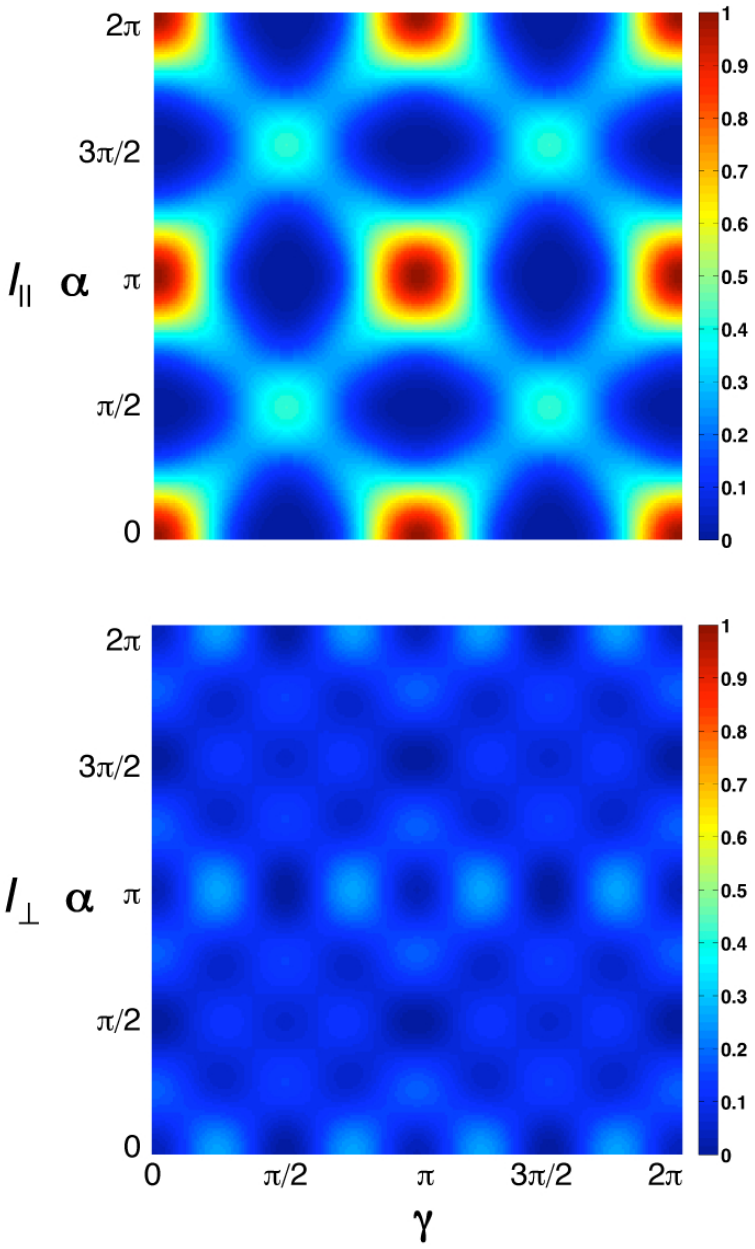

Figure 33 Predicted GFP fluorescence light intensities parallel and perpendicular to the exciting light. Numerical values were calculated for the numerical aperture and immersion oil used in this study, and are shown as a function of α (the angle between the GFP excitation transition dipole and the

nucleo-cytoplasmic axis of the NPC) and γ (the angle between the nucleo-cytoplasmic axis of the NPC and the electric field dipole of the exciting light).

This family of functions $A_\alpha(\gamma)$ can be written explicitly by substitution with equations [3.23-3.25]; it is graphed in **Figure 34**a.

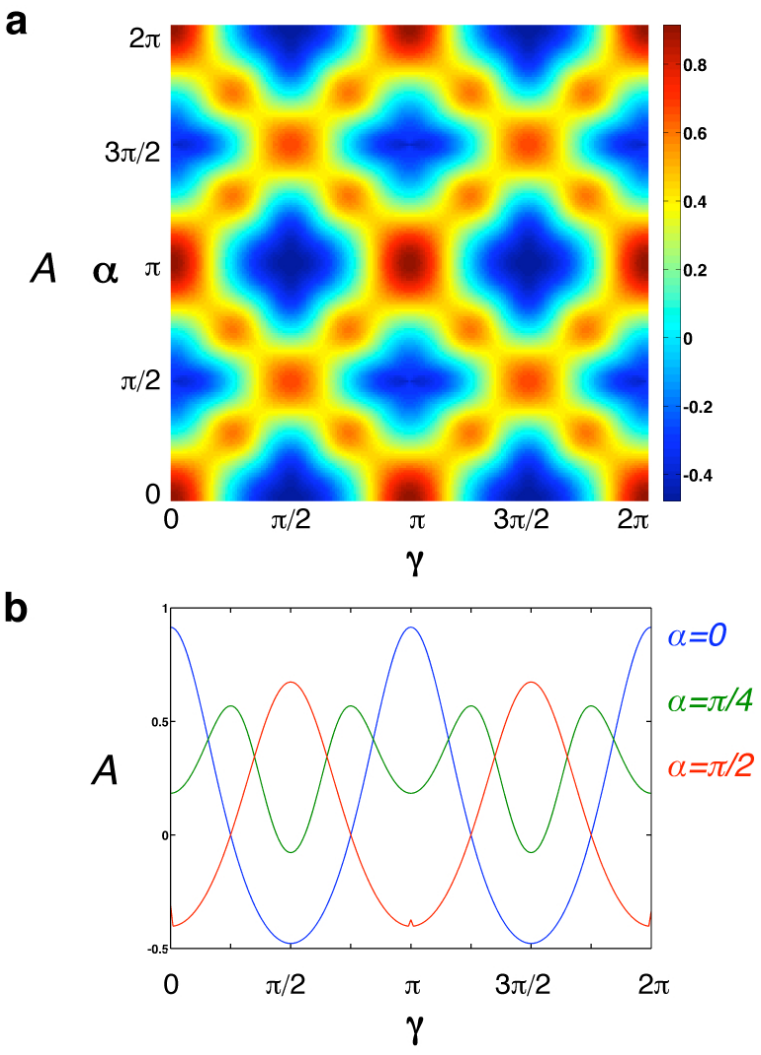

Figure 34 Fluorescence anisotropy as a function of α (the angle between the GFP excitation transition dipole and the nucleo-cytoplasmic axis of the NPC) and γ (the angle between the nucleo-cytoplasmic axis of the NPC and the electric field dipole of the exciting light). Numerical values were

calculated for the numerical aperture and immersion oil used in this study. (**a**) Graph for all values of α and γ. (**b**) Graph for three selected values of α: 0, π/4 and π/2.

Although the graph of $A_\alpha(\gamma)$ has similarities with $f_\alpha(\gamma)$, there are interesting differences. Extrema $A_\alpha(\gamma)$ are found at $\gamma = 0$ and $\gamma = \pi/2$ for any choice of parameter α. Whether these extrema are maxima or minima depends on K_1, K_2, K_3 and α. Importantly, further extrema can be present, thus $A_\alpha(\gamma = 0)$ and $A_\alpha(\gamma = \frac{\pi}{2})$ do not always represent the global maximum and minimum of the anisotropy. For illustrative purposes, we will consider three cases of $A_\alpha(\gamma)$, shown in **Figure 34**b for $K_1 \approx 0.03$, $K_2 \approx 1.00$, $K_3 \approx 0.38$. The general characteristics of these functions are outlined below and also apply to other values K_1, K_2, K_3, as long as $K_2 > K_1$.

(i) $\alpha=\alpha_1$, all GFP dipoles parallel to the nucleo-cytoplasmic axis

When the GFP transition dipoles are parallel to the nucleo-cytoplasmic axis ($\alpha = \alpha_1 = 0$), the anisotropy is maximal for NPCs with their nucleo-cytoplasmic axis parallel to the direction of the polarized light ($\gamma = 0$). In NPCs at a 45° angle along the nuclear envelope cross-section ($\gamma = \pi/4$), the measured $I_{\parallel}$ and $I_{\perp}$ are equal, therefore the anisotropy becomes 0. For

NPCs oriented between 45° and 90° ($\pi/4 < \gamma < \pi/2$), $I_{\perp}$ is greater than $I_{\parallel}$, resulting in negative anisotropy values. Note that the anisotropy is not defined for $\gamma = \pi/2$, since GFP is not excited in NPCs in this orientation.

(ii) $\alpha=\alpha_2$, GFP dipoles parallel to the nuclear envelope

When the GFP transition dipoles are parallel to the nucleo-cytoplasmic axis ($\alpha = \alpha_2 = \pi/2$), the anisotropy is maximal for NPCs with their nucleo-cytoplasmic axis perpendicular to the direction of the polarized light ($\gamma = \pi/2$). As γ decreases from $\pi/2$ towards 0, the anisotropy decreases. In NPCs at a 45° angle along the nuclear envelope cross-section ($\gamma = \pi/4$), the measured $I_{\parallel}$ and $I_{\perp}$ are equal, therefore the anisotropy becomes 0. The anisotropy is not defined for $\gamma = 0$, where GFP is not excited.

(iii) $\alpha=\pi/4$

When the GFP transition dipoles are at a 45° angle from the nucleo-cytoplasmic axis ($\alpha = \pi/4 + n\cdot\pi$), the anisotropy reaches a global minimum at $\gamma = \pi/2$ and a local minimum at $\gamma = 0$. The maximum anisotropy is obtained for γ close to $\pi/4$.

As these examples illustrate, the pattern of GFP anisotropy around the nuclear envelope cross-section, both in terms of the localization of maxima and minima, and in terms of the relative values of these extrema, is a function of α. The dramatic changes in the anisotropy pattern as a function of α should allow us to estimate α by measuring $A(\gamma)$ experimentally, even in the presence of noise.

Effects of homo-FRET between GFP-tagged nups within the NPC on fluorescence anisotropy: Theory

As described in Chapter 1, the efficiency of homo-FRET between two fluorophores depends on their distance and mutual orientation. When investigating homo-FRET for molecules in solution, one assumes random orientations between the fluorophores to calculate the homo-FRET efficiency and the loss of anisotropy resulting from homo-FRET. This assumption is not valid for fluorophores that are ordered with respect to the NPC. In the following sections, I will derive upper bounds for the effect on anisotropy that results from homo-FRET between ordered GFP-tagged nups and show that the effects are negligible for nups occurring in eight or sixteen copies. For nups occurring in more than sixteen copies, and for GFP attached to disordered nup domains, homo-FRET can have substantial

effects on anisotropy. These depend on the labeling density, which can easily be controlled in genomically tagged yeast cells, as discussed below.

(i) GFP attached to ordered domains of nups present in eight copies within the NPC

Due to the eightfold symmetry axis of the NPC, nups occurring in eight copies per NPC will always form an octagon parallel to the nuclear envelope plane (**Figure 35**). If r is the distance between the nups and the nucleocytoplasmic axis $\boldsymbol{N}$, then we can place one GFP on the $\boldsymbol{P}$ axis, where it will have the following coordinates m_1 and dipole vector $\boldsymbol{\mu}_1$:

[3.34] $$m_1 = (0, r, 0) \;;\; \boldsymbol{\mu}_1 = \begin{pmatrix} \cos\alpha \\ \sin\alpha \cdot \cos\beta \\ \sin\alpha \cdot \sin\beta \end{pmatrix}$$

An adjacent GFP will have the coordinates m_2 and dipole vector $\boldsymbol{\mu}_2$:

[3.35] $$m_2 = \left(0, \tfrac{1}{\sqrt{2}} r, \tfrac{1}{\sqrt{2}} r\right) \;;\; \boldsymbol{\mu}_2 = \begin{pmatrix} \cos\alpha \\ \sin\alpha \cdot \cos(\beta + \tfrac{\pi}{4}) \\ \sin\alpha \cdot \sin(\beta + \tfrac{\pi}{4}) \end{pmatrix}$$

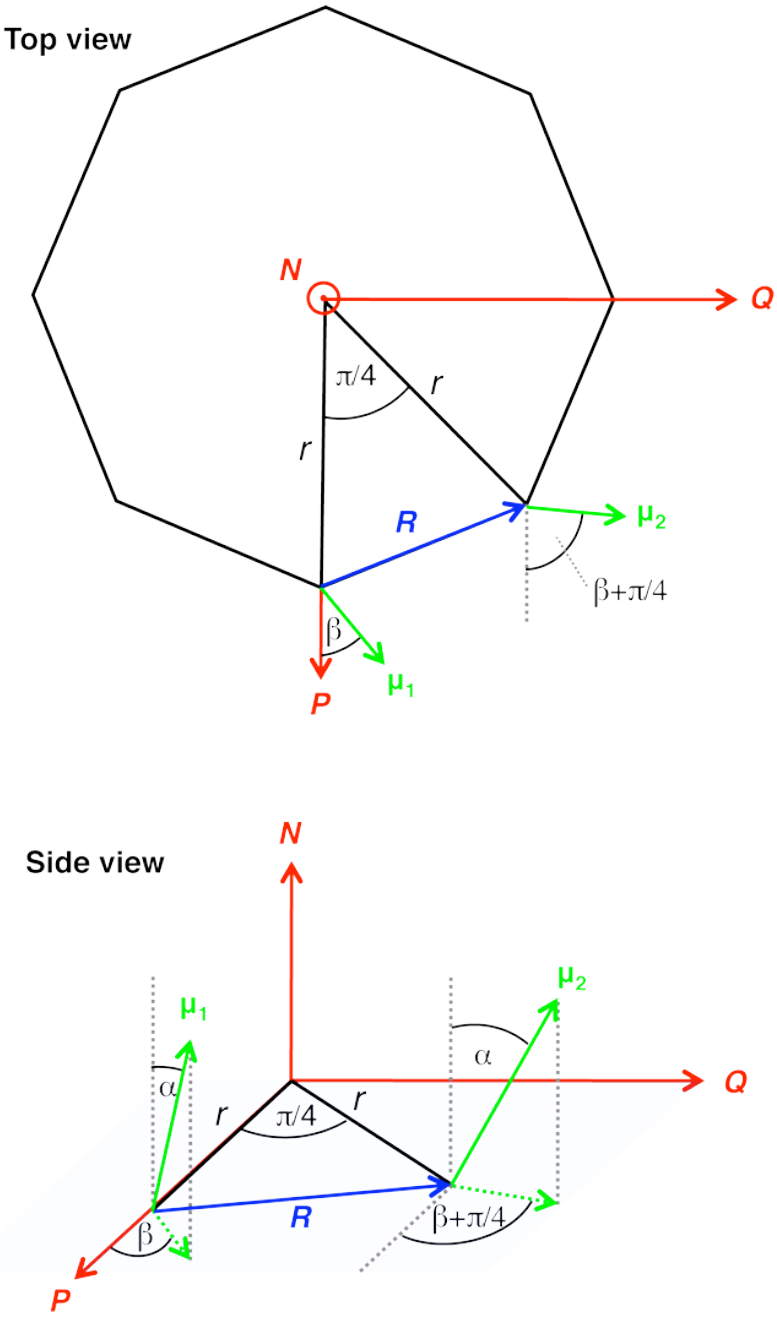

Figure 35 Geometry of two GFP molecules attached rigidly to two adjacent nups localized in the same plane parallel to the nuclear envelope. Details are given in the text.

The vector $\boldsymbol{R}$ between them is:

[3.36] $$\boldsymbol{R} = m_2 - m_1 = \begin{pmatrix} 0 \\ \frac{1-\sqrt{2}}{\sqrt{2}} r \\ \frac{1}{\sqrt{2}} r \end{pmatrix}$$

and the length of R is:

[3.37] $$|\boldsymbol{R}| = \sqrt{2-\sqrt{2}} \cdot r$$

The cosines of the angles between $\boldsymbol{\mu}_1$, $\boldsymbol{\mu}_2$ and $\boldsymbol{R}$, as defined in Chapter 1, can be calculated as follows:

[3.38] $$\cos\theta = \boldsymbol{\mu}_1 \cdot \boldsymbol{\mu}_2 = \cos^2\alpha + \tfrac{1}{\sqrt{2}}\sin^2\alpha$$

[3.39] $$\cos\phi = \frac{\boldsymbol{\mu}_1 \cdot \boldsymbol{R}}{|\boldsymbol{R}|} = \tfrac{1}{2\sqrt{2-\sqrt{2}}}\sin\alpha \cdot [\sqrt{2}\sin\beta + (\sqrt{2}-2)\cos\beta]$$

[3.40] $$\cos\psi = \frac{\boldsymbol{\mu}_2 \cdot \boldsymbol{R}}{|\boldsymbol{R}|} = \tfrac{1}{2\sqrt{2-\sqrt{2}}}\sin\alpha \cdot [\sqrt{2}\sin\beta - (\sqrt{2}-2)\cos\beta]$$

Thus, the orientation factor κ^2 can be calculated explicitly:

$$\kappa^2 = (\cos\theta - 3\cdot\cos\theta\cdot\cos\psi)^2 = \frac{[(2\sqrt{2}-4)\cos^2\alpha + (\sqrt{2}-1+3(\sqrt{2}-2)\cos^2\beta)\sin^2\alpha]^2}{24-16\sqrt{2}} \quad [3.41]$$

Note that κ^2 depends only on α and β, not on r.

The Förster distance for homo-FRET between randomly oriented GFP molecules (κ^2 = 2/3) is 47 Å (Gautier et al., 2001). We can calculate the Förster distance R_0 for other values of κ^2 as follows:

$$R_0 = \sqrt[6]{\frac{3\kappa^2}{2}}\cdot 47\text{Å} \quad [3.42]$$

The homo-FRET efficiency E is then:

$$E = \frac{1}{1+\frac{2}{3\kappa^2}\left(\frac{|\boldsymbol{R}|}{47\text{Å}}\right)^6} \quad [3.43]$$

and E is a function of r, α and β. For any given set of dipole orientations α and β, E will increase as r (and thus the distance $|\boldsymbol{R}|$ between the GFP molecules) decreases. The smallest possible value of r for ordered nup domains is 200 Å, since the central channel of the yeast NPC has a diameter of ~40 nm (Yang et al., 1998). Values of E for r = 200 Å will thus represent an upper limit for homo-FRET between GFP attached to ordered nups present in eight copies per NPC. **Figure 36** shows E as a function of α and β for r = 200 Å. Even for optimal choices of α and β, the homo-FRET efficiency is well below 0.1%, and thus negligible.

(ii) GFP attached to ordered domains of nups present in sixteen copies within the NPC

For nups present in sixteen copies, the nearest neighbor for a given nup can be a nup related by symmetry around a dyad axis that lies within the nuclear envelope mid-plane. To describe the spatial relationship between GFPs attached to these two nups, we need two further parameters: h, the distance from the nuclear envelope mid-plane and δ, the angle between the dyad axis and the shortest line connecting GFP and the nucleocytoplasmic axis $\boldsymbol{N}$ (**Figure 37**).

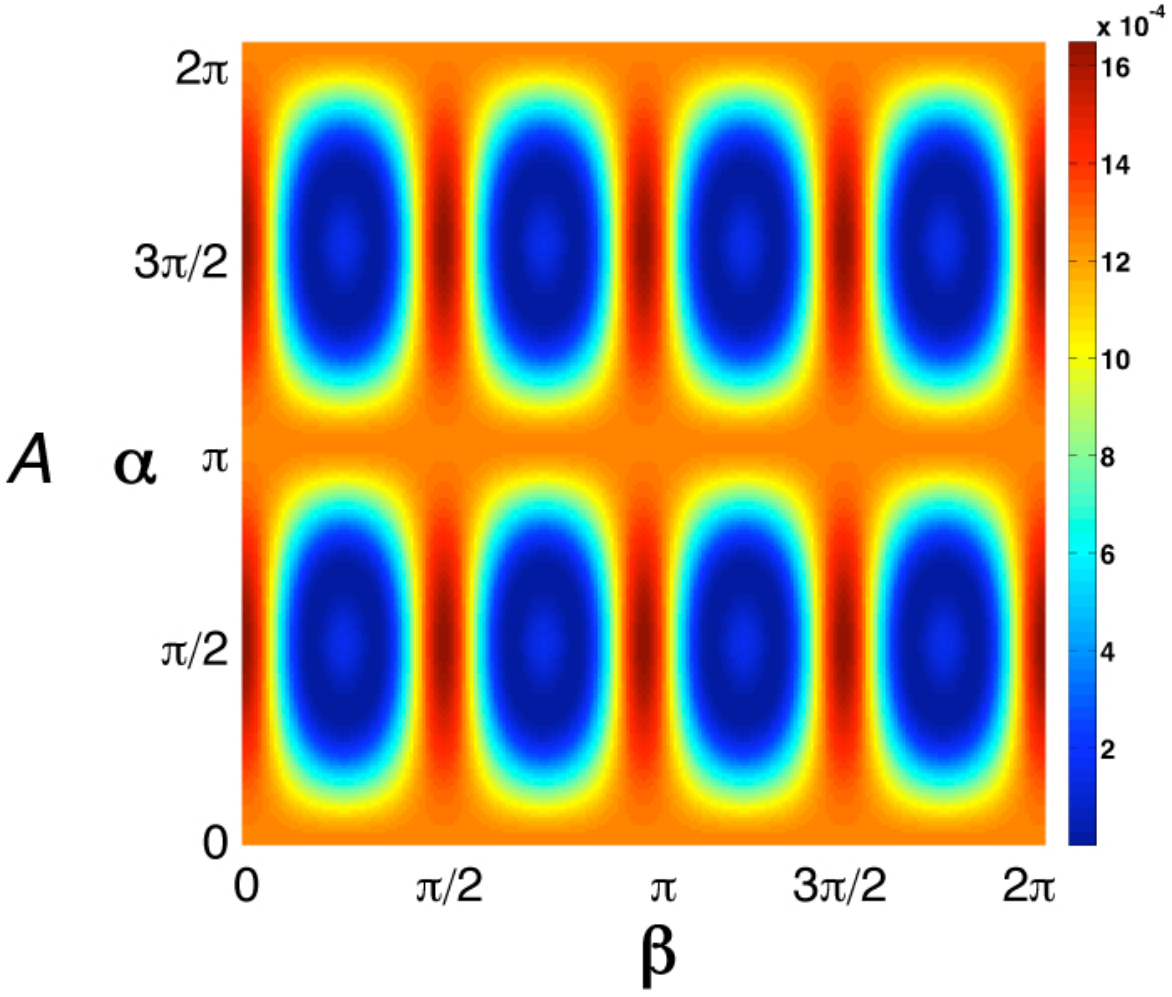

Figure 36 Homo-FRET efficiency *E* between GFP molecules rigidly attached to nups present in eight copies per NPC, as a function of α and β.

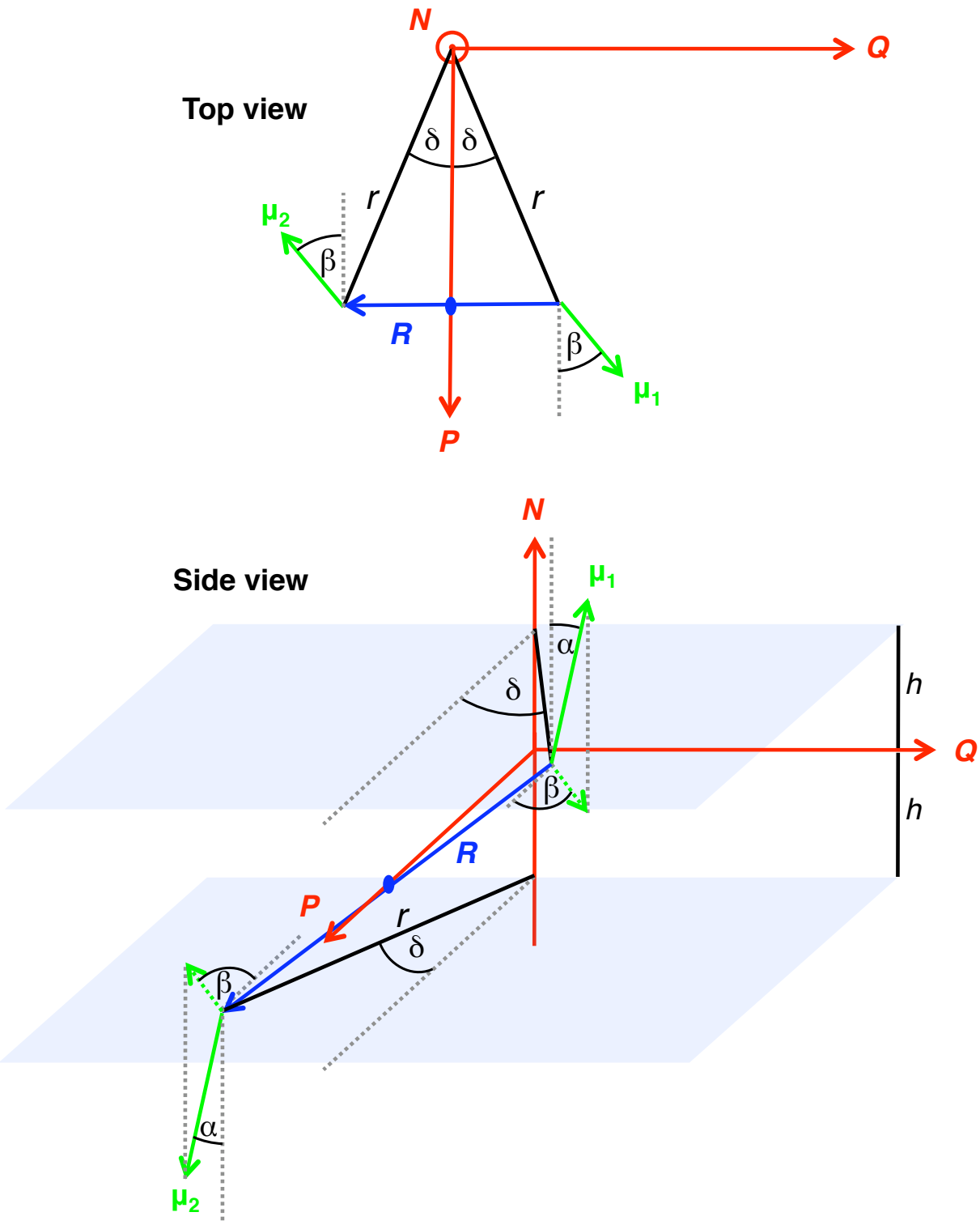

Figure 37 Geometry of two GFP molecules attached rigidly to two nups related by dyad symmetry. Details are given in the text.

δ is between 0 and $\pi/16$, since for greater values of δ, a different GFP becomes the nearest neighbor. To simplify calculations, we choose the dyad axis to coincide with the ***P*** axis of the coordinate system.

The coordinates m_1, m_2 and the dipole vectors $\boldsymbol{\mu}_1, \boldsymbol{\mu}_2$ of the GFP molecules are:

[3.44] $$m_1 = (h, r\cos\delta, r\sin\delta) \;;\; \boldsymbol{\mu}_1 = \begin{pmatrix} \cos\alpha \\ \sin\alpha\cdot\cos\beta \\ \sin\alpha\cdot\sin\beta \end{pmatrix}$$

[3.45]

$$m_2 = (-h, r\cos\delta, -r\sin\delta) \;;\; \boldsymbol{\mu}_2 = \begin{pmatrix} \cos\alpha \\ \cos(2\delta)\cdot\sin\alpha\cdot\cos\beta + \sin(2\delta)\cdot\sin\alpha\cdot\sin\beta \\ \cos(2\delta)\cdot\sin\alpha\cdot\sin\beta - \sin(2\delta)\cdot\sin\alpha\cdot\cos\beta \end{pmatrix}$$

Vector ***R*** connecting the GFPs, and its length |***R***| are:

[3.46] $$\boldsymbol{R} = \begin{pmatrix} -2h \\ 0 \\ -2r\sin\delta \end{pmatrix} \;;\; |\boldsymbol{R}| = 2\sqrt{h^2 + r^2\sin^2\delta}$$

The cosines of the angles between $\boldsymbol{\mu}_1, \boldsymbol{\mu}_2$ and ***R*** can be used to calculate κ^2, as in the previous section. The resulting expression is cumbersome and therefore not given here. κ^2 depends on α, β, δ, h and r.

The efficiency of homo-FRET can become very high when $|\boldsymbol{R}|$, the distance between the GFP molecules, is short. This is the case whenever h and δ are small, irrespective of r. However, our ability to monitor homo-FRET relies on a loss of anisotropy occurring when a photon absorbed by a GFP in one orientation is transferred to, and emitted by a GFP in a different orientation. For small δ, where homo-FRET can occur efficiently, the dipoles of the GFP molecules are also very similar, thus leading to a small effect on the anisotropy – in the limit of $\delta=0$, $\boldsymbol{\mu}_1 = \boldsymbol{\mu}_2$ and we cannot detect the homo-FRET event. The question is therefore whether there are values of δ for which homo-FRET occurs between GFP molecules that are different enough in their orientation to result in detectable FRET.

When homo-FRET occurs between two GFP molecules rigidly positioned with respect to each other, the probability of transfer back to the original donor GFP cannot be excluded. The probability of photon emission from the GFP that was originally excited is:

$$[3.47]\ (E-1) + E \cdot E \cdot (E-1) + E \cdot E \cdot E \cdot E \cdot (E-1) + \ldots = \sum_{n=0}^{\infty} E^{2n}(E-1)$$

and the probability of photon emission from the adjacent GFP is

[3.48] $$E \cdot (E-1) + E \cdot E \cdot E \cdot (E-1) + \ldots = E \cdot \sum_{n=0}^{\infty} E^{2n}(E-1)$$

Thus, the overall efficiency with which the photon will be emitted from the adjacent GFP, which I will designate E_∞, is:

[3.49] $$E_\infty = \frac{E \cdot \sum_{n=0}^{\infty} E^{2n}(E-1)}{E \cdot \sum_{n=0}^{\infty} E^{2n}(E-1) + \sum_{n=0}^{\infty} E^{2n}(E-1)} = \frac{E}{E+1}$$

For maximally efficient homo-FRET, $E_\infty = ½$.

When the effects of homo-FRET are taken into account, equations [3.23-25] become:

[3.50] $$I_x^{FRET} = \frac{1}{2\pi} \int_0^{2\pi} p_{\boldsymbol{\mu}_1} \cdot (1 - E_\infty) \cdot \boldsymbol{\mu}_{1x}^2 d\beta + \frac{1}{2\pi} \int_0^{2\pi} p_{\boldsymbol{\mu}_1} \cdot E_\infty \cdot \boldsymbol{\mu}_{2x}^2 d\beta$$

and *mutatis mutandis* for I_y and I_z. These FRET-corrected intensity components would be used to calculate the FRET-corrected anisotropy A^{FRET}. In order to summarize the anisotropy changes caused by homo-FRET,

one could calculate the root mean square deviation between A^{FRET} and the FRET-less anisotropy A along the nuclear envelope cross-section:

$$[3.51] \qquad RMSD^{FRET}(\alpha,\delta,r,h) = \sqrt{\frac{1}{2\pi}\int_0^{2\pi}(A^{FRET} - A)^2\, d\gamma}$$

In practice, already the integral in equation [3.50] is too complicated to solve analytically, even with the help of computer programs like Mathematica, since p, E_∞ and μ all depend on β. Instead, I will estimate an upper limit for the anisotropy change caused by homo-FRET.

To eliminate the dependence of E_∞ on β, we set κ^2 to its theoretical maximum value of 4. Furthermore, to minimize $|\boldsymbol{R}|$, we will set r to 200 Å, the smallest value for ordered nups as outlined above, and we will set h to 20 Å, corresponding roughly to the radius of GFP itself. The resulting value of E_∞ is:

$$[3.52] \qquad E_{\infty,\max} = \frac{1}{2 + \frac{32}{3\cdot 47^6}\left(400 + 40{,}000\cdot \sin^2\delta\right)^3}$$

The integral in equation [3.50] can now be solved, and A^{FRET} can be calculated. However, the integral in [3.51] is again too complicated. Therefore, we are not able to investigate the $RMSD^{FRET}$ for all α, γ and δ. Instead, we will first inspect the change in anisotropy caused by homo-FRET, $A^{FRET}(\gamma,\delta)-A(\gamma)$ for three specific values of α: 0, $\pi/4$, and $\pi/2$. For $\alpha=0$, the calculated change in anisotropy was close to 0 for all values of α and δ. The other two cases are shown in **Figure 38**. Since the largest effect was apparent around $\delta=3\pi/64$, I calculated $A^{FRET}(\alpha,\gamma)-A(\alpha,\gamma)$ for this value of δ (**Figure 39**). The largest calculated effect on anisotropy was a decrease by ~0.01 (for $\alpha=\pi/2$, $\gamma=\pi/2$, $\delta=3\pi/64$). A change in anisotropy on this order of magnitude is small but detectable. However, most parameter choices of α, δ, h and r will result in much smaller homo-FRET effects. In general, homo-FRET between GFPs labeling ordered domains of nups present in 16 copies per NPC is therefore not likely to be an important factor in fluorescence anisotropy measurements.

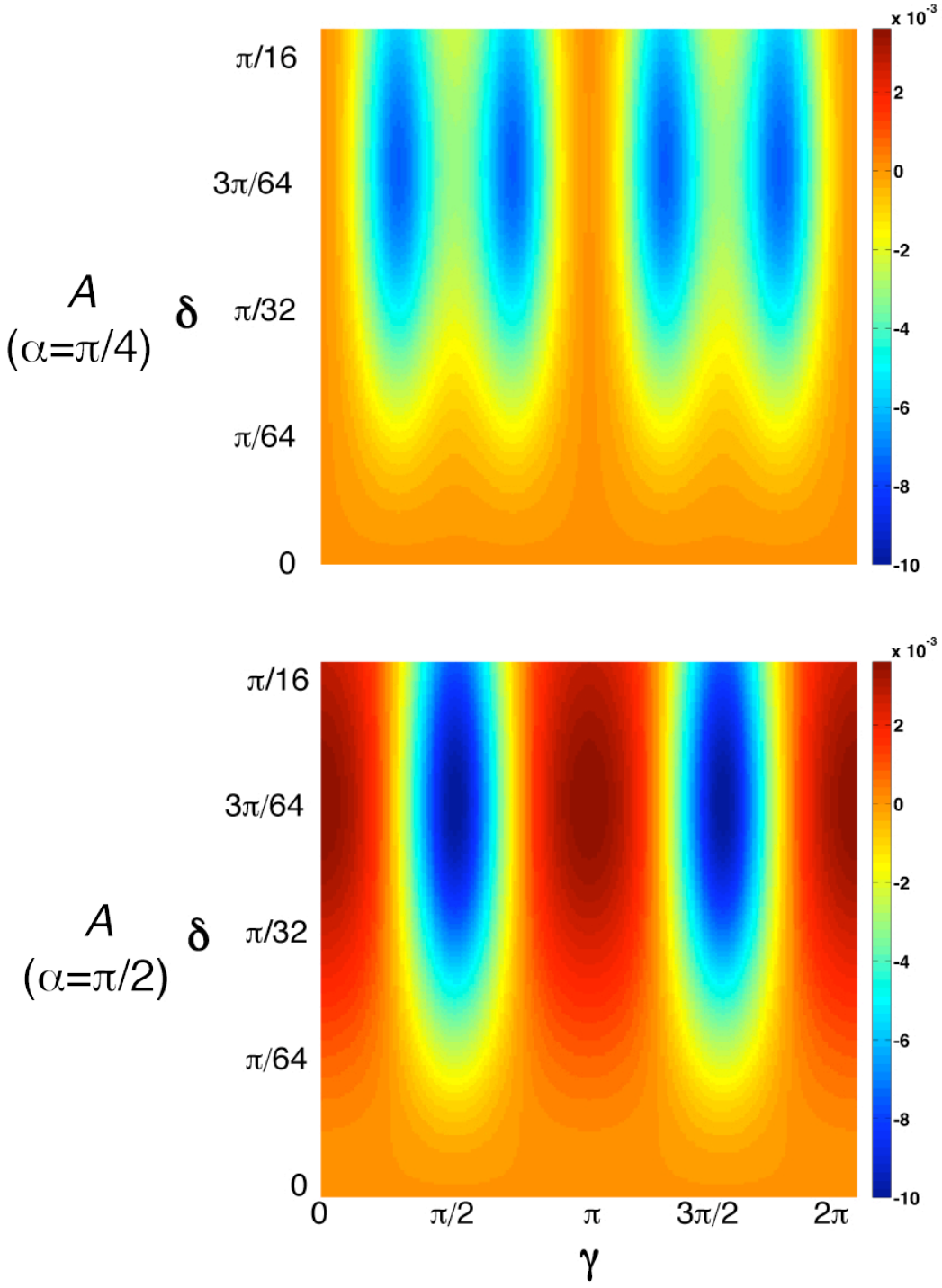

Figure 38 Upper limit of effects of homo-FRET on anisotropy for $\alpha=\pi/4$ and $\alpha=\pi/2$. For $\alpha=0$, no changes were detectable. Maximal changes in anisotropy are observed for a value of δ around $3\pi/64$.

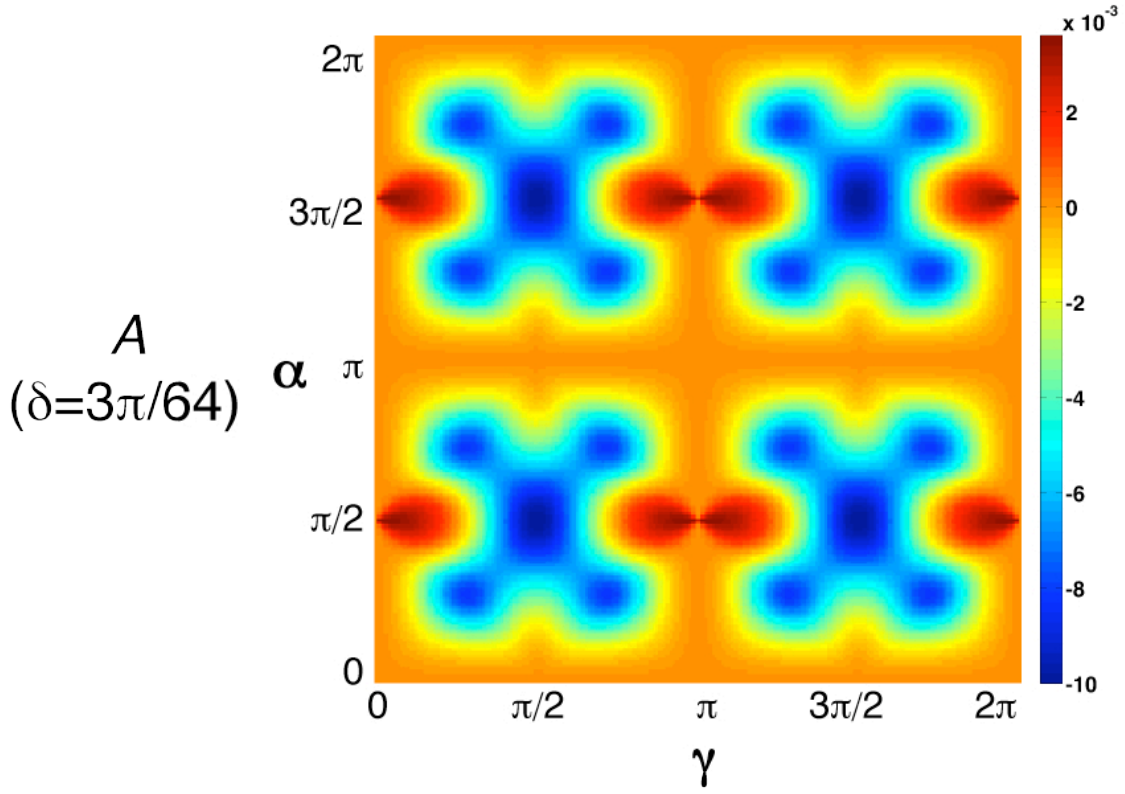

Figure 39 Upper limit of effects of homo-FRET on anisotropy for δ=3π/64.

(iii) GFP attached to ordered domains of nups present in thirty-two copies within the NPC

The core NPC consists of 16 asymmetric units. Nups present in 32 copies per NPC will therefore be present in two copies per asymmetric unit. Within an asymmetric unit, there are no symmetry constraints; hence it is possible that the two nups present in the same asymmetric unit are positioned close to

each other for efficient homo-FRET and at angles that lead to significant losses in anisotropy upon homo-FRET. We predict that in the case of 32 GFP-labeled nups, each nup has exactly one potential homo-FRET partner, since homo-FRET between proteins located in different asymmetric units is not efficient or does not have a large effect on anisotropy, as shown above. However, since the orientation and distance for homo-FRET pairs are arbitrary, it is not possible to predict the exact effect of homo-FRET on anisotropy around the nuclear envelope cross-section.

An experimental approach that we developed in order to test for homo-FRET between GFP-labeled nups is to control the GFP-labeling stoichiometry of a given nup. In budding yeast, genomic tagging in haploid strains will lead to a stoichiometry of one GFP tag per nup. The same stoichiometry is obtained in diploid strains in which both alleles of the nup are genomically tagged with GFP. However, diploid strains in which only one of the two nup alleles is tagged with GFP will have a labeling ratio of 0.5. A caveat is that the efficiency of gene expression may be affected by GFP tagging and distort the ratio of labeled versus unlabeled nup. Furthermore, mRNA production in bursts can lead to stochastic fluctuations in the ratio of labeled and unlabeled nups over time. Thus, when an NPC is

assembled in the presence of an excess of GFP-tagged nup over untagged nup, its GFP labeling ratio will be larger than 0.5, and vice versa.

However, if we assume that on average, the GFP-labeling ratio in a single-labeled diploid will be 0.5, then there is a 50% chance for each GFP-nup that a homo-FRET partner is present in the asymmetric unit. The lower labeling ratio will thus reduce the amount of homo-FRET occurring by half, and be reflected in a gain in anisotropy. Since the labeling ratio should generally not affect the orientation of labeled nups within the NPC, or the rotational diffusion of labeled nups, a difference in GFP anisotropy between fully and half-labeled strains is indicative of homo-FRET.

(iv) GFP attached flexibly to nup domains.

In this section, we will consider GFP molecules that do not show a fixed orientation with respect to the NPC, and therefore exhibit a uniform anisotropy value along the nuclear envelope cross-section. If GFP rotational diffusion is negligible, this anisotropy value will be ~0.4 in the absence of homo-FRET. The orientation factor κ^2 between any two disordered GFP molecules will on average be 2/3, thus the Förster distance R_0 will be 47 Å. Homo-FRET efficiency should thus solely depend on the distance $|\boldsymbol{R}|$ between GFP molecules (equation [1.13], from chapter 1.). The anisotropy

of randomly oriented acceptor molecules is 0 on average. Since anisotropy values of different coexisting species (in this case, primary excited fluorophores, with an anisotropy of ~0.4, and acceptor molecules, with an anisotropy of 0) are additive, the expected anisotropy is:

[3.53] $$A = (1 - E_\infty) \cdot 0.4 + E_\infty \cdot 0 = (1 - E_\infty) \cdot 0.4$$

We can distinguish two types of unoriented GFP tags: those that are localized at defined positions within the NPC since they are attached to nups via a short flexible linker, and those that are attached to nups via a long, unstructured FG domain and thus neither orientationally nor spatially fixed with respect to the NPC.

For spatially fixed GFP molecules attached to nups present in eight copies per NPC, $|\boldsymbol{R}|$ can be calculated directly from their distance r to the nucleo-cytoplasmic axis, using equation [3.37]. For the minimal distance of r = 200 Å for ordered nups, we obtain $|\boldsymbol{R}| \approx 153$Å, which translates to a negligible FRET efficiency of 0.8%. However, randomly oriented nups present in more than eight copies can be present in pairs with short distances between them, resulting in efficient homo-FRET.

GFP tags attached to unstructured FG domains of nups are not localized to a defined position within the NPC. Rather, they will assume a position within a radius ρ of the structured domain of the nup. Results obtained *in vitro* suggest that FG domains can be described by the Kradky-Porod model as worm-like chains with a persistence length l_p of 3.9 Å and a contour length L_c corresponding to the number of amino acids multiplied with the average peptide bond length of 3.8 Å (Lim et al., 2006). Thus, the average ρ will be

[3.54] $$\bar{\rho} = \sqrt{2 \cdot l_p \cdot L_c} \approx \sqrt{30 \cdot aa}\,\text{Å}$$

where *aa* is the number of amino acids constituting the FG domain. In the context of the NPC, the density of FG domains is so high that the ends of FG domains are likely "pushed" further away from their anchoring point in the structured part of the NPC (Lim et al., 2006). Thus, it is probably a fair assumption that GFP molecules attached to the end of FG domains of central nups are randomly distributed within the central channel, and possibly the volume surrounding it. If we describe the central channel as a cylinder with height 30 nm and a radius of 20 nm, the local concentration of *n* GFP molecules would be:

[3.55] $$n \cdot [nup]_{central\ channel} = \frac{n / N_A}{\pi \cdot 20^2 \cdot 30\ \text{nm}^3} \approx n \cdot 44\mu\text{M}$$

which corresponds to ~0.7 mM for nups occurring in 16 copies and ~1.4 mM for nups present in 32 copies. If we assume that the FG domains extend beyond the central channel towards the cytoplasm and nucleoplasm, the local GFP concentration would be even lower.

The critical concentration C_0 at which the homo-FRET efficiency is 50% can be calculated from R_0 as follows (Förster, 1948):

[3.56] $$C_0 = \frac{3}{4\pi \cdot N_A \cdot R_0^3} = \frac{3}{4\pi \cdot N_A \cdot (47\text{Å})^3} \approx 3.8\text{mM}$$

Different equations have been derived to calculate the homo-FRET efficiencies E for concentrations below C_0 (Förster, 1948; Ore, 1959). According to these equations, the range of E predicted for 16 GFP molecules (0.7 mM) or 32 GFP molecules (1.4 mM) is between 20% and 30%, thus homo-FRET between GFP attached to FG domains could decrease the anisotropy from 0.4 to ~0.3-0.33. Decreasing the GFP labeling ratio from 1

to 0.5 amounts to halving the GFP concentration, which will reduce the homo-FRET efficiency.

To summarize this section, GFP labeling of one species of nup within the NPC can lead to a loss in anisotropy by homo-FRET, but only for GFP-tags that are flexibly attached to nups, or for GFP-tags that are rigidly attached to nups present in more than 16 copies per NPC. In particular, homo-FRET will not occur between GFPs localized to the structured domains of nups related by eightfold symmetry around the nucleo-cytoplasmic axis. This precludes their use in monitoring radial dilation of the transporting NPC. However, such measurements could be achieved by labeling more than one nup species with GFP, or by labeling two nup species with different spectral variants of GFP and quantifying hetero-FRET between them.

To distinguish anisotropy loss due to homo-FRET from anisotropy loss caused by other processes, cells with a reduced GFP labeling ratio can be investigated, since GFP density should affect homo-FRET, but not other processes affecting fluorescence anisotropy.

Effects of dynamics of GFP-tagged nups within the NPC on fluorescence anisotropy: Theory

As outlined in Chapter 1, loss in fluorescence anisotropy can occur when the fluorophore changes its orientation on the time-scale of the fluorescence life time. Using equation [1.7], we can estimate the magnitude of this effect for GFP. The molecular weight of GFP is ~27 kDa, its τ_c in aqueous solution at 20ºC estimated from equation [1.9] is ~11 ns. The fluorescence lifetime τ_F of GFP is ~3 ns (Suhling et al., 2002; Volkmer et al., 2000). According to the Perrin equation, the measured anisotropy A for GFP in solution should therefore be $A_0 \cdot (1/(1 + 3 \text{ ns}/11 \text{ ns})) \approx 0.8 \cdot A_0 = 0.8 \text{ x } 0.4 = 0.32$. This is indeed the experimentally determined value for free GFP in solutions as well as in the cytosol of eukaryotic cells (Rocheleau et al., 2003). Thus, the difference in anisotropy we can expect between rapidly diffusing and spatially fixed unoriented GFP tags within the NPC is at most ~25%. In particular, very accurate measurements will be required to distinguish between the hydrophobic meshwork and the entropic exclusion model for FG repeats.

Rotational diffusion can also lower anisotropy values for GFP tags that appear to have a somewhat defined orientation within the NPC based on their anisotropy variation around the nuclear envelope cross-

section. This situation would apply to GFP tags that rotate around a defined axis that is close to but not coincident with the GFP dipole axis.

Computational Processing of Polarization Microscopy Images

To measure the anisotropy of GFP-tagged nups *in vivo*, yeast cells were subjected to polarized fluorescence microsopy (technical details are described in Chapter 5). The exciting light was passed through a polarizer with known orientation. The emitted light was passed through a polarizer/image splitter, so that separate images corresponding to the light intensity parallel and perpendicular to the direction of the exciting light could be recorded simultaneously with a CCD camera (**Figure 40**).

To calculate the pixel-by-pixel anisotropy, the parallel and perpendicular channel images needed to be aligned. We found that the accuracy of alignment was a crucial factor for the calculation of anisotropy values: Since the nuclear envelope signal in the images was only a few pixels wide, slight misalignment of the channels resulted in pairing of nuclear envelope pixels from one channel with background pixels from the other channel, and the anisotropy values calculated from these mispaired pixels were meaningless.

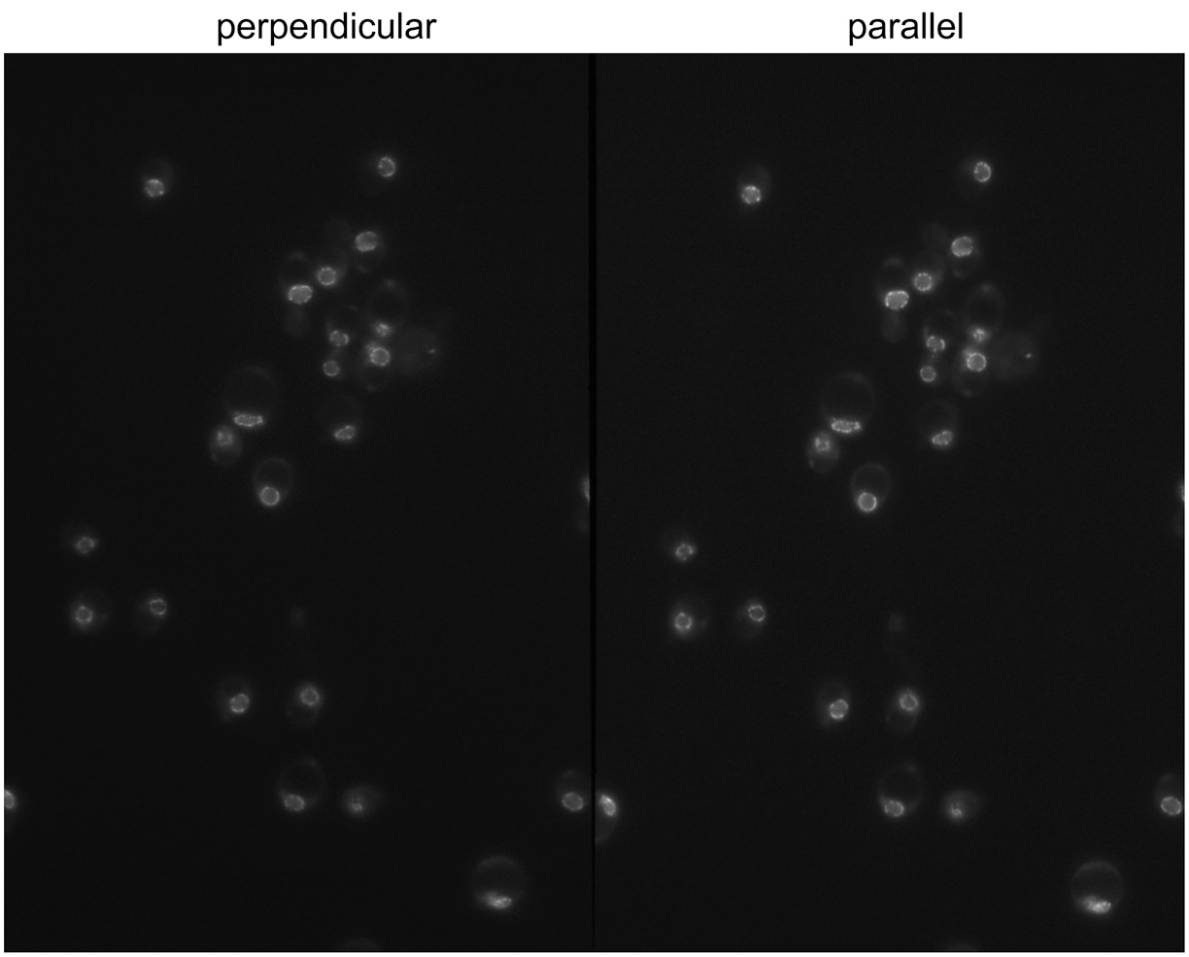

Figure 40 CCD-recorded GFP polarized epifluorescence micrograph. The image was split by a polarizer/splitter into the emitted light components parallel and perpendicular to the direction of the exciting light. Specimen: Yeast cells with GFP-labeled nups.

We first attempted to align the two half-images globally using an ImageJ script; however, the results were not satisfactory (**Figure 41**a). Possible reasons include the fact that only whole-pixel shifts were considered by ImageJ, and that distortions in the imaging of the two

channels may thwart global alignment. We therefore implemented scripts in MATLAB and SPIDER that were based on the single-particle EM approach for image alignment: Image pairs of corresponding individual cells were cropped from both channel images and aligned using rotational and translational sub-pixel alignment. This approach gave generally good results (**Figure 41**a).

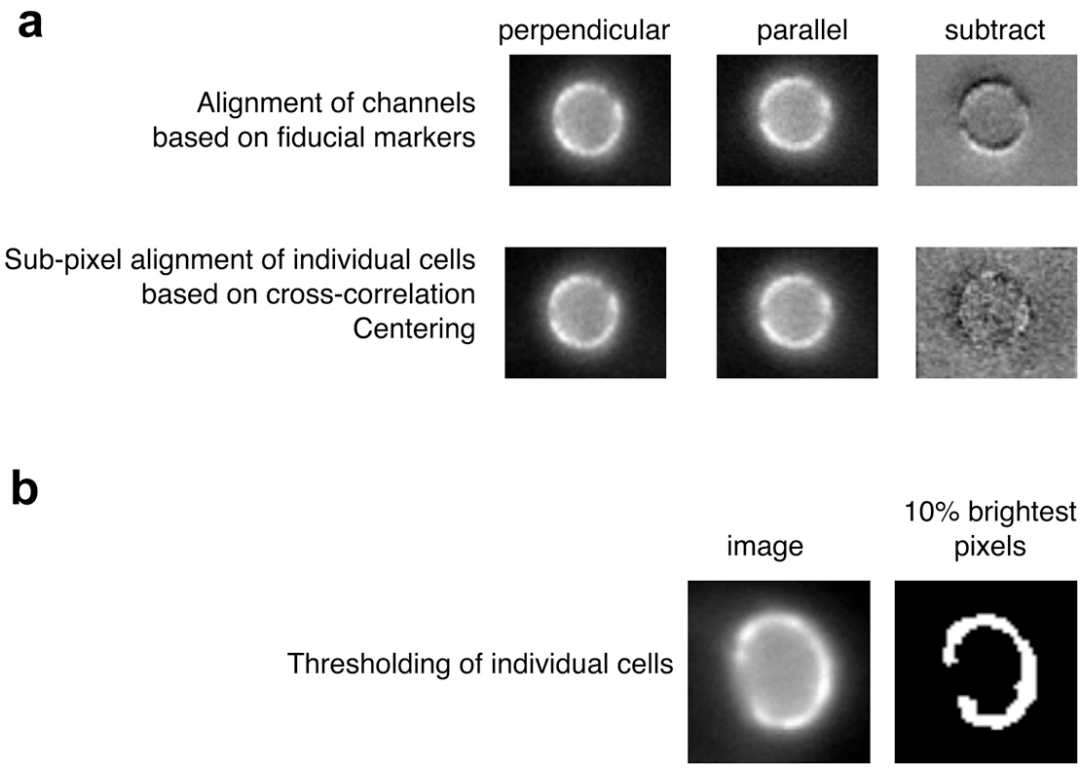

Figure 41 Computational image alignment and thresholding. (a) Alignment of the parallel and perpendicular channel images. Global alignment does not result in accurate alignment of individual nuclear envelopes. We therefore implemented sub-pixel alignment of individual images. (b) Thresholding of individual nuclear envelope images. The top 10% brightest pixels usually coincide with the nuclear envelope signal.

To include only pixels corresponding to nuclear envelope signal in our further analysis, we applied a threshold-based mask to the images. The cell-based approach proved to be crucial for this step as well. Since fluorescence intensities varied considerably between cells in one field (**Figure 40**), it was impossible to find a global threshold that would include nuclear envelope pixels from all cells but exclude background pixels. Instead, we created masks for each image pair based on the 10% brightest pixels in the image from the parallel channel. This mask usually coincided with the nuclear envelope signal (**Figure 41**b).

A further aspect of data analysis that we aimed to automate was the quantification of anisotropy changes along the nuclear envelope cross-section, which would allow us to determine the orientation of fluorophores with respect to the NPC, as detailed above. Thresholded nuclear envelope image pairs were centered based on their center of gravity calculated from pixel intensities, and anisotropy values were averaged for eight sectors of the centered image (**Figure 42**).

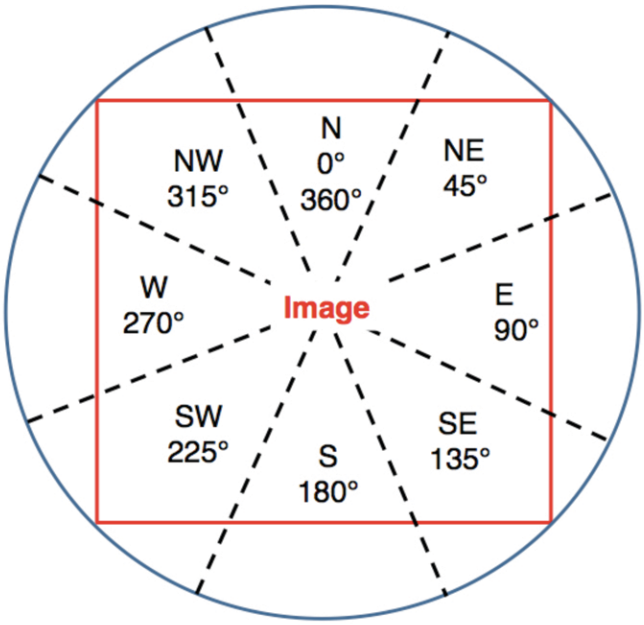

Figure 42 Anisotropy quantification in 8 image sectors. Nuclear envelopes were individually centered within square images, and the image was divided into 8 sectors, as shown. The average anisotropy value was calculated for each sector.

Anisotropy variation along the nuclear envelope cross-section for GFP attached to folded nup domains

As described above, GFP in a fixed orientation within the NPC is expected to give rise to an anisotropy that varies along the nuclear envelope cross-section. We tested a variety of yeast strains in which GFP was attached either to a nup domain that was predicted to be folded, or to an FG domain, which is presumably unfolded. As shown in (**Figure 43**), the anisotropy patterns between these two types of strains were indeed different.

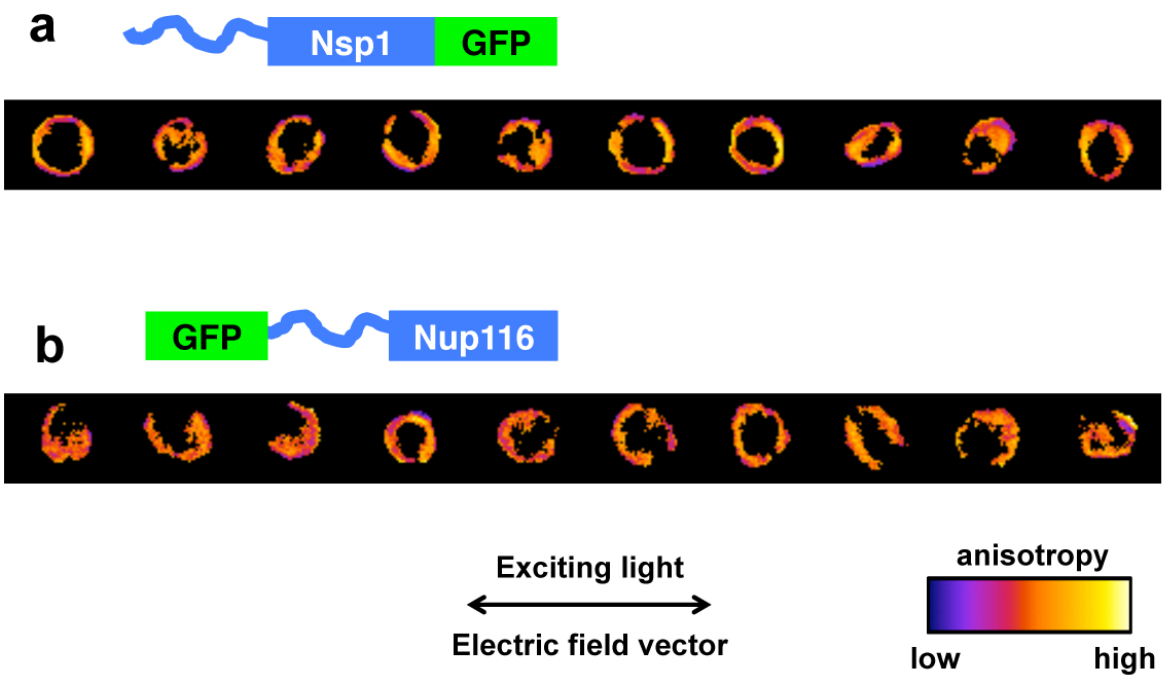

Figure 43 Anisotropy distribution along the nuclear envelope cross-section. Individual nuclear envelope anisotropy maps are shown after thresholding. (**a**) GPF attached to the ordered domain of Nsp1. Anisotropy values for the left and right edges of the nuclear envelopes appear higher than for the top and bottom edges. (**b**) GFP attached to the FG domain of Nup116. Anisotropy values do not seem to vary systematically along the nuclear envelope cross section.

To analyze anisotropy patterns in a large number of cells, we determined average anisotropy values for 8 sectors of the image (**Figure 44**). A comparison for GFP tagging of the structured and unstructured ends of Nup57 is shown in **Figure 44**. GFP attached to the structured C-terminus of

Nup57 has high anisotropy values for $\gamma = 0+n\cdot\pi$, and low anisotropy values for $\gamma = \pi/2+n\cdot\pi$, indicating that the GFP dipole is oriented close to the nucleo-cytoplasmic axis of the NPC. GFP attached to the unstructured N-terminus of Nup57 shows no significant variation in anisotropy around the nuclear envelope cross-section, suggesting that the GFP molecules are randomly oriented within the NPC.

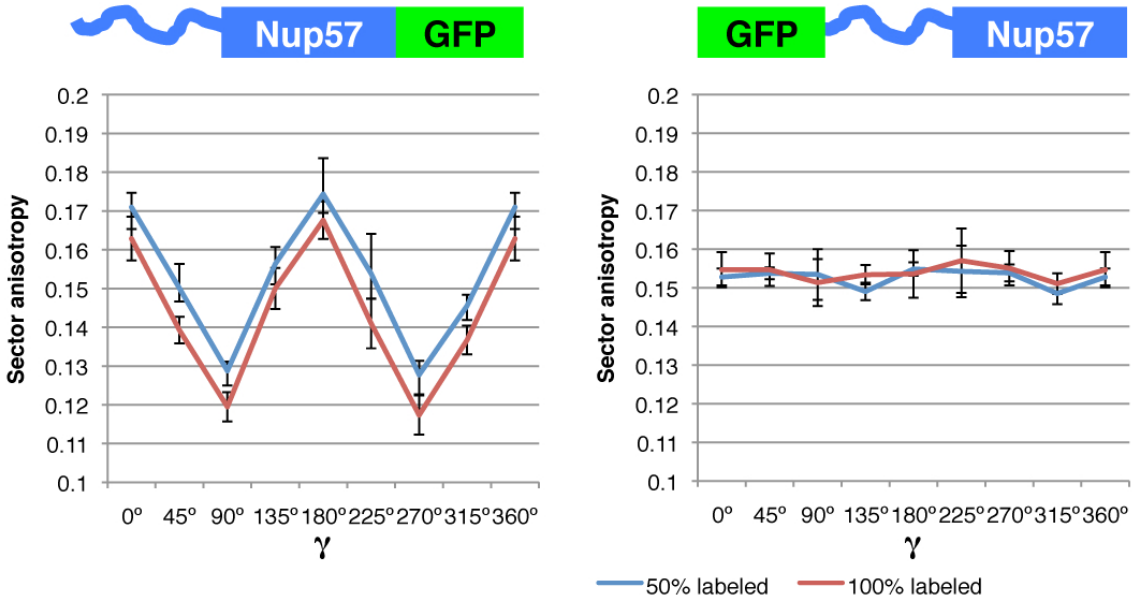

Figure 44 Average anisotropy values in different nuclear envelope sectors of four yeast strains: *Left*, structured domain of Nup57 labeled with GFP, 50% or 100% labeling ratio. *Right*, FG-domain of Nup57 labeled with GFP, 50% or 100% labeling ratio.

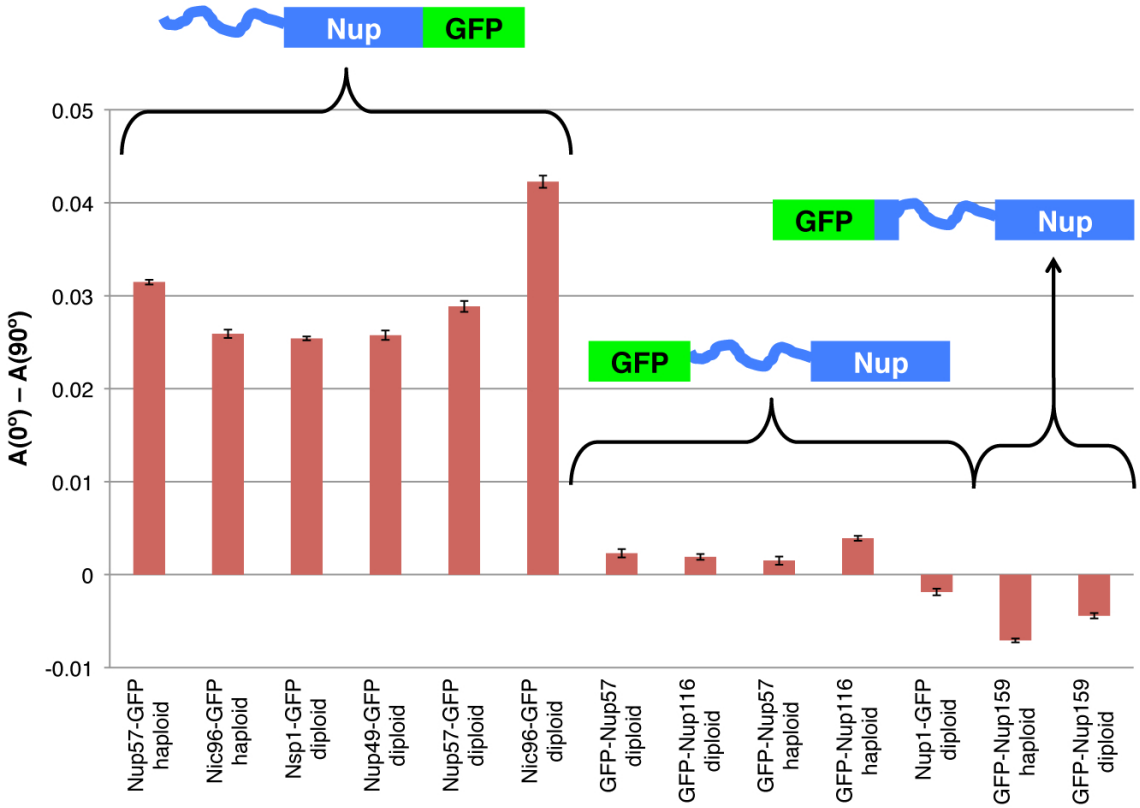

Figure 45 Comparison of anisotropy distributions for various yeast strains. The difference between the anisotropy at $\gamma=0$ and at $\gamma=\pi/2$ is shown. In the first six strains, GFP is attached to a structured domain. In the following five strains, GFP is attached to an FG domain. In the last two strains, GFP is attached to the N-terminal β-propeller of Nup159, which in turn is connected to the structured C-terminal domain of Nup159 by an FG domain. Data were collected on a different day than data shown in **Figure 44** and **Figure 46**.

Similar results were obtained for other nucleoporins as summarized in **Figure 45**. GFP attached to structured nup domains displayed considerable differences between anisotropy values at 0° and 180° on the one hand, and anisotropy values at 90° and 270° on the other hand.

Dipoles of GFP attached to the structured domains of Nup57, Nic96, Nsp1 and Nup49 seem to be oriented close to the nucleo-cytoplasmic axis of the NPC.

Nup159 is a special case, since the major structured domain of the protein is found at the C-terminus, and a β-propeller is found at the N-terminus (Weirich et al., 2004), linked to the C-terminal structured part by the unstructured FG-domain. The small negative anisotropy difference indicates that the orientation of the GFP dipole more similar to the nuclear envelope plane than to the nucleo-cytoplasmic axis. Possibly, the Nup159 β-propeller is less rigidly oriented with respect to the NPC, due to its attachment via the unstructured FG-domain. This would explain why the difference of anisotropy along the nuclear envelope cross-section is rather small.

GFP molecules attached to the FG domains of Nup57, Nup116 and Nup1 showed almost constant anisotropy values, indicating that they were randomly oriented with respect to the NPC. These findings are not surprising, but it is reassuring that our measurements support the generally accepted view that FG domains are disordered.

Homo-FRET revealed by varying GFP labeling ratio

In yeast, complete labeling of a given nup with GFP can be achieved by tagging the nup genomically in a haploid strain. Alternatively, both alleles of the nup gene can be tagged in a diploid strain. A reduced labeling ratio is obtained by labeling only one allele in a diploid strain. We will refer to this latter case as "50% labeled", even though the actual labeling ratio may differ from that exact value. (It may, if anything, be expected to be lower than 50%, if we assume that gene expression is less efficient for the longer construct than for the wild type gene, rather than vice versa.)

Homo-FRET is predicted to be more efficient in 100%-labeled strains, since their concentration of potential FRET acceptor molecules is higher than that in 50%-labeled strains. In order to detect homo-FRET, we therefore compared the anisotropy between strains that were 100% versus 50% GFP-labeled. We found significant differences for strains in which the structured domain of Nup57 was tagged, as well as for strains in which a GFP tag was inserted between the FG-domain and the structured domain of Nup116 (**Figure 46**).

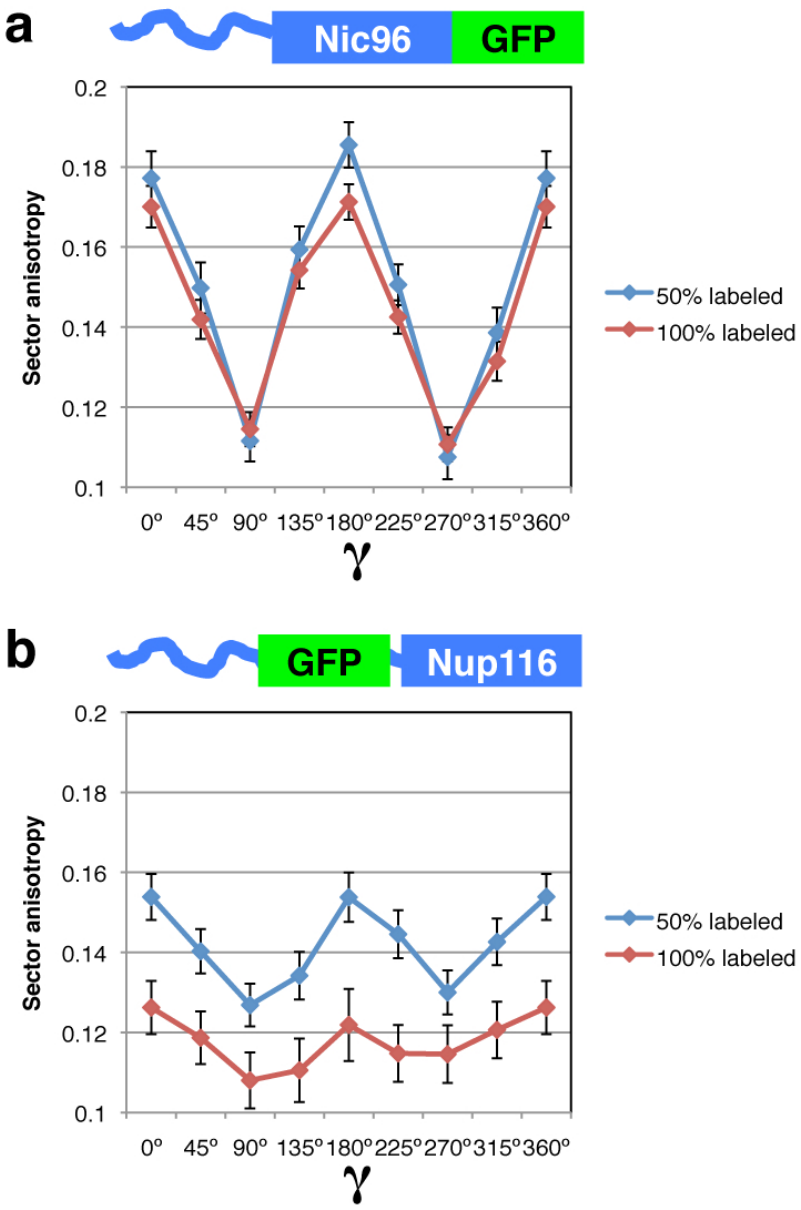

Figure 46 Increased GFP labeling ratio decreases anisotropy. Strains in which a nup is genomically GFP-tagged either in a haploid strain (100% labeling), or in a diploid strain that possesses a second, unlabeled copy of the same nup (50% labeling). *Top*, the structured domain of Nic96 was tagged. *Bottom*, a GFP tag was introduced between the FG domain and the structured domain of Nup116.

For both strains, the anisotropy is lower in 100% labeled strains than in 50% labeled strains. This effect is difficult to explain by other factors than homo-FRET, since the orientation or flexibility of GFP tags should not be affected by nearby GFP tags. Nic96 is thought to occur in 32 or more copies per NPC (Rout et al., 2000). Therefore, Nic96 homo-FRET is consistent with our prediction that homo-FRET between GFP molecules attached rigidly to ordered nup domains occurs only for nups present in at least 32 copies per NPC. Nup116 is thought to be present in 16 copies per NPC (Rout et al., 2000). The comparatively low amount of anisotropy variation along the nuclear envelope cross-section may be indicative of the fact that the GFP tag adjacent to the FG domain displays some degree of variability in its orientation, thus increasing the effect of homo-FRET on anisotropy values.

Blocking active transport through the NPC

In order to study NPC dynamics, such as dilation or FG-domain movements that specifically accompany active transport through the NPC, we needed to block transport through the NPC. We tested two methods that were developed by others (Shulga et al., 1996; Strawn et al., 2004). To monitor active transport in live cells, we used a GFP-NLS reporter, which is actively

transported into the nucleus under normal conditions, but equilibrates between nucleus and cytoplasm when transport is blocked, since it is small enough to diffuse through the NPC passively (**Figure 47**).

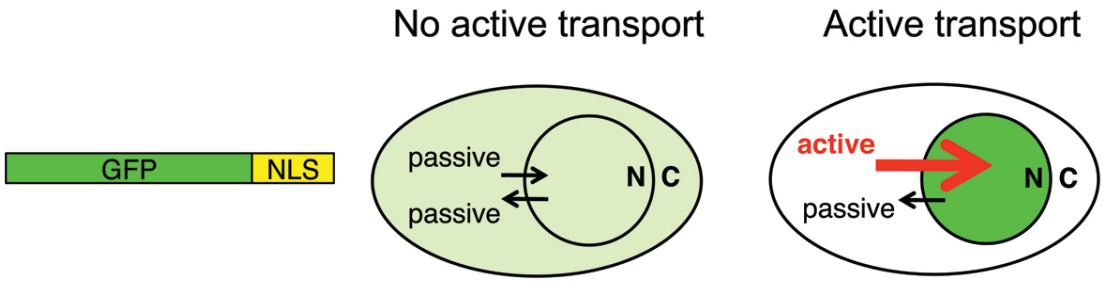

Figure 47 A GFP-NLS reporter for active transport through the NPC. In the absence of active transport, the reporter equilibrates between the nucleus and the cytoplasm due to passive diffusion through the NPC. In the presence of active transport, the reporter accumulates in the nucleus.

As described in Chapter 1, active transport through the NPC is driven by a Ran gradient, which in turn is established by the action of two asymmetrically distributed regulators of Ran: Ran-GEF in the nucleus and Ran-GAP in the cytoplasm. Temperature-sensitive alleles of these two factors have been found in yeast. We successfully induced a transport block in mtr1–1 (ran-GEF) mutant cells (Booth et al., 1999) by shifting them to the restrictive temperature (**Figure 48**). However, recovery was relatively fast after shifting back to the permissive temperature, and it was not easy to

control the temperature of the microscope stage and objective precisely. An additional concern was that temperature may have several indirect effects on GFP anisotropy, which may confound the analysis of effects due to changes in NPC structure dynamics.

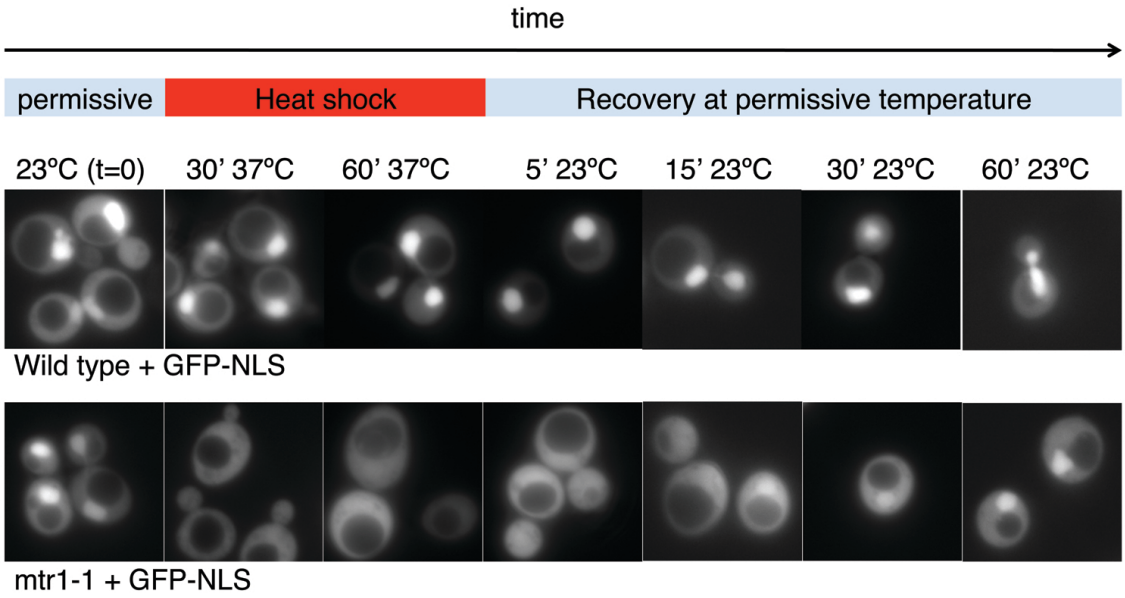

Figure 48 Transport block in a temperature-sensitive Ran-GEF (mtr1-1) mutant strain. Cells expressing the GFP-NLS reporter (**Figure 47**) were grown at 23ºC, shifted to 37ºC for one hour, and shifted back to 23ºC. GFP epifluorescence micrographs were taken at various time points to monitor the subcellular distribution of the reporter. *Top row*: wild type cells as negative control. *Bottom row*: Ran-GEF temperature sensitive mutant strains.

We therefore tested an alternative, less specific way of blocking transport NPC: By treating the cells with deoxy-glucose and sodium azide, they are rapidly depleted of ATP, which will in turn deplete GTP and block transport. This method worked efficiently (**Figure 49**), but caused an increase in background fluorescence, thus affecting the measured anisotropy values. We are currently developing computational methods of background subtraction to solve the problem.

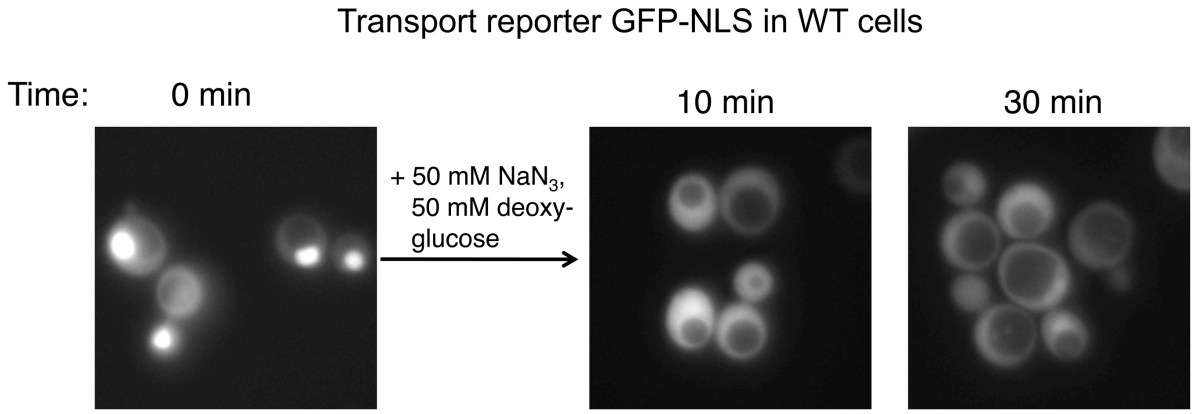

Figure 49 Transport block by energy depletion. Sodium azide and deoxyglucose were added to wild type cells expressing a GFP-NLS reporter (**Figure 47**), and GFP epifluorescence micrographs were taken at different timepoints.

CHAPTER 4: Discussion and Future Directions

Three-dimensional structure of the Nup84 complex

I solved 3D structures of an entire NPC subcomplex, the heptameric Nup84 complex from budding yeast. My data confirm the overall architecture that was proposed previously based on 2D EM (Lutzmann et al., 2002). Averaging of images allowed me to discern additional details, such as four globular regions and the asymmetry of the two arms of the particle, and to characterize the conformational heterogeneity of the particle. The 3D maps, in combination with protein labeling experiments, enabled me to dock available nup crystal structures into the heptamer structure.

The EM structures (**Figure 18**) do not necessarily represent the conformation of the heptameric complex in the context of the NPC since (i) interactions with other nups may affect the conformation of the heptameric complex, and (ii) the present structures are of the particle bound to a planar support film, whereas in the context of the NPC, the heptameric complex coats a highly curved surface. Distortions of the particle structure caused by negative staining and by missing-cone effects due to incomplete angular coverage of particle views are a potential concern, but they are

unlikely to be dramatic in the present study, since the particle is not very extended in the direction perpendicular to the carbon support film. The simultaneous iterative reconstruction technique was used to minimize missing-cone effects. The docking of nups into the EM map (**Figure 27**) represents the best possible fit given the current data; future higher-resolution EM maps and additional crystal structures may lead to a refinement of nup positions and orientations.

Despite these caveats, the present 3D structures yield fundamental insights into the architecture of the heptameric complex. The main architectural principle of the heptameric complex is that the globular domains at the ends of the arms and the stem are formed by β-propeller domains, whereas the thinner connecting segments are formed mainly by α-solenoid folds. While the crystal structure of Nup120 is not yet available, we expect Nup120 to conform to this principle: the shape of the long arm strongly suggests that the predicted Nup120 β-propeller localizes to the thick, globular end of the arm, whereas the predicted α-helical regions form the thinner connection to the vertex. This arrangement is supported by the 2D class averages (**Figure 13**): the long arm ends in a round shape ~5 nm in diameter with a central hole or depression, compatible with a β-propeller in top view. Intriguingly, the same architectural principle of α-solenoid arms

ending in β-propeller domains is also found in the clathrin triskelion(Fotin et al., 2004), thus lending further support to the hypothetical evolutionary relationship between vesicle coats and the heptameric complex.

β-propellers occur in many biological contexts, frequently acting as platforms for interactions with other proteins. The structural basis for this function is their rigid fold and the availability of several highly variable interaction surfaces (Paoli, 2001). Remarkably, the surfaces of the four β-propellers in the heptamer are mostly exposed, and thus available for interactions with other proteins. As suggested previously (Brohawn et al., 2008; Debler et al., 2008; Hsia et al., 2007), the β-propellers may be involved in higher-order interactions between heptameric complexes within the NPC. Such an arrangement occurs in the COPII vesicle coat (Fath et al., 2007). Moreover, a scaffold formed by heptameric complexes is likely to form a platform that organizes other nups within the NPC.

Whereas the β-propellers are rigid structural units, the connecting regions formed by α-solenoids and, possibly, by unstructured regions are likely to account for the conformational flexibility of the heptameric complex. Flexibility of α-solenoid arms was described for both COPII coatamers (Fath et al., 2007) and clathrin triskelia (Ferguson et al.,

2008), where it is thought to allow the formation of vesicle coats in different sizes.

In **Figure 50**, the present EM map of the Nup84 complex is compared to the computationally generated model by Alber and colleagues (Alber et al., 2007). Although the overall dimensions of the complex are similar, the arrangement and interactions of nups found by EM and crystallography differs from the computational model. Most notably, Sec13 is predicted to interact only with Nup84 by Alber and colleagues, whereas it forms a very intimate complex with Nup145C in the crystal structure: one blade of the Sec13 β-propeller is formed by Nup145C. Furthermore, the present EM map shows no direct interaction between Sec13 and Nup84. These findings highlight the importance of classical structural biology techniques to confirm results from computational modeling approaches.

Figure 50 Comparison between the EM map and the model by Alber and colleagues. (**a**) Segmented EM map of the Nup84 complex. (**b**) Computational model for the Nup84 complex (Alber et al., 2007). Color was added to facilitate comparison with the EM map. (a) and (b) are drawn to scale. (**c**) "Protein adjacencies" within the Nup 84 complex, according to Alber et al., 2007. The indicated edge weights correspond to the fraction of computational models of the entire NPC in which the proteins connected by the edge are in direct contact.

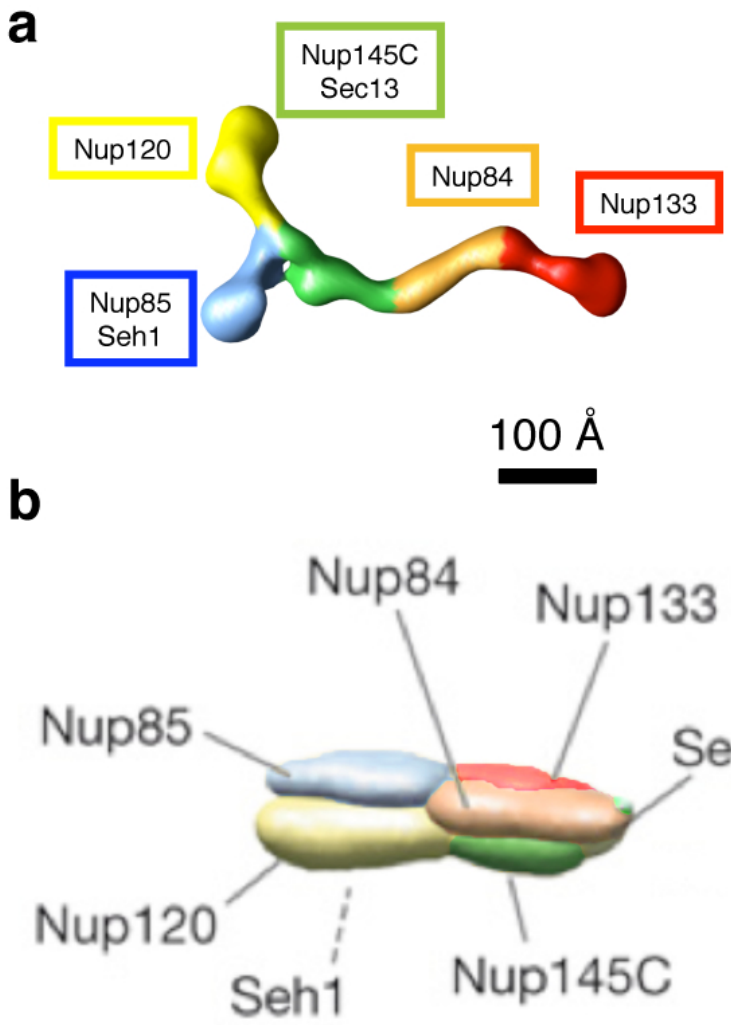
a
Nup145C
Sec13
Nup120
Nup84
Nup133
Nup85
Seh1
100 Å
b
Nup84
Nup133
Nup85
Sec13
Nup120
Seh1
Nup145C
c
Sec13
0.66
Nup84
0.54
Nup85
0.57
1.0
Nup133
1.0
0.49
0.6
Seh1
0.59
0.84
52
Nup145C
0.5
Nup120

Figure 50

A model for the role of the Nup84 complex in NPC assembly

The heptameric complex was reported to play an essential role in the formation of NPCs, both post-mitotically and during interphase. Immunodepletion of the vertebrate homologue of the heptamer from nuclear assembly reactions leads to the formation of a continuous nuclear envelope devoid of pores (Harel et al., 2003; Walther et al., 2003). Similarly, the heptamer is required for *de novo* insertion of NPCs into the interphase nuclear envelope (D'Angelo et al., 2006). While the mechanism of NPC assembly is currently unknown, a specific structural role for the heptameric complex in this process can be envisaged based on its structure and its affinity for highly curved membrane surfaces.

Formation of new NPCs during interphase requires the formation of a fusion pore between the outer and inner nuclear membranes. In other biological contexts, membrane fusion was shown to occur by a stepwise process: apposition of two membranes, hemifusion between the inner leaflets of the two lipid bilayers, reversible formation of a small fusion pore, stabilization and expansion of the fusion pore (Chernomordik and Kozlov, 2008). In different biological processes, such as exocytosis or viral membrane fusion, these steps are catalyzed by specific proteins that interact

with the membranes to overcome the inherent energy barriers of each step along the fusion pathway, and to control the geometry of fusion.

The heptameric complex may function in one or several phases during the formation of nuclear envelope pores (**Figure 51**). The formation of the initial fusion pore is likely catalyzed by integral membrane proteins, possibly by the poms, which are components of the mature NPC. The heptamer may then stabilize initial fusion pores, by binding to the sharply bent membrane lining the pore. The following step of fusion pore expansion is particularly interesting in the case of nuclear envelope pores: whereas in other biological contexts, such as vesicle fusion, fusion pores expand maximally to integrate the vesicle membrane into the target membrane, the nuclear envelope fusion pore expands to a defined diameter of ~100 nm to accommodate the NPC. A scaffold formed by several heptamers may control the final size of the fusion pore, and thus act as a molecular ruler.

Once the heptamer scaffold has stabilized the 100 nm pore, it can serve as a platform for the recruitment of other nups. The eightfold symmetry of the NPC may be dictated by the eightfold symmetry of the initial scaffold formed by heptameric complexes.

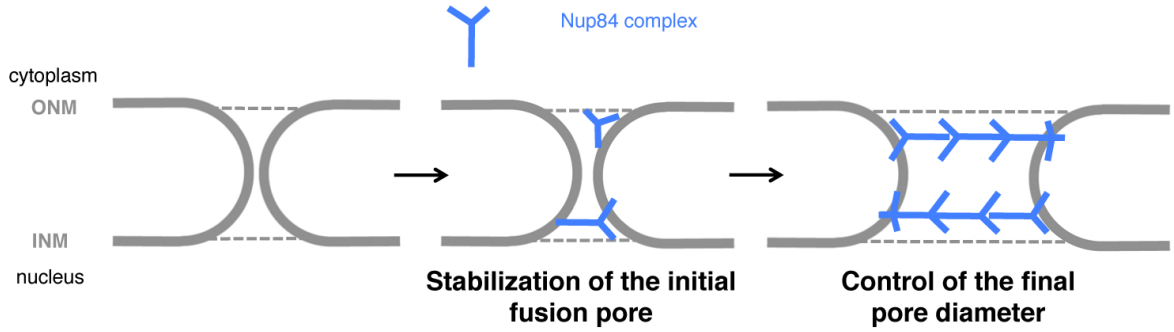

Figure 51 Hypothetical role for the heptameric complex in NPC assembly. Interphase formation of NPCs requires a fusion between inner and outer nuclear membranes, which is presumably by transmembrane proteins yet to be identified. The heptameric complex may recognize and bind the sharply bent fusion pore membrane, thereby stabilizing it. Assembly of a scaffold of heptameric subcomplexes may define the final diameter of the pore, and possibly also determine the eightfold symmetry of the mature NPC. The nature of the scaffold is currently unknown; it may consist of two or four rings, or some other arrangement of heptamers.

The architecture of a scaffold formed by Nup84 complexes is as yet unknown. Unfortunately, I was not able to observe higher-order assemblies of the heptamer directly by EM. Interactions between heptamers are likely unstable outside the context of the NPC. This may even be a physiological requirement, since these interactions would have to dissociate to allow the passage of integral membrane proteins of the inner nuclear membrane through the NPC (King et al., 2006).

Several models have been proposed for the structure of a Nup84 complex scaffold in the context of the NPC. The heptameric complex was suggested to assemble into a head-to-tail arrangement of eight heptameric complexes in a ring (Hsia et al., 2007). I built such a hypothetical head-to-tail ring from the EM maps (**Figure 52**), and the resulting diameter is ~100 nm, which corresponds to the observed outer diameter of the NPC.

It was also proposed that four such rings in an anti-parallel arrangement would form an outer cylinder of the NPC, in which hetero-octamers of Nup85·Seh1 and Nup145C·Sec13, which were observed in crystals, form poles parallel to the nucleocytoplasmic axis (Debler et al., 2008; Hsia et al., 2007). The present EM data does not necessarily support such an arrangement, since Nup85·Seh1 and Nup145C·Sec13 are only separated by ~10 nm within one heptamer, whereas the anti-parallel cylinder model would require them to be separated by about half the length of the entire heptamer, i.e. 20 nm or more (Debler et al., 2008; Hsia et al., 2007). However, it cannot be excluded that the structure of the heptameric complex within the NPC differs drastically from the structure observed by single-particle EM. Furthermore, it is possible that either the Nup85·Seh1 or the Nup145C·Sec13 hetero-octamer pole exist in the NPC, but not both.

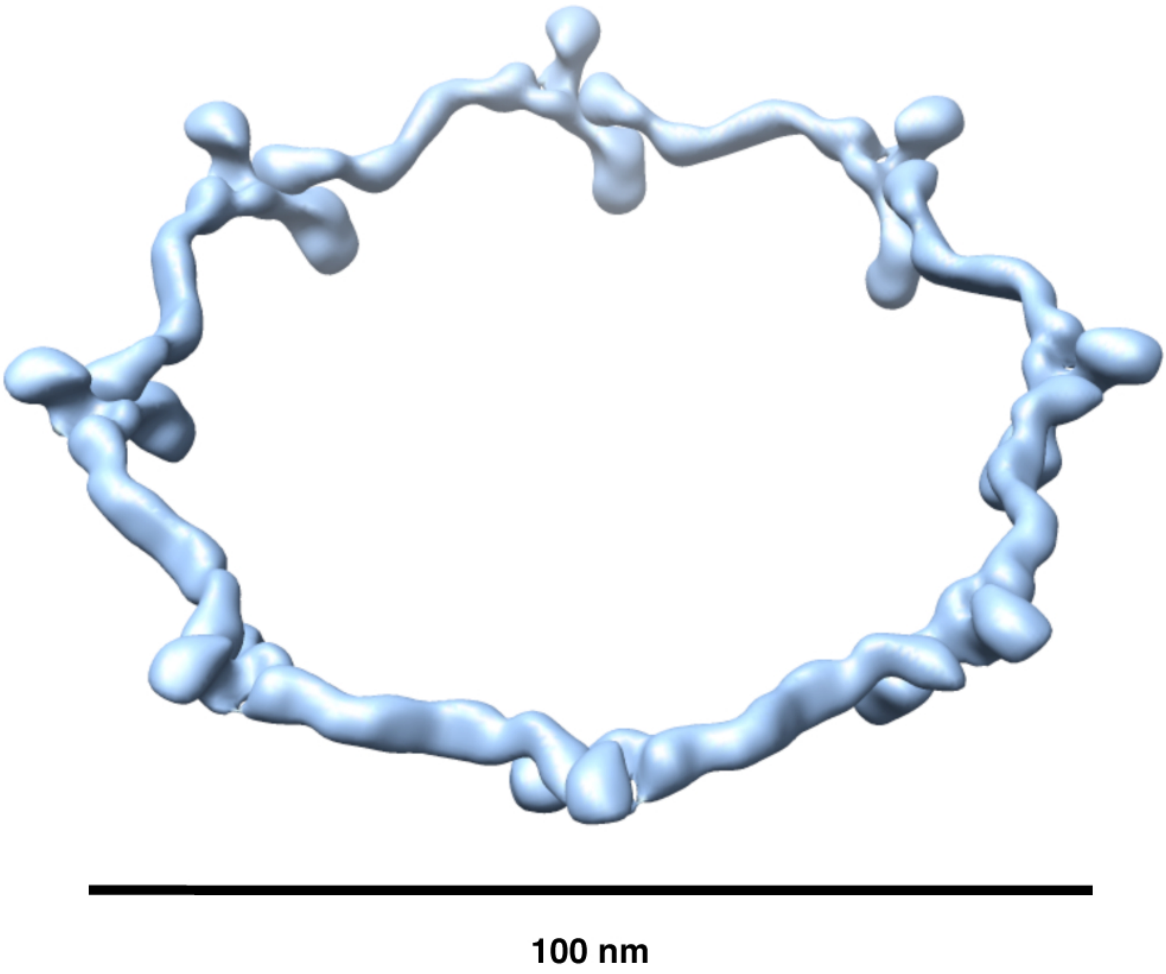

Figure 52 Hypothetical model for a head-to-tail arrangement of eight heptamers in a ring. The ring diameter of ~100 nm is in good agreement with the outer diameter of the yeast NPC.

An alternative model for the arrangement of Nup84 complexes within the NPC was suggested (Brohawn et al., 2008) in which eight heptamers interact via their Nup85·Seh1 and Nup120 arms to form a ring. In

this model, the stem would be approximately parallel to the nucleocytoplasmic axis. Two such rings were suggested to be linked by a scaffold formed by other nups, including Nic96. Based on the present EM structure, one such ring would be ~45 nm high, the entire assembly would thus be higher than 90 nm, which is not compatible with the observed NPC height of ~30 nm. However, we need to consider again the possibility that the structure of the Nup84 complex within the NPC differs significantly from the structure of the isolated particle.

Flexibility and Dynamics in the NPC

The flexibility of the heptameric complex is also potentially of physiological relevance. Flexibility of the entire NPC was described (Akey, 1995; Beck et al., 2004; Beck et al., 2007) and may reflect conformational changes that accompany active transport. In particular, dilation of the NPC may be required to allow passage of large cargoes, such as ribosomal subunits. Molecular sliding of nups located near the central channel of the NPC was suggested to form the basis for NPC dilation (Melcák et al., 2007). It is likely that conformational changes of these central nups would occur in concert with conformational changes of the more peripheral nups, including

the heptameric complex. A further requirement for flexibility may apply to the vertebrate homologue of the heptameric subcomplex, which has additional functions outside the NPC during mitosis (Lim et al., 2008), and may adopt distinct conformations in different cellular contexts.

Interestingly, the length of the heptameric complex was constant in the different conformations we observed (**Figure 12**). This means that a ring of heptamers could maintain a fixed size based on head-to-tail interactions, while the flexibility of the heptamer would buffer conformational changes of other parts of the NPC that are anchored to the heptamer ring (**Figure 53**).

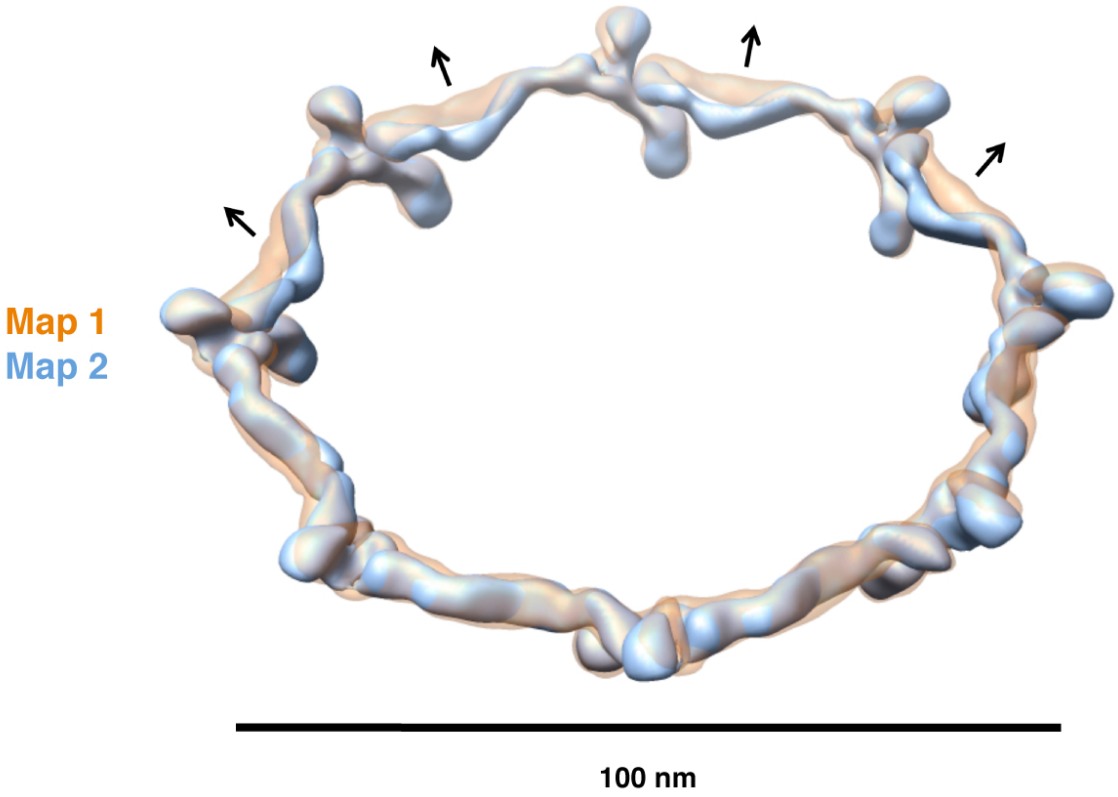

Figure 53 Hypothetical model for conformational changes of the heptameric complex within the NPC. Rings of eight heptamers, map 1 (orange) and map 2 (blue) are shown as transparent overlay. Remarkably, the head-to-tail length is identical for both conformations of the heptamer. The main difference is the movement of the stem hinge region. The flexibility of the heptamer in this region may be involved in buffering conformational changes of other parts of the NPC that are anchored here, while stabilizing the overall structure of the NPC and its interaction with the pore membrane.

Future studies addressing the interaction of the heptameric complex with other nups and membranes

The structure of the heptameric complex raises further interesting questions: If the subcomplex is the membrane-coating module of the NPC, how does it interact with membranes? Do heptamers form higher-order oligomers within the NPC? How does the heptamer interact with other nups? In a continuation of the work presented here, I will attempt to answer some of these questions.

The β-propeller domain of Nup133 was shown to interact directly with small liposomes in a sucrose flotation assay (Drin et al., 2007). I plan to test the binding of the entire heptameric complex to liposomes of different sizes in a similar assay. The composition of the liposomes will be designed to approximate the physiological lipid composition of the yeast nuclear envelope (Zinser et al., 1991). If stable complexes between the heptameric complex and liposomes can be obtained, I will investigate their structure by cryo-EM. Liposomes are known to generate cryo-EM images with good contrast.

In addition, I will attempt to obtain 2D crystals of the heptameric complex at a planar phospholipid interface. This technique has successfully been used in the structure determination of both integral membrane proteins and soluble proteins. The setup of 2D crystallization

trials is illustrated in **Figure 54**. A solution of the protein of interest is placed in a well, and a phospholipid monolayer is created at the surface of the aqueous buffer. If the protein interacts with the lipid head groups, it accumulates at the monolayer surface. The local concentration becomes so high that ordered arrays or 2D crystals form. The monolayer and bound particles are transferred to a grid and imaged by EM. The binding of the particle to the lipid head groups can be promoted by including positively charged lipids, which electrostatically interact with negatively charged protein surfaces (Darst et al., 1988), or by including chemically modified lipids that specifically interact with the target protein (Bischler et al., 1998; Darst et al., 1991). Initially, I will attempt to obtain 2D crystals of the heptamer bound to phospholipids approximating the yeast nuclear envelope composition, in order to observe potentially the physiological mode of membrane interaction.

If 2D crystals can be obtained, the particle will be fixed in one conformation, which will allow the determination of its structure at considerably higher resolution. Even if the heptamer does not crystallize, the high local concentration at the 2D interface should promote interactions between heptamers, which may reveal the physiological binding mode by

which heptamers form higher-order assemblies within the context of the NPC.

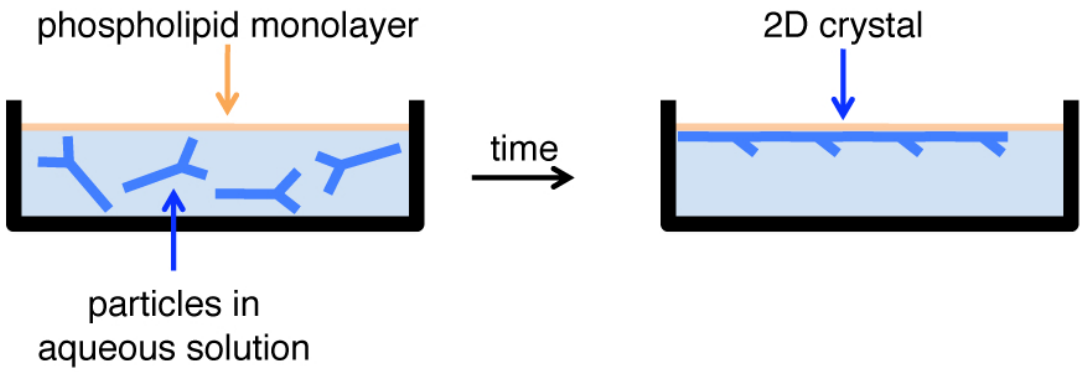

Figure 54 2D crystallization trial, schematic diagram. See text for details.

The heptamer also interacts with other nups within the NPC, such as Nup157 and Nup145N (Lutzmann et al., 2005). I will attempt to reconstitute complexes between the native heptameric complex and recombinant nups purified by other members of the Blobel lab, and to determine the 3D structure of these complexes by single-particle EM as before. The volume corresponding to the additional bound nup will be identified by difference mapping.

Together, these future experiments should expand our understanding of the structural role of the Nup84 complex in the complex of the NPC.

Interpretation of fluorescence anisotropy measurements of GFP-tagged nups

We established experimental and computational techniques to allow us to measure the fluorescence anisotropy of GFP-tagged nups in live yeast cells by polarized fluorescence microscopy. GFP attached to ordered nup domains was oriented with respect to the NPC, whereas GFP attached to FG domains appeared randomly oriented. In two cases, we observed homo-FRET between GFP tags.

For the interpretation of these results in terms of their biological significance, a number of caveats need to be taken into account. When GFP is attached to nups, different scenarios can be envisaged:

(i) The GFP can be linked rigidly to the nup, so that GFP dynamics reflect dynamics of the tagged nup domain.

   a. A nup highly oriented with respect to the NPC would orient the GFP dipole with respect to the NPC.

   b. Tagging of a flexible nup domain, such as the FG domain, would result in GFP dipoles that are not oriented with respect to the NPC

(ii) The link between the GFP and the nup can be so flexible that GFP dynamics do not reflect dynamics of the nup it is attached to. The GFP will appear randomly oriented, and possibly flexible, although the nup domain it is attached to is perfectly oriented.

(iii) Within the NPC, there may only be a limited number of "niches" that can accommodate GFP tags without causing steric clashes with nups. The orientation of the GFP tag may therefore reflect its optimal positioning in a nearby niche, rather than properties of the nup it is attached to.

We are planning to rule out the "niche" scenario using an approach developed in the Mitchison lab (Vrabioiu and Mitchison, 2006, 2007): the N-terminus of GFP is formed by a short α-helix, which can be fused to the C-terminal α-helix of a suitable target protein, to yield a defined, rigid linkage between the target and the GFP tag. Furthermore, a defined number of α-helix-favoring residues can be introduced, such that the linking α-helix is extended. The extension will result in a rotation of the GFP tag around the α-helical axis. The angle of this rotation can be predicted from the known geometry of the α-helical fold. If the GFP dipole rotates in space as predicted when the α-helix is extended, it can be assumed that the GFP orientation depends on the nup and the rigid linker, rather than

on a niche constraining the nup. Almost half of the yeast nups are predicted to feature C-terminal α-helices (Devos et al., 2006) and are thus potential targets for the helical extension approach.

The anisotropy values we obtained were lower than expected. For unoriented GFP tags, a value of ~0.4 would be expected for static GFP, and a value of ~0.32 for freely rotating GFP. Even homo-FRET would not be sufficient to lower the values below ~0.2, based on my calculations.

One possible explanation is that some of our initial assumptions do not apply. Not all nuclear envelopes are perfect spheres, and the geometric heterogeneity should lead to lower average anisotropy values. Furthermore, the volume imaged by polarized fluorescence microsopy is not an infinitely thin central section through the nuclear envelope. The focal depth of the microscope is such that light is collected from a thicker section of the nuclear envelope, possibly corresponding to ~1/3 of the nuclear diameter. Thus, fluorescence from NPCs in different orientations is averaged for each value of γ, leading to a decrease in anisotropy. While this effect can be ignored for larger spheres, such as cells (Axelrod, 1979), it may become very significant for the comparatively small yeast nuclear envelope. It is difficult to apply accurate corrections for this effect, since the exact spatial intensity distribution of the focal field is not known.

An alternative method for determining anisotropy values would be the cuvette measurement of a yeast suspension. In that case, the anisotropy would be averaged over all nuclei of the entire population, and information about the spatial orientation of GFP dipoles with respect to the NPC would be lost. However, an independently measured value for the anisotropy of unoriented fluorophores would be obtained, and serve as a control for the values obtained by microscopy.

Future studies addressing NPC architecture and dynamics in live yeast cells

Two important questions about NPC dynamics remain to be answered: (i) what is the gating mechanism – in particular, do FG domains form a static meshwork that operates by hydrophobic exclusion, or a highly dynamic polymer brush that operates by entropic exclusion? (ii) Does the observed plasticity of NPC structure reflect conformational changes that accompany active transport, such as NPC dilation to allow the passage of large cargo?

To answer the first question, we will confirm anisotropy values for tagged GFP domains from independent microscopy and cuvette measurements. We will also tag the free ends of FG domains with other fluorophores, such as small biarsenical dyes that bind to short tetracysteine

motifs in live cells, in order to confirm that the measured anisotropy values reflect properties of the FG domains, rather than the fluorescent tag.

To answer the second question, we will optimize our transport block protocols and then compare homo-FRET between GFP-nups before and after transport block. Dilation during transport should be reflected in a reduction in homo-FRET. We will also construct strains in which a second species of nup is tagged with mCherry, which is as an efficient hetero-FRET acceptor with GFP as a donor. This will enable us to quantify FRET independent of anisotropy, which is a great advantage because anisotropy is influenced by a number of factors, as discussed in Chapter 3.

A third application of the techniques we have developed will be the determination of nup orientation within the NPC. In combination with the α-helical extension approach described in the previous section, we should be able to confidently map the orientation of nups containing C-terminal α-helices. In cases where the crystal structure of the C-terminal nup domain is known, this will allow us to predict the orientation of the entire nup domain with respect to the NPC. In the case of the Nup84 complex, very different models for the arrangement of the complex in the context of the NPC have been proposed (Brohawn et al., 2008; Hsia et al., 2007). The orientation in which the Nup84 is placed within the NPC differs by 90º

between the two models. Our method should therefore be uniquely suited to distinguish between the two models *in vivo*.

CHAPTER 5: Materials and Methods

Plasmids

All plasmids used are listed in **Table 1**. Oligonucleotide primers used in the construction of plasmids and yeast strains were ordered from IDT DNA Technologies. Each primer was assigned a number, and the oligonucleotide sequences of all primers are listed in**Table 2**.

Plasmids were constructed using standard molecular cloning techniques (Sambrook et al., 1989). Polymerase chain reactions (PCR) were carried out using Kod HiFi DNA polymerase (VWR) following the supplier's protocol. Magnesium concentration, extension time and annealing temperature were optimized for each PCR reaction, if necessary. Restriction endonucleases and T4 DNA ligase and mung bean nuclease were purchased from New England Biolabs.

Plasmid CP429 was a gift from Susan Wente (Vanderbilt University).

Plasmid pMK484 was constructed by PCR-amplifying yeast-optimized EGFP from pKT127 with primers 1027 and 1030 to introduce PacI and AscI restriction sites and a Gly-Gly-Ser-Gly-Ser-Gly-Gly spacer at

the N-terminal end of EGFP. The PCR product was digested with PacI and AscI and ligated into the backbone of pKT127 from which the insert encoding EGFP had been removed by PacI/AscI cleavage. Plasmid pMK485 was constructed by ligating the same insert into the backbone of pKT174, from which the ECFP sequence had been removed by PacI/AscI cleavage. Plasmid pMK489 was created by removing the ECFP sequence from pKT174 by PvuII/AscI cleavage, mung-bean nuclease digestion of the 5'-single-stranded extension of the AscI-cleaved end and religation of the blunt ends. To create plasmid pMK490, the EGFP coding sequence from pKT127 was PCR-amplified using primers 1079 and 1080, which introduced SacI and SpeI sites as well as Gly-Gly-Ser-Gly-Ser-Gly-Gly spacer at the C-terminal end of GFP. This PCR product, as well as pMK489, were digested with SacI and SpeI and ligated to yield pMK490.

Plasmid pMK468 was constructed by PCR-amplifying yeast-optimized EGFP from pKT127 with primers 965 and 968 to introduce XhoI and HindIII restriction sites, as well as a Kozak sequence upstream of the open reading frame, and ligating it into the SalI/HindIII digested backbone of pUG27.

Plasmid number	Description	Parent plasmid	Source
CP429	GFP-NLS	–	Strawn et al., 2004
pKT127	yEGFP-KanR	–	Sheff and Thorn, 2004
pKT128	yEGFP-SpHIS5	–	Sheff and Thorn, 2004
pKT174	yECFP-CaURA3	–	Sheff and Thorn, 2004
pRS422	ADE2-containing plasmid	–	Christianson et al., 1992
pSH47	P_{GAL1}-cre	–	Gueldener et al., 2002
pUG27	loxP- SpHIS5-loxP		Gueldener et al., 2002
pMK468	loxP- SpHIS5-loxP-Kozak-yEGFP	pUG27	This study
pMK484	GGSGSGG-yEGFP-KanR	pKT127	This study
pMK485	GGSGSGG-yEGFP-CaURA3	pKT174	This study
pMK489	CaURA3	pKT174	This study
pMK490	CaURA3-yEGFP-GGSGSGG	pMK489	This study

Table 1 Plasmids used in the present work. Details about the construction of these plasmids are provided in the text.

#	Oligonucleotide sequence (5’ to 3’ end)
920	GAAACGTACAGCACTTTAATTAATATAGACGTCTCTCTAg gtgctggtttaattaacatg
921	TACTGATATATAGATATAAACAAAAATATACAATATTTA AAAtcgatgaattcgagctcg
922	TCCACCTCTCTGGAAAAACAAATCAACTCGATAAAGAAA ggtgctggtttaattaacatg
923	ATGTCAAATAAGTGTAGAATAGAGGGAATTTTTTCTTTTA GAtcgatgaattcgagctcg
924	TTACATCAAAAAACGAAAACACTGGCATCATTGAGCATA ggtgctggtttaattaacatg
925	GTACTTGTTATACGCACTATATAAACTTTCAGGGCGATTT ACtcgatgaattcgagctcg
926	AAAGATGCTGCAATTGTAAAAAAATATAAAAATAAAACG ggtgctggtttaattaacatg
927	ATCGATCTTTATACAATTCAGTCATTGATTTAAGTAACCT GAtcgatgaattcgagctcg
931	gactaaggttggccatggaactgg
965	cctgAAGCtttgtacaattcatccataccatggg
968	cgtaCTCGAGtaaaaaatgtctaaaggtgaagaattattcactgg
972	GTAACAAAAGACATACCTTGTTGACCAATTGATCACgccact agtggatctgatatcacc
973	CGAACCCGTTATTACTACCGCTGAAACCAAACATtttgtacaatt catccataccatggg
978	ATTCAGCTTCGAAGATTTCTTTTTTAAAACATTATTgccacta gtggatctgatatcacc

979	CGCTGGGGAATGCGCCACGGCTAACTCCAAACATtttgtacaat tcatccataccatggg
982	TAAATATATATATATTGATTACAGAACCATTATAACgccact agtggatctgatatcacc
983	TCTCAGTGGGTACTTCATCCTTCAAAGAAGACATtttgtacaatt catccataccatggg
984	CAGAAAGATTGCAAGAATGAGGCACTCTAAAAGGatgtctaa aggtgaagaattattcac
985	CCTTCAGAAAAGCAACACAATACCTAATTACATAACCGA TATtcgatgaattcgagctcg
1027	ggTTAATTAAggtggttctggttctggtggtATGTCTAAAGGTGAAGAA TTATTCACTGG
1030	TATggcgcgccTTATTTGTACAATTCATCCATACCATGGG
1031	ACTATACCATCAACTATGAAACCAACACTGTAGAATACgg tggttctggttctggtggtA
1032	CCAGTAAAGTTTATTATATATATGTAAAATTGTATTATAG catcgatgaattcgagctcg
1041	TTGAGGGTAAATGGGAACCCGCTGGTGAAGTTCATCAGgg tggttctggttctggtggtA
1042	TTTTCTTTTGAGATGTTTCATTTTAAATTCTTGATACTCTcat cgatgaattcgagctcg
1043	ATGAATTTAAGTGTATGTCAGTAATTACTGCCCAACAAggt ggttctggttctggtggtA
1044	AAGTACCAATATATAATGTTATGTATACATATATTCTTATc atcgatgaattcgagctcg
1046	CCTATTGATCAGAATGCCATACGTGAAG
1050	GAACTTCTAAGCGAGCATGATGACC

1051	GGACTCAAGACAATGAACAAGGCCC
1084	atgtctaaaggtgaagaattattcactgg
1085	ttcttggccacccatatcacg
1086	gtagttgggcagatattaccaatgctc
1087	accaccagaaccagaaccac
1088	GGATATGATAACTTCAATACAACTCATCG
1089	ccagtgaataattcttcacctttagacatATGGCTATCCTAATGTACTTCACTTGAATTG
1091	gtggttctggttctggtggtATGAGTGAAAAAAAAGTACATCTTCGTTTGCGG
1092	CTTGTGGTCATTGACTAGTCCATATCC
1164	TTGGTAGCAAACCTGCTACAGGATCC
1165	ccagtgaataattcttcacctttagacatACTACCAAACAGGCCCGTTGAACC
1166	cccatggtatggatgaattgtacaaaAATAACACCTCTCAATCTACTAATGCTGGAG
1167	CATTTTGTATGCGTTCGTCAAACTGGC

Table 2 Oligonucleotide sequences of primers used in this study. Alternating upper case and lower case letters are used to denote different elements of the primer, such as sites recognized by restriction endonucleases, spacer sequences, sequences annealing to the PCR template.

Yeast strains

All yeast strains used in the studies described in this thesis are listed in (**Table 3**). Standard procedures of yeast genetics were followed for the mating of haploid yeast strains, tetrad dissection of sporulated diploid strains and general strain maintenance (Sherman, 2002). Changes of the yeast genome sequence were achieved by the commonly used strategy of transformation with PCR-generated linear fragments (Sheff and Thorn, 2004) unless specified otherwise. Yeast transformations with linear or plasmid DNA followed the lithium acetate/polyethylene glycol protocol (Gietz and Woods, 2002).

Nup84 complex was purified from budding yeast in which the C-terminus of Nup85 was genomically tagged with a tandem affinity purification (TAP) tag (Ghaemmaghami et al., 2003). C-terminally GFP-tagged strains MKY1262, MKY1266 and MKY1267 were derived from this strain using standard methods for genomic tagging. A seven-amino-acid spacer with the sequence Gly-Gly-Ser-Gly-Ser-Gly-Gly was included between GFP and the nup in all constructs in order to minimize the likelihood that the GFP-tag would disrupt physiological interactions between nucleoporins. Linear DNA encoding the spacer, GFP and a kanamycin

resistance marker that was flanked by sequences corresponding to the DNA sequence of the desired genomic locus of integration in yeast was generated by PCR, using pMK484 as a template and the following primer pairs: to construct MKY1262, primers 1031 and 1032; to construct MKY1266, primers 1043 and 1044; to construct MKY1267, primers 1041 and 1042. To confirm correct genomic integration of the tag, control PCRs were carried out, using genomic DNA from the newly constructed strains as a template and a primer that annealed to the GFP coding sequence (primer 931) in combination with a primer that annealed to the coding sequence of the targeted nup (primer 1046 for MKY1262, primer 1050 for MKY1266, and primer 1051 for MKY1267).

N-terminal tagging of Nup133 with EGFP was achieved in two steps by adaptamer-based genomic tagging (Reid et al., 2002). Pieces of genomic DNA sequences corresponding to the regions flanking the desired insertion site were amplified from yeast genomic DNA using primers 1088 and 1089 (upstream fragment) and primers 1091 and 1092 (downstream fragment). The PCR introduced a sequence corresponding to the 5' end of the GFP coding sequence into the upstream fragment, and a sequence corresponding to the spacer into the downstream fragment. A fragment corresponding to the EGFP coding sequence followed by the first ~2/3 of the

Candida albicans URA3 coding sequence was created using primers 1084 and 1085 with pMK485 as a template. This PCR product was spliced to the upstream fragment in a PCR reaction with primers 1085 and 1088. A fragment corresponding the last ~2/3 of the *C. albicans* URA3 coding sequence followed by the EGFP coding sequence was created using primers 1086 and 1087 with pMK490 as a template. This PCR product was spliced to the downstream fragment in a PCR reaction with primers 1086 and 1092. The two different spliced fragments were pooled and transformed into the Nup85-TAP-HIS3 strain to yield MKY1268. In this strain, the GFP-URA3 cassette separates the Nup133 promoter from the GFP-GGSGSGG-Nup133 coding sequence and thus prevents expression of the GFP-tagged nup. MKY1268 was therefore plated on medium containing 5-fluoro-orotic acid (5-FOA, purchased from American Bioanalytical), which selected for cells in which the URA3 marker had been eliminated by recombination between the two GFP sequences. The resulting strain was named MKY240.

Strains for fluorescence anisotropy medium were constructed in a W303 background since this strain is known to sporulated more efficiently than BY4743. However, the ade2– background of W303 causes the accumulation of a highly fluorescent metabolite. I therefore constructed a diploid W303 strain in which both copies of ade2– were repaired by

transformation with the ADE2 wild type sequence, obtained as the BglII fragment from plasmid pRS422 (Christianson et al., 1992). This strain, referred to as MKY363, was the parent for the GFP-tagged strains used for polarized microscopy. C-terminal diploid GFP fusion strains of Nsp1 (MKY1210), Nup49 (MKY1211), Nup57 (MKY1212) and Nic96 (MKY1213) were obtained by transformation with a PCR product generated from template pKT127 with the following primer pairs, respectively: 922+923, 924+925, 926+927, 920+921. A diploid C-terminal GFP fusion strain of Nup1 (MKY1221), was obtained by transformation with a PCR product generated from template pKT128 with primers 984+985.

N-terminal fusions of Nup57, Nup116 and Nup159 were obtained in a two-step procedure. MKY363 was transformed with PCR fragments generated from template plasmid pMK468 with the following respective primer pairs: 972+973, 978+979, 982+983. The SpHis5 marker was removed by cre-lox recombination (Gueldener et al., 2002) to obtain the final strains MKY216, MKY219 and MKY221.

The internal GFP fusion of Nup116 was created by adaptamer-based genomic tagging (see above) using the following primer pairs: 1164+1165 to generate the upstream genomic flanking sequence, 1166+1167 to generate the downstream genomic flanking sequence.

Corresponding haploid strains were obtained by sporulation and tetrad dissection of diploids.

Strain number	Description	Strain background / Parent strain	Source
–	W303 diploid	MATa/α leu2-3,112 ade2-1 his3-11,15 ura3-1 trp1-1 can1-100	ATTC
–	BY4741	MATa his3Δ1 leu2Δ0 met15Δ0 ura3Δ0	ATTC
–	Nup85-TAP-HIS3	BY4741	Ghaemmaghami et al., 2003
LDY551	mtr1-1 (ran-GEF ts mutant)	W303	Booth et al., 1999
MKY1262	Nup133-GFP-KanR	Nup85-TAP-HIS3	This study
MKY1266	Seh1-GFP-KanR	Nup85-TAP-HIS3	This study
MKY1267	Sec13-GFP-KanR	Nup85-TAP-HIS3	This study
MKY1268	GFP-URA3-GFP-Nup133	Nup85-TAP-HIS3	This study
MKY240	GFP-Nup133	Nup85-TAP-HIS3	This study
MKY363	ADE2/ADE2	W303	This study
MKY1210	Nsp1-GFP-KanR diploid	MKY363	This study

MKY1211	Nup49-GFP-KanR diploid	MKY363	This study
MKY1212	Nup57-GFP-KanR diploid	MKY363	This study
MKY453	Nup57-GFP-KanR haploid	MKY1212	This study
MKY1213	Nic96-GFP-KanR diploid	MKY363	This study
MKY454	Nic96-GFP-KanR haploid	MKY1213	This study
MKY1221	Nup1-GFP- SpHIS5 diploid	MKY363	This study
MKY216	GFP-Nup57 diploid	MKY363	This study
MKY455	GFP-Nup57 haploid	MKY216	This study
MKY219	GFP-Nup116 diploid	MKY363	This study
MKY457	GFP-Nup116 haploid	MKY219	This study
MKY221	GFP-Nup159 diploid	MKY363	This study
MKY459	GFP-Nup159 haploid	MKY221	This study
MKY227	Nup116 with GFP tag between FG domain and structured domain, diploid	MKY363	This study
MKY469	Nup116 with GFP tag between FG domain and structured domain, diploid	MKY227	This study

Table 3 Yeast strains used in the present work. Details about the construction of these strains are provided in the text.

Nup84 complex purification

Yeast cells were grown in YPD medium at 30ºC, harvested in mid-exponential phase (OD600 = 0.4–0.6), washed in water and frozen in liquid nitrogen. Frozen cell pellets were ground cryogenically in a Retsch MM301 bead mill, following the method by Cristea and colleagues (Cristea et al., 2005). 4.5 l of cell culture yielded ~3 g of cell powder. 1.5 g cell powder was thawed in 13.5 ml lysis buffer (500 mM NaCl, 110 mM KOAc, 2 mM $MgCl_2$, 20 mM HEPES pH 7.5, 0.05% CHAPS, 1 mM DTT, 1 mM PMSF, 5 μM pepstatin A and 1/100 volume of protease inhibitor cocktail, Sigma catalogue number P8340), homogenized in a Dounce homogenizer (40 strokes, tight pestle) and the lysate was clarified by centrifugation for 15 minutes at 3,200 g. Clarified lysate was incubated for 1 hour at 4ºC with 10^9 magnetic beads (Dynal) that were freshly coated with rabbit IgG (MP Biomedicals). A twofold dilution series of lysis buffer into elution buffer (200 mM NaCl, 110 mM KOAc, 2 mM $MgCl_2$, 20 mM HEPES pH 7.5, 0.05% CHAPS, 1 mM DTT) was prepared, and the beads were washed with five 1ml aliquots of sequentially diluted buffer to obtain a stepwise reduction in NaCl concentration. The beads were then resuspended in 500 µl of elution buffer, 100 units of AcTEV protease (Invitrogen) were added, and the

sample was incubated for 1 hour at 4ºC. The eluate was concentrated tenfold using Amicon Ultra filters (Millipore, 50 kDa molecular weight cutoff) and aggregates were removed from the concentrated sample by centrifugation for 15 minutes at 18,000 g. The soluble fraction was then subjected to size-exclusion chromatography in elution buffer on a Superose-6 column (2.4 ml column volume). For analytical purposes, eluted fractions were analyzed by SDS-PAGE, stained with Coomassie, and each individual protein band was identified by mass spectrometry.

During optimization of the purification protocol, recovery and loss of heptameric complex at different steps was estimated by quantifying signals from Western blotting using an antibody against the calmodulin-binding peptide moiety of the TAP-tag (Open Biosystems). The optimized procedure recovered ~20% of total cellular heptameric complex. ~10% was lost upon lysate clarification, < 2% was lost during bead washing, < 1% was lost due to incomplete cleavage with TEV protease, ~5% was lost during eluate concentration, < 1% was lost during removal of insoluble complex before size exclusion chromatography. The remaining loss occurred during incubation of the clarified lysate with IgG-dynabeads. We found that the amount of beads was limiting for subcomplex recovery at this step.

Electron microscopy

For EM, 3 μl of the 150 μl fraction containing heptameric complex (elution volume 1.1–1.25 ml, see Fig. 1a) was directly applied to a glow-discharged carbon-coated copper grid and stained with three drops of 2% uranyl formate. Electron micrographs of negatively stained samples were collected with a defocus of –1.0 μm and doses not exceeding 10 $e^{-}/Å^{2}$ per exposure on a JEOL2100 field emission gun transmission electron microscope at 200 kV and recorded with a CCD camera at a calibrated magnification of 40,641, corresponding to 5.91 Å/pixel. Micrograph pairs were taken at tilt angles of 50° and 0° in a semi-automated manner using SerialEM (Mastronarde, 2005). All images for a given construct were taken from a single grid over several days.

EM Image processing and analysis, 3D reconstruction

Low-pass filtering of the micrographs at $(15\ Å)^{-1}$, the spatial frequency corresponding to the first node of the contrast transfer function, was applied instead of contrast transfer function-correction. Pairs of tilted particles were selected interactively in the program WEB (Frank et al., 1996). Reference-free alignment and classification of untilted particles was carried out using the program EMAN (Ludtke et al., 1999). Angles between particle segments

in 90 class averages obtained from k-means classification in EMAN were measured in ImageJ (Abramoff et al., 2004) as accurately as possible. Principal component analysis was carried out in Matlab (The Mathworks). All remaining steps were implemented in SPIDER, based on procedures described in the SPIDER documentation (Frank et al., 1996). The global set of aligned particles was subjected to correspondence analysis and hierarchical ascendant classification to group particles. For two well-defined groups, initial 3D reconstructions were obtained from tilted particle images using random conical tilt reconstruction (Radermacher et al., 1986). These initial maps were used as references for projection matching. Reference projections were created in 5º increments for tilt angles from 40º to 55º, resulting in 205 projections per initial map. Each of the 9,028 tilted particle images was matched to the projection from either of the two references that resulted in the highest cross-correlation coefficient. Final maps were obtained by the simultaneous iterative refinement technique to minimize missing-cone effects.

To localize GFP densities for tagged complexes, images of untilted GFP-tagged and untagged particles were pooled and subsequently aligned and classified as before. Well-defined classes were selected and separate class averages for tagged and untagged particles from the same

class were calculated. Significance of differences between the two class averages was calculated using the method by Wagenknecht and colleagues (Wagenknecht et al., 1988); pixels with intensity values below the average value in both tagged and untagged class average images were not included in the significance map since they were localized outside the particle and therefore reflected differences in stain levels.

Docking of crystal structures into EM maps

All figures of crystal structures and EM maps were prepared using Chimera (Pettersen et al., 2004). Structures with the PDB codes 3F3F (Nup85·Seh1), 1XKS (Nup133) and 3BG0 (Nup145C·Sec13) were docked independently as rigid bodies into particle maps 1 and 2 by exhaustive cross-correlation based search in Situs (Chacon and Wriggers, 2002; Wriggers et al., 1999). From the list of likely positions, the highest-scoring position that placed the crystal structure in the correct segment of the particle (as assigned in Fig. 7a) was chosen. PDB code 3CQG (Nup107·Nup133) was docked locally based on cross-correlation in Chimera, since docking in Situs did not place the crystal structure in the correct segment of the EM map.

Fluorescence Polarization Microscopy of Yeast Cells

Yeast cells were grown at 30ºC in synthetic medium lacking riboflavin and folic acid (Sheff and Thorn, 2004), which will be referred to as "low-fluorescence medium". During the exponential growth phase (OD600 = 0.3-0.6), 1 ml of cell suspension was withdrawn and cells were pelleted by centrifugation for 5 seconds at 10,000 g. The supernatant was removed and the cell pellet was resuspended in 10 µl of low-fluorescence medium. 1 µl of the concentrated cell suspension was placed on a glass slide and the cells were immobilized by spreading the suspension with a glass cover slip. Cells mounted in this way could be imaged for up to 20 minutes. We compared this simple mounting protocol to the following, more elaborate protocol kindly provided by Dr. Frank Neumann (The Rockefeller University): A flat agarose pad was created in a depression on a glass slide by applying a heated solution of 1.4% agarose in low-fluorescence medium to the depression and removing excess agarose by sliding a second glass slide across the depression. Once the pad solidified, 2 µl of concentrated yeast cell suspension was applied to the pad and spread with a cover slip. We did not find any differences in the results obtained with these two mounting techniques when we tested both in a variety of experiments, and therefore decided to use the simpler mounting protocol, not involving the agarose pad.

For energy-depletion experiments, 1 ml of yeast cell suspension was withdrawn from an exponentially growing culture and pelleted as described above. The supernatant was removed and the cells were resuspended in 1 ml of energy-depletion medium (low-fluorescence medium lacking glucose and containing 50 mM sodium azide and 50 mM 2-deoxyglucose). For end-point imaging, the cells were incubated at 30ºC for 20 minutes and then pelleted and mounted as before. For time-course imaging, the cells were pelleted immediately after resuspension in energy-depletion medium and mounted as before, and images were taken over 20 minutes.

To monitor nuclear import activity, yeast strains transformed with plasmid CP429 (Strawn et al., 2004) were grown in low-fluorescence medium lacking uracil and methionine. Lack of uracil selected for cells maintaining the plasmid, which carries the URA3 gene required for uracil prototrophy in a ura3– genetic background. Lack of methionine induced expression of the GFP-NLS reporter protein from the methionine-repressible MET25 promoter.

An Olympus IX-70 wide-field microscope was set up for GFP fluorescence polarization microscopy as follows: light from a Xenon lamp was passed through a polarizer and the following filter set: excitation filter,

Chroma HQ 470/40 nm bandpass; dichroic mirror, 495 nm long-pass; emission filter, Chroma HQ 525/50 nm band-pass. A 60X oil objective with a numerical aperture of 1.45 was used. An Optosplit III Image Splitter (Cairn Research) split the emitted light based on polarization parallel versus perpendicular to the polarization direction of the exciting light, and these two channels were recorded as a split image with an ORCA-ER cooled CCD camera (Hamamatsu). Image acquisition was controlled by Metamorph software (Molecular Devices).

During each microscopy session, control images were taken of slides prepared with media lacking cells to correct for camera background and background fluorescence of the medium, and of a fluorescein solution assumed to have no fluorescence anisotropy to calibrate the relative intensity of the images that were split on the basis of polarization.

Quantitative analysis of fluorescence anisotropy

During each microscopy session, control images of medium alone, and of a fluorescein solution were taken. The medium-only images were used to calculate the fluorescence and camera background for each channel, and to substract it from the experimental images. The fluorescein solution was assumed to have an anisotropy of 0, since fluorescein is a small molecule

with a high rotational diffusion constant. Fluorescein images could thus be used to correct for differential transmission of light intensities in the parallel and perpendicular channels.

Pairs of images of the same cell were individually aligned based on cross-correlation with sub-pixel accuracy, and the nuclear envelopes were centered within the image by a program we developed for this purpose in SPIDER.

Centering of nuclear envelopes was achieved as follows: a circular mask with a radius of 24 pixels was applied in order to exclude adjacent cells, pixels with intensities less than one standard deviation above the image average were set to 0 intensity, and the center of gravity calculated from the remaining pixels was shifted to the center of the image. The remainder of the analysis was carried out using MATLAB programs we developed. Anisotropy was calculated pixel-by-pixel for the aligned pairs of images corresponding to the parallel and perpendicular fluorescence intensities. Only the 10% of pixels with the brightest intensity values in the parallel channel were further analyzed, since these pixels corresponded to the nuclear envelope region (**Figure 41**).

Analysis of sector anisotropy was carried out in MATLAB, using a sector mask as shown in **Figure 42**.

BIBLIOGRAPHY

Abramoff, M.D., Magelhaes, P.J., and Ram, S.J. (2004). Image Processing with ImageJ. Biophotonics International *11*, 36-42.

Axelrod, D. (1979). Carbocyanine dye orientation in red cell membrane studied by microscopic fluorescence polarization. Biophys J *26*, 557-573.

Berke, I.C., Boehmer, T., Blobel, G., and Schwartz, T.U. (2004). Structural and functional analysis of Nup133 domains reveals modular building blocks of the nuclear pore complex. J Cell Biol *167*, 591-597.

Blobel, G. (1980). Intracellular protein topogenesis. Proc Natl Acad Sci U S A *77*, 1496-1500.

Boehmer, T., Jeudy, S., Berke, I.C., and Schwartz, T.U. (2008). Structural and functional studies of Nup107/Nup133 interaction and its implications for the architecture of the nuclear pore complex. Mol Cell *30*, 721-731.

Booth, J.W., Belanger, K.D., Sannella, M.I., and Davis, L.I. (1999). The yeast nucleoporin Nup2p is involved in nuclear export of importin alpha/Srp1p. J Biol Chem *274*, 32360-32367.

Brenner, S., and Horne, R.W. (1959). A negative staining method for high resolution electron microscopy of viruses. Biochim Biophys Acta *34*, 103-110.

Cantor, C.R., and Schimmel, P.R. (1980). Techniques for the study of biological structure and function (San Francisco, W. H. Freeman).

Chernomordik, L.V., and Kozlov, M.M. (2008). Mechanics of membrane fusion. Nat Struct Mol Biol *15*, 675-683.

Christianson, T.W., Sikorski, R.S., Dante, M., Shero, J.H., and Hieter, P. (1992). Multifunctional yeast high-copy-number shuttle vectors. Gene *110*, 119-122.

Cristea, I.M., Williams, R., Chait, B.T., and Rout, M.P. (2005). Fluorescent proteins as proteomic probes. Mol Cell Proteomics *4*, 1933-1941.

Darst, S.A., Ribi, H.O., Pierce, D.W., and Kornberg, R.D. (1988). Two-dimensional crystals of Escherichia coli RNA polymerase holoenzyme on positively charged lipid layers. J Mol Biol *203*, 269-273.

Debler, E.W., Ma, Y., Seo, H.S., Hsia, K.C., Noriega, T.R., Blobel, G., and Hoelz, A. (2008). A fence-like coat for the nuclear pore membrane. Mol Cell *32*, 815-826.

Devos, D., Dokudovskaya, S., Williams, R., Alber, F., Eswar, N., Chait, B.T., Rout, M.P., and Sali, A. (2006). Simple fold composition and modular architecture of the nuclear pore complex. Proc Natl Acad Sci U S A *103*, 2172-2177.

Ferguson, M.L., Prasad, K., Boukari, H., Sackett, D.L., Krueger, S., Lafer, E.M., and Nossal, R. (2008). Clathrin triskelia show evidence of molecular flexibility. Biophys J *95*, 1945-1955.

Förster, T. (1948). Zwischenmolekulare Energiewanderung und Fluoreszenz. Ann Physik *437*, 55–75.

Fotin, A., Cheng, Y., Sliz, P., Grigorieff, N., Harrison, S.C., Kirchhausen, T., and Walz, T. (2004). Molecular model for a complete clathrin lattice from electron cryomicroscopy. Nature *432*, 573-579.

Frank, J. (2006). Three-dimensional electron microscopy of macromolecular assemblies : visualization of biological molecules in their native state, 2nd edn (Oxford ; New York, Oxford University Press).

Frank, J., Radermacher, M., Penczek, P., Zhu, J., Li, Y., Ladjadj, M., and Leith, A. (1996). SPIDER and WEB: processing and visualization of images in 3D electron microscopy and related fields. J Struct Biol *116*, 190-199.

Frank, J., Verschoor, A., and Boublik, M. (1981). Computer averaging of electron micrographs of 40S ribosomal subunits. Science *214*, 1353-1355.

Frey, S., and Gorlich, D. (2007). A saturated FG-repeat hydrogel can reproduce the permeability properties of nuclear pore complexes. Cell *130*, 512-523.

Ghaemmaghami, S., Huh, W.K., Bower, K., Howson, R.W., Belle, A., Dephoure, N., O'Shea, E.K., and Weissman, J.S. (2003). Global analysis of protein expression in yeast. Nature *425*, 737-741.

Gietz, R.D., and Woods, R.A. (2002). Transformation of yeast by lithium acetate/single-stranded carrier DNA/polyethylene glycol method. Methods Enzymol *350*, 87-96.

Gilbert, P. (1972). Iterative methods for the three-dimensional reconstruction of an object from projections. J Theor Biol *36*, 105-117.

Hinshaw, J.E., and Milligan, R.A. (2003). Nuclear pore complexes exceeding eightfold rotational symmetry. J Struct Biol *141*, 259-268.

Hsia, K.C., Stavropoulos, P., Blobel, G., and Hoelz, A. (2007). Architecture of a coat for the nuclear pore membrane. Cell *131*, 1313-1326.

King, M.C., Lusk, C.P., and Blobel, G. (2006). Karyopherin-mediated import of integral inner nuclear membrane proteins. Nature *442*, 1003-1007.

Lim, R.Y., Huang, N.P., Koser, J., Deng, J., Lau, K.H., Schwarz-Herion, K., Fahrenkrog, B., and Aebi, U. (2006). Flexible phenylalanine-glycine nucleoporins as entropic barriers to nucleocytoplasmic transport. Proc Natl Acad Sci U S A *103*, 9512-9517.

Lim, R.Y., Koser, J., Huang, N.P., Schwarz-Herion, K., and Aebi, U. (2007). Nanomechanical interactions of phenylalanine-glycine nucleoporins studied by single molecule force-volume spectroscopy. J Struct Biol *159*, 277-289.

Lim, R.Y., Ullman, K.S., and Fahrenkrog, B. (2008). Biology and biophysics of the nuclear pore complex and its components. Int Rev Cell Mol Biol *267*, 299-342.

Ludtke, S.J., Baldwin, P.R., and Chiu, W. (1999). EMAN: semiautomated software for high-resolution single-particle reconstructions. J Struct Biol *128*, 82-97.

Lutzmann, M., Kunze, R., Buerer, A., Aebi, U., and Hurt, E. (2002). Modular self-assembly of a Y-shaped multiprotein complex from seven nucleoporins. EMBO J *21*, 387-397.

Lutzmann, M., Kunze, R., Stangl, K., Stelter, P., Toth, K.F., Bottcher, B., and Hurt, E. (2005). Reconstitution of Nup157 and Nup145N into the Nup84 complex. J Biol Chem *280*, 18442-18451.

Mastronarde, D.N. (2005). Automated electron microscope tomography using robust prediction of specimen movements. J Struct Biol *152*, 36-51.

Ore, A. (1959). Intermolecular Energy Transfer and Concentration Depolarization of Fluorescent Light. Journal of Chemical Physics *31*, 442-443.

Paoli, M. (2001). Protein folds propelled by diversity. Prog Biophys Mol Biol *76*, 103-130.

Penczek, P., Radermacher, M., and Frank, J. (1992). Three-dimensional reconstruction of single particles embedded in ice. Ultramicroscopy *40*, 33-53.

Pettersen, E.F., Goddard, T.D., Huang, C.C., Couch, G.S., Greenblatt, D.M., Meng, E.C., and Ferrin, T.E. (2004). UCSF Chimera--a visualization system for exploratory research and analysis. J Comput Chem *25*, 1605-1612.

Radermacher, M., Wagenknecht, T., Verschoor, A., and Frank, J. (1986). A new 3-D reconstruction scheme applied to the 50S ribosomal subunit of E. coli. J Microsc *141*, RP1-2.

Reid, R.J., Lisby, M., and Rothstein, R. (2002). Cloning-free genome alterations in Saccharomyces cerevisiae using adaptamer-mediated PCR. Methods Enzymol *350*, 258-277.

Rout, M.P., Aitchison, J.D., Suprapto, A., Hjertaas, K., Zhao, Y., and Chait, B.T. (2000). The yeast nuclear pore complex: composition, architecture, and transport mechanism. J Cell Biol *148*, 635-651.

Sambrook, J., Maniatis, T., and Fritsch, E.F. (1989). Molecular cloning : a laboratory manual, 2nd edn (Cold Spring Harbor, N.Y., Cold Spring Harbor Laboratory Press).

Sheff, M.A., and Thorn, K.S. (2004). Optimized cassettes for fluorescent protein tagging in Saccharomyces cerevisiae. Yeast *21*, 661-670.

Sherman, F. (2002). Getting started with yeast. Methods Enzymol *350*, 3-41.

van Heel, M., and Frank, J. (1981). Use of multivariate statistics in analysing the images of biological macromolecules. Ultramicroscopy *6*, 187-194.

Wagenknecht, T., Frank, J., Boublik, M., Nurse, K., and Ofengand, J. (1988). Direct localization of the tRNA--anticodon interaction site on the Escherichia coli 30 S ribosomal subunit by electron microscopy and computerized image averaging. J Mol Biol *203*, 753-760.

Yang, Q., Rout, M.P., and Akey, C.W. (1998). Three-dimensional architecture of the isolated yeast nuclear pore complex: functional and evolutionary implications. Mol Cell *1*, 223-234.

Zinser, E., Sperka-Gottlieb, C.D., Fasch, E.V., Kohlwein, S.D., Paltauf, F., and Daum, G. (1991). Phospholipid synthesis and lipid composition of subcellular membranes in the unicellular eukaryote Saccharomyces cerevisiae. J Bacteriol *173*, 2026-2034.